ENGINYERIA ELECTRÒNICA ELÈCTRICA I AUTOMÀTICA

UNIVERSITAT ROVIRA I VIRGILI

Graduate Students Meeting on Electronics Engineering

Tarragona, Spain. June 29 - 30, 2017

BOOK OF ABSTRACTS

Index

ENGINYERIA ELECTRÒNICA ELÈCTRICA I AUTOMÀTICA

UNIVERSITAT ROVIRA I VIRGILI

Graduate Students Meeting on Electronics Engineering

Tarragona, Spain. June 29 - 30, 2017

Programme

Thursday June 29th, 2017

14:30-15:00 Chek-In and Poster Placement

15:00-15:10 Opening

15:10-16:10 Invited Talk

TiO2 :Eu3+ nanoparticles for thermometry in living cells: synthesis and characterization

Dra. Carla Bittencourt. *Université de Mons*, Belgium.

16:10-17:10 Ph. D. Students Oral Presentations

Wearable and Wireless Devices for Medical Applications, **Stefano Milici**.

Low-Power Isolated DC/DC Converters for Mismatch Mitigation in Photovoltaic Systems, **Nazmul Hassan**.

Combined Pulsed UV and Temperature Activation of Metal Oxide Nanomaterials in Breath Analysis Applications , **Oriol González**.

17:10-17:30 Break and Poster Session

17:30-18:30 Invited Talk

Data correction methods and time-series analysis for metabolomics

Dra. Julie Wilson. *University of York*, United Kingdom.

Friday June 30th, 2017

9:30-10:30 Invited Talk

Applications of fractional differentation to modelling and control

Dr. Jocelyn Sabatier. *Université Bordeaux 1*, France.

10:30-11:10 Ph. D. Students Oral Presentations

Output Voltage Regulation of a Boost Converter With Constant Power Load by Means of Sliding Mode Control, **Blanca Areli Martínez.**

Characterization of Human Breath Profiles by Using WO3 and Commercial SnO2 Gas Sensors Combined with Multivariate Analysis, **Tarik Saidi.**

Ligand-capped AuNPs Gas Sensor Array for Gastric Cancer Diagnosis in Exhaled Breath, **Tesfalem Welearegay.**

11:10-11:30 Break and Poster Session

11:30-12:30 Invited Talk

Engineering Biological Circuits for Fine and Speciality Chemical Synthesis

Dra. Mariona Vinaixa. *University of Manchester*, United Kingdom.

12:30-13:30 Invited Talk

2D Electronics – Opportunities and Challenges

Dr. Frank Schwierz. *Technische Universität Ilmenau*, Germany

13:30 Closing and Lunch

Invited Sessions

TiO_2 :Eu^{3+} nanoparticles for thermometry in living cells: synthesis and characterization

Carla Bittencourt
Université de Mons
Belgium

Luminescent thermometry has been reported as a key technique for probing spatial distribution of temperature with sub-micrometer resolution [1]. In this context, we evaluate the use of TiO_2 nanoparticles (NPs) doped with Eu^{3+} ions for nanothermometry of single cells. TiO_2 NPs are reported to be non-toxic, and chemically stable material, having a wide variety of biological applications.

Anatase nanoparticles doped with Eu^{3+} (TiO_2: Eu^{3+}) were synthesized according to the sol-gel method [2]. The luminescence spectra of the synthesized TiO_2: Eu^{3+} NPs as a function of temperature (288 K – 323 K), show emission bands in two distinct spectral regions: one associated with trap emission in the TiO_2 and the other with emission peaks of the dopant $Eu^{3+.}$ Using L929 cells incubated with NPs, we show that these nanostructures can be used to probe local temperature within single cells with sensitivity near to 1-2%/K. Temperature measurement with the TiO_2: Eu^{3+} nanoparticles should be artifact-free, since Eu^{3+} atom is incorporated in a TiO_2 lattice, and thus isolated from intracellular environment.

[1] D. Jaque, F. Vetrone, Luminescence nanothermometry, Nanoscale 4 (2012) 4301- 4326.
[2] Ž. Antić, R. M. Krmanović, M. G. Nikolič, M. Marinović-Cinović, M. Mitrić, S. Polizzi, M. D. Dramićanin. Multisite luminescence or rare earth doped with TiO_2 anatase nanoparticles. Materials Chemistry and Physics 135 (2012)1064-1069.

Data correction methods and time-series analysis for metabolomics

Julie Wilson
University of York
United Kingdom

There is a particular need for reproducible and comparable results in non-targeted metabolomics, especially when differences between experimental groups are small. Pre-processing methods, such as the binning and de-noising of NMR spectra and the use of quality control (QC) samples to correct variation between batches in LC-MS data will be discussed.

Time series data can reveal differences between experimental groups that are not apparent when considering individual time points and potentially allow the metabolic networks associated with biochemical processes to be inferred. Here control-correction may be necessary to ensure that the time profiles are related to the conditions of interest. A software package, MetaboClust, that allows an interactive approach to time-course analyses will be introduced. The software can be used to apply data correction, generate the time-profiles, perform exploratory statistical analysis and to assign tentative metabolite identifications. Clustering algorithms group metabolites showing similar responses together in an unbiased manner. This allows the software to highlight pathways warranting further investigation, based on the overlap between their constituent metabolites and the annotations associated with clusters showing interesting trends.

Applications of fractional differentation to modelling and control

Jocelyn Sabatier
Université Bordeaux 1
France

In this talk, a short reminder on fractional differentiation and fractional models is proposed. Some applications of these models done by the CRONE group (CRONE is the French acronym for Fractional Order Robust Control) at IMS laboratory are presented. It is first shown how fractional models can be used to model the dynamic input-output behavior of electrochemical components such as batteries, ultracapacitors and fuel cells. In the case of lithium-ion batteries, obtained fractional models are used to design state of charge estimators. Then, CRONE control, a robust control method that uses fractional differentiation for the open loop transfer function definition of a common unity-feedback configuration is presented. This control methodology ensures robustness of the loop stability-degree with respect to the parametric plant perturbation, and also permits shaping constraints on the 4 usual closed loop sensitivity functions. Several applications of CRONE Control made in the context of industrial collaborations are finally presented.

Engineering Biological Circuits for Fine and Speciality Chemical Synthesis

Mariona Vinaixa
University of Manchester
United Kingdom

There is a particular need for reproducible and comparable results in non-targeted metabolomics, especially when differences between experimental groups are small. Pre-processing methods, such as the binning and de-noising of NMR spectra and the use of quality control (QC) samples to correct variation between batches in LC-MS data will be discussed.

Time series data can reveal differences between experimental groups that are not apparent when considering individual time points and potentially allow the metabolic networks associated with biochemical processes to be inferred. Here control-correction may be necessary to ensure that the time profiles are related to the conditions of interest. A software package, MetaboClust, that allows an interactive approach to time-course analyses will be introduced. The software can be used to apply data correction, generate the time-profiles, perform exploratory statistical analysis and to assign tentative metabolite identifications. Clustering algorithms group metabolites showing similar responses together in an unbiased manner. This allows the software to highlight pathways warranting further investigation, based on the overlap between their constituent metabolites and the annotations associated with clusters showing interesting trends.

2D Electronics – Opportunities and Challenges

Frank Schwierz
Technische Universität Ilmenau
Germany

During the past decade, 2D (two-dimensional) materials have attracted enormous attention from various scientific communities ranging from chemists and physicists to material scientists and device engineers. The rise of the 2D materials began in 2004 with the pioneering work on graphene at Manchester University and Georgia Tech. Particularly the observed high carrier mobilities raised early expectations that graphene could be the perfect channel material for FETs and supersede the conventional semiconductors. It soon became clear, however, that due its zero bandgap graphene is not suitable for FET channels. Therefore, the prospects of graphene transistors are assessed rather pessimistic now. However, researchers have extended their work to 2D materials beyond graphene and the number of 2D materials under investigation is continuously rising. In part the 2D materials beyond graphene materials possess sizeable bandgaps and therefore are considered to be useful for electronic applications. Indeed, rapid progress has been made in research on 2D transistors and experimental FETs using 2D channel materials beyond graphene have been reported by many groups around the world. The most recent bang was the demonstration of a well performing 1-nm gate MoS_2 MOSFET. On the other hand, and in spite of the rapid progress in the field, the debate on the real prospects of 2D MOSFETs for future electronics is still controversial.

In the present lecture, the most important classes of 2D materials are introduced and the potential of 2D transistors is assessed as realistically as possible. To this end, two important properties of transistor channels – the bandgap and the mobility – are examined and the mobility-bandgap tradeoff is discussed. The state of the art of 2D transistors is reviewed by (i) summarizing relevant results of leading groups in the field and (ii) presenting examples of lecturer's own work on 2D materials and transistors. Moreover, the performance of 2D transistors is compared to that of competing conventional transistors, in particular Si MOSFETs and III-V HEMTs, and a balanced view of both the pros and cons of 2D transistors is provided. Finally, potential applications of 2D transistors in both the More Moore and the More Than Moore domains of semiconductor electronics are identified. It is shown that 2D channel materials with heavy carrier effective mass may enable MOSFET scaling beyond the limits of the Si MOSFET and extend the lifetime of Moore's Law in digital CMOS. This could be important for the industry since digital CMOS covers around 70% of the overall chip market. Moreover, 2D materials are bendable and stretchable and therefore show promise for the emerging field of flexible electronics.

Regular Sessions

Wearable and Wireless Devices for Medical Applications

S.Milici, A.Lazaro, J.Lorenzo, R.Villarino, D.Girbau

Department of Electronics, Electrics and Automatics Engineering (DEEEA),
Universitat Rovira i Virgili (URV),
Tarragona, Spain
e-mail: stefano.milici@urv.cat, antonioramon.lazaro@urv.cat

Abstract

Sleep disorder disease (SDA) and sleep apnoea are, at this moment, very common pathologies that affect at least 25% of the worldwide population. The method to investigate this disease is expensive, complicated, and needs hospitalization of patients. Comfortable wireless devices can be designed to detect the main parameters of SDA. The aim of this work is to study the feasibility of using the modulated frequency selective surface (FSS) as a semi-passive tag for body sensing applications. Two examples are presented: a breathing sensor and a skin thermometer. The wireless communication is performed by a backscattered field technique, which varies the signal received by the transponder. The tag is composed by an array of dipoles, which are loaded with varactor diodes. This backscattering technique saves a large amount of energy in comparison to commercial alternatives and guarantees a long battery lifetime. The design, simulation, and characterization of the FSS are discussed, as well as performance of the sensors when place on the body.

1. Introduction

Sleep apnoea is a common medical disorder that occurs when breathing is interrupted during sleep, also known as sleep-disorder breathing (SDB). Apnoea events can occur up to thirty times an hour, and has direct correlation with major diverse pathologies such as; hyperactivity disorder, diabetes, cardiovascular disease (including strokes), and arterial hypertension. Many wearable systems propose they monitor the respiration parameters during sleep but can't assess sleep quality. Wearable devices are smart accessories that integrate sensors, microcontrollers and wireless transceivers that can be worn on the body. Smart watches are the most popular wearable devices that are used generally as activity trackers. The method of communication that typically uses little energy is Bluetooth, which allows sending the data to a mobile phone and storing the data on a database. This topology presents some challenges; one of the most important ones is the limited battery life claimed by the users, due to the power consumption of the microcontroller and the transceiver, especially in continuous long-term monitoring applications. The continuous monitoring of skin temperature and respiration rate represents an important role into the understanding of various health, but, unfortunately, is impracticable using this technology. In this work, a semi-passive tag based on a modulated frequency selective surface (FSS) is proposed for sensing [1]. The FSS consists of an array of dipoles loaded with reverse-biased varactor diodes connected to a low-frequency oscillator. Therefore, the communication is performed by modulating the radar cross section with backscattering. In previous work, it is demonstrated that FSS on contact with the body can achieve large bandwidth avoiding the typical detuning problem of narrow band tags such as UHF tags. In addition, FSS can be printed on a flexible thin-film substrate that allows the integration on textile clothing, making it a flexible and comfortable option. The oscillation frequency of the oscillator, which modulates the FSS, may be used to sense various parameters. In this work, a temperature dependent resistor is employed to change the modulation frequency[2,3] and the temperature variation is transmitted using a frequency modulation. Applications of these sensors are here presented. Furthermore, this FM modulator does not need any microcontroller and transmitter module. The result is a strong increase of the battery lifetime drawing 40 µA at 3 V, even in continuous real-time monitoring cases, which implies a reduction on maintenance costs and a saving on the battery charge circuit, reducing the cost and size of the devices.

2. Method

A. Backscattering communication using FSS for on-body applications

The proposed system consists of two components: An unlicensed ISM 2.45GHz reader and either one or more transponders (tags) based on FSS technology to be placed onto the skin to measure the temperature variations. The reader produces a continuous wave (CW) that illuminates the tag with frequency f_c, which answers by modulating the backscatter of the FSS *radar cross section* (RCS).

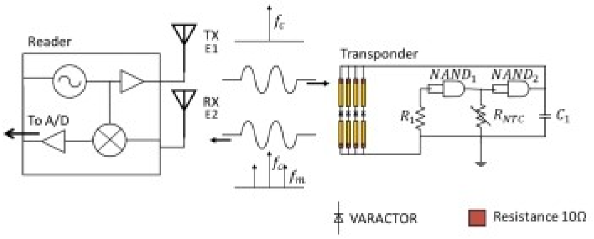

Fig. 1. Block diagram of the system, including the reader and the FSS.

In order to study the performance of the FSS transponder in different curved parts of the body, various simulations on a cylindrical human model are performed. The body model is simulated using a cylindrical multilayer shape surrounded by an FSS transponder composed by seven elements.

B. Breathing sensor

Fig. 2 shows the parts of the breathing sensor. The FSS is included into the headband, while the oscillator is inserted in the back of the headband and, a 3V coin battery is connected on the same board. A two-wire cable connects the oscillator to the FSS. A NTC resistor is placed under the nose, connected with a thin cable to the oscillator as shown in Fig. 2b.

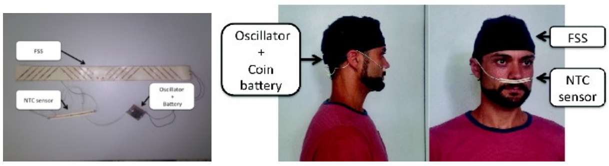

(a) (b)

Fig. 2. (a) Breathing sensors. (b) Placement on the body.

C. Temperature sensor

The FSS is connected to a low-frequency oscillator, which is based on a two-inverter oscillator (Fig. 3). It draws 8μA from a 3V button-type battery. The oscillation frequency f_m depends on the RC time constant, where R is the oscillator resistance and C is the capacitance. In this case, R is an NTC variable resistance that depends on the temperature.

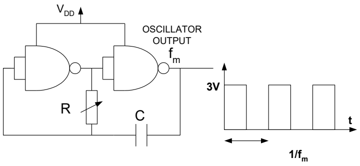

Fig. 3. Schema of the modulating oscillator. NAND based oscillater.

3. Results

For the test, the FSS is modulated with a low-frequency generator. A CW generator that transmits at 2.45GHz using an 8dB gain antenna illuminates a prototype with 7 dipoles. Fig. 4 shows the signal received at the spectrum analyser.

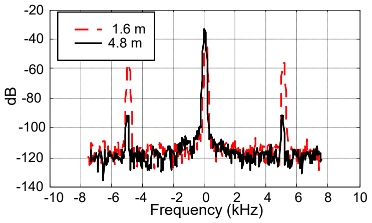

Fig. 4. Measurement of the spectrum at 2.45GHz (at 1.6 m solid line and 4.8 m dotted line).

The measurement setup is shown in Fig. 2. Fig. 5 shows the performance of the sensor during apneas. The algorithm can calculate correctly the respiration rate.

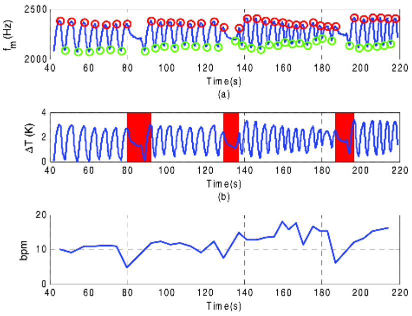

Fig. 5. Example of measurement for a person with apnoea: (a) measured modulation frequency, (b) temperature change,(c) breaths per minute.

The calibration of the temperature sensor has been performed using a Peltier cell. In the range of body temperature, the sensor behaviour can be easily approximated as a linear function of the modulation frequency. The resolution in terms of temperature is approximately 0.05K.

4. Conclusions

In this study, we demonstrate the use of FSS as alternative method of transmission for a simple, not expensive sensor. Sensors with high accuracy, resolution, and long lifetime can be designed to perform medical measurement. Backscattering communication between the tag and the reader by modulating the FSS radar cross section (RCS) is achieved. Low-cost reverse biased varactors are used as switching elements to reduce the consumption and to increase the battery lifetime, one of the harder challenges for wearable devices.

References

[1] J. Lorenzo, A. Lazaro, R. Villarino, and D. Girbau, 'Modulated Frequency Selective Surfaces for wearable RFID and sensor applications', *IEEE Trans. Antennas Propag.*, vol. PP, no. 99, pp. 1–1, 2016.

[2] Milici, S., Lorenzo, J., Lazaro, A., Villarino, R., & Girbau, D. 'Wireless Breathing Sensor Based on Wearable Modulated Frequency Selective Surface', *IEEE Sens. J.*, vol. 17, no. 5, pp. 1285–1292, Mar. 2017.

[3] S. Milici, A. Lazaro, J. Lorenzo, R. Villarino, and D. Girbau, 'Wearable Sensors Based on Modulated Frequency Selective Surfaces', *accepted* to European Microwave Week *Conference*, Nuremberg, October 2017.

Low Cost Fast Transducer Prototyping Technique

M. Alvarado[1], J.L. Ramírez[1], A.J. Romero[1]

1. Minos-EMaS, Departament d'Enginyeria Electrònica, Universitat Rovira i Virgili, Tarragona, Spain

*Correspondence: miriam.alvarado@urv.cat, joseluis.ramirez@urv.cat

Abstract

In this work we present a low cost fast prototyping technique for stencil circuit printing. The use of inexpensive polymer film to produce the mask makes it cheaper than an inox mesh for screen printing. We printed some devices with different geometries and obtained 150 µm resolution and high reproducibility.

1. Introduction

During the last years, technological advances have adapted printing technologies to the electronics field. Among its advantages are the reduction in the fabrication time and costs, allows non-traditional materials, simplifies the process, etc. Printing technologies have made it possible to develop electronics components in various materials such as, fabric, paper, and plastics. The increasing use of polymer substrates for printed electronics is evidenced by development of devices such as large area printed pressure sensors, radio frequency identification tags, solar cells, light emitting diodes and transistors [1].

Thin Polymeric films as substrates are extremely attractive, they can be made lightweight and inexpensive making it possible to target high-volume and low-cost commercial products. Polymer films are inherently plastic enabling a high degree of mechanical flexibility and conformability. A number of plastic films are available including thermoplastic amorphous polymers such as polycarbonate, polyether sulfone, and high-transition glass temperature materials (Tg) such as polyimide [2]. The polyimide has excellent physical, electrical and mechanical properties over a wide temperature range, -269°C until 400°C.

For printed electronics is required a special ink. This fact brings a challenge, to find a material with the adequate chemical and physical properties to be used as an ink. Majority of printable materials are in the form of solutions, which require specific properties to allow proper printing on variety of plastic or paper substrates. Silver (Ag) based pastes and solutions are included in the list of materials used for printed electronics and are the choice of most of the researchers due to its good physical and electrical performance on plastic substrates. [1]

Among the printed technologies is the Stencil technique. With the stencil technique an image is obtained by applying pigment to a surface over an intermediate object (stencil) with designed gaps in it which create the pattern or image by only allowing the pigment to reach some parts of the surface. In practice, the object is usually a thin sheet of material, such as paper, plastic, wood or metal with a design cut from it, used to produce a design on an underlying surface by applying pigment through the cut-out holes in the material. The use of a polymer film to produce the mask makes it cheaper than the inox mesh used traditionally for screen printing. Cutting the mask with a CO_2 laser we get, in a few seconds, 150 µm resolution and high reproducibility. Besides, the computer-aided design is a powerful tool to obtain a wide range of devices or circuits. In this work we developed a stencil technique to deposit a conductive ink over a flexible polymeric substrate using a plastic stencil.

2. Experimental

A commercial high resistant polyimide film (Kapton 50µm) has been used to deposit silver ink onto it. To fabricate the stencil, an adhesive coated polyimide film (Kapton 25 µm) has been used. The adhesive coated polyimide (Kapton 25 µm) was stuck to polyimide film (Kapton 50 µm). We used a piece of 3 cm · 5 cm of Kapton 50 µm and over it the adhesive polyimide (Kapton 25 µm) was stuck. The designs to be deposited were plotted in a vector graphics editor software creating a file with EPS (Encapsulated PostScript) extension, this was done with the aim to have a file compatible with the software of the laser. Afterwards only the adhesive coated polyimide was cut with a CO_2 laser. Once cut the design, the surface was cleaned with a cloth moistened with ethanol (Ethanol 96% Pure, Sigma Aldrich), figure 1 shows a mask after cleaned it. Then the parts to be deposited were removed manually, using a microscope to get a better view of cut areas. To deposit the silver ink (DuPont 5064H silver conductive), it was distributed with a spatula filling the cut-out holes with ink. The ink was dried in an oven at 130 °C for 20 minutes. Finally, the devices were taken out of the oven and the remaining parts of the adhesive polyimide were removed carefully. We obtained the design cut deposited onto the polyimide film (50 µm). With a multimeter we checked the continuity of the tracks and looked for short-circuits.

3. Results

We obtained a set of 2.5 cm · 2.5 cm devices, interdigitated electrodes and bridges of interdigitated electrodes (IDE). Figure 2 shows the different devices printed, the part C) shows a bridge of IDE over 50 µm thick flexible polyimide film, tracks width of 300 µm and a thickness of 25 µm with a separation between tracks of 300 µm. In our example, actual dimension shows a variation of ±15%. The variation in the dimension is due to the potency applied with the laser and issues of file conversion. While the potency applied with the laser is higher, the cutting lines get thicker and in consequence this fact modifies the dimensions of the design. We obtained a 150 µm resolution, below this distance, joints between the tracks were presented.

We have greatly reduce the time and the cost of the mask generation process. The full process, from CAD design to mask availability, takes less than forty minutes work. The cost of 0.2 m^2 adhesive Kapton is around 0.51 €, obtaining about 250 masks. The cost of a stencil mask made externally is around 100 € and availability in the order of weeks.

4. Conclusions

This technique is effective for manufacturing stencil mask, faster and cheaper than other manufacturing methods. Has been used to obtain different designs: heaters, contacts, connecting tracks, etc. The maximum dimensions of the mask to be manufactured are constrained by the cutting area of the laser used. Tolerance in the obtained dimensions is due to the polyimide remaining glue and the loss of material during the mask removing.

One drawback of the mask adhesive polyimide is to have adhesive residue mixed with silver paste, this may produce circuit failures and non-homogeneous tracks. We occasionally have found traces of the material used to clean, deposited with the ink. The obtained mask are cheap and disposable, so they are the perfect choice for prototyping at development design phase.

Fig.1. Mask stuck to the flexible substrate, before to deposit ink.

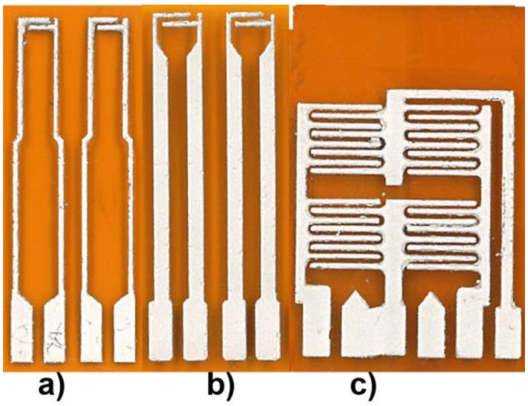

Fig. 2. Different geometries obtained through stencil technique. a) IDE with a gap of 300 µm, b) IDE with a gap of 500 µm and c) a bridge of IDE with gaps of 300 µm.

5. References

[1] Khan, S., Lorenzelli, L., Dahiya, R. S., & Member, S. (2015). Technologies for Printing Sensors and Electronics Over Large Flexible Substrates: A Review, 15(6), 3164–3185.

[2] Zardetto, V., Brown, T. M., Reale, A., & Carlo, A. Di. (2011). Substrates for Flexible Electronics : A Practical Investigation on the Electrical, Film Flexibility, Optical, Temperature, and Solvent Resistance Properties, 638–648. https://doi.org/10.1002/polb.22227

Carbon quantum dots: Synthesis and Applications for light emitting diodes

Sofia Paulo,[a,b] Eugenia Martinez-Ferrero,[b,*] Emilio Palomares[a,c,*]

[a] *Institute of Chemical Research of Catalonia (ICIQ), The Barcelona Institute of Science and Technology (BIST), Avinguda del Països Catalans 16, 43007 Tarragona, Spain.*

[b] *Fundació Eurecat. Av. d'Ernest Lluch 36, Parc Científic i de la Innovació TecnoCampus, E-08302, Mataró, Barcelona, Spain Mail: eugenia.martinez@eurecat.org.*

[c] *Catalan Institution for Research and Advanced Studies (ICREA), Passeig de Lluis Companys 23, 08010 Barcelona, Spain. Fax: +34 977920224; Tel: +34 977920200; Mail: epalomares@iciq.es.*

Abstract

Semiconductor quantum dots (QDs)[1] have been deeply studied from the last years for their extraordinary optical properties such as narrow spectra emission bandwidth, color tuneability, high quantum yield and their use in a range of applications such as optoelectronic devices, biological system.

However, the high known toxicity and costly reactants represent a huge problem to scale-up improvement. To try to solve this problem a new generation of carbon based quantum dots appeared in the last decades. The main advantage is the use of free heavy metals, non-chloro-solvents and ordinary reactants to obtain it. In this abstract, we want to describe one of the possible applications of working with carbon quantum dots(CQDs or CD) as active layers in light emitting diodes (LEDs).

1. Introduction

The first article describing carbon quantum dot synthesis at large scale was in 2006[2]. From that moment, a few groups tried to synthesize tunable carbon quantum dots using one method. The main goal was obtain different color emission spectra for biological, energy conversion or optoelectronics [3].

On the other hand, Quantum dots LEDs (QLEDs) have emerged in the last year as new LEDs generation due to better narrow emission bands and color tuneability in over the entire visible spectrum[4].

There are a few publications using graphene[5] structure as emissive layer in LEDs, however until 2004, Fu Wang[2] et al published CQDs using hexadecylamonium (HDA) as passivated ligand, working as emissive layer in OLEDs.

2. Synthesis and characterization.

The synthesis of carbon quantum dots was carrying out according Fu Wang et al. method .Briefly, 15mL 1-octadecene (ODE) and 1,5g of 1-hexadecylamine (HDA) were stirred in a three neck flask under inert conditions during 30min at 120ºC. Next, the solution was heated up to 300ºC. At 300ºC, 1g of citric acid was added as quickly as possible and keeping the reaction 3 hours at 300ºC. Carbon quantum dots were precipitated in acetone and redispersed in toluene and dichloromethane for its characterization. Samples were characterized by absorbance/ emission spectra and electrochemical cyclic voltammetry(fig 1). Synthesized CQDs show an emission peak centred at 440 nm and a quantum yield of 44% using Couramine 102 as reference dye.

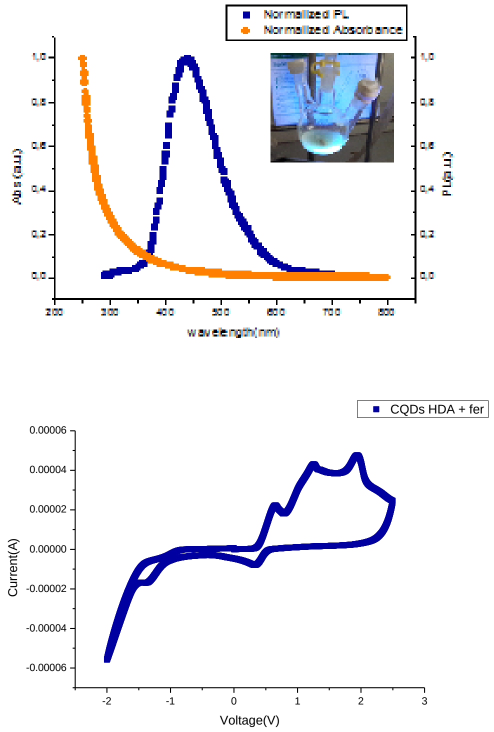

Figure 1.UV/vis absorption and PL spectra of CQDs. Electrochemical cyclic voltammetry using ferrocene as reference.

3. Results

The idea of working with hybrid LEDs (HyLEDs) instead of organic LEDs (OLEDs) is to try to avoid as much as possible organic compound due to low stability versus inorganic oxides In figure 2 depicts the diagrammatic representation of each element used to fabricate the HyLEDs. Zinc oxide (ZnO) works as electron transport layer, next we deposit an interlayer of polyethylenimine (PEI) because PEI can enhance electron injection from metal oxide to active layer as well as balance of charge injection through the device[6]. CD works as emissive layer and poly(9-vinylcarbazole) (PVK) and MoO3 as hole transport layer.

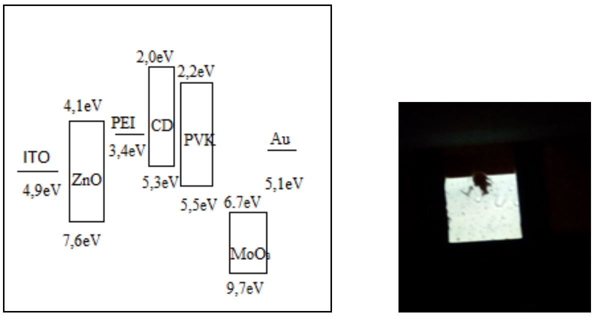

Figure 2. Energy levels diagram of the material employed with the device structure. Photograph of a HyLED applying a voltage.

Figure 3, we present the current density voltage and the luminance versus voltage of QLEDs. In table 1we show the final results working with different concentrations of CQDs. There was not a significant difference in the final luminance working with different concentrations and the currents remains constant in all the devices,

Device	Turn-on Voltage(V^a)	Max lum (Cd/m2)
CQDs-HDA 5mg/ml	5,45	4,33
CQDs-HDA 10mg/ml	6,26	3,36
CQDs-HDA 20mg/ml	4,86	3,74
CQDs-HDA>20mg/ml	5,76	4,00

Table 1. *V^a is the turn-on voltage at 0,01 Cd/m2*

a)

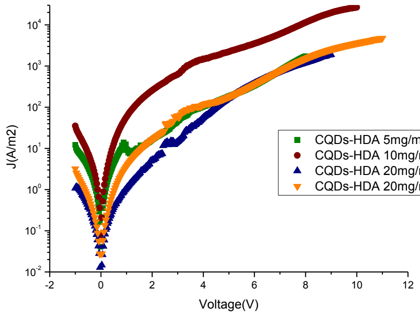

b)

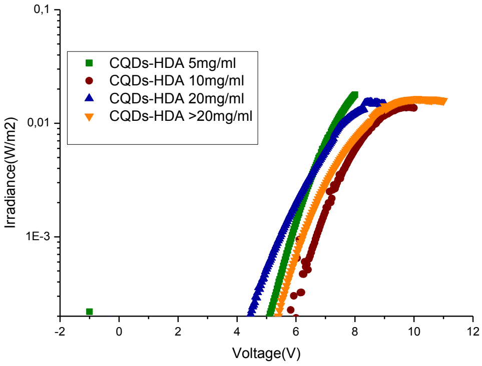

Figure 3. a) Curve IV. b) Irradiance (W/m2) versus voltage(V).

4. Conclusions

In summary, we have successfully fabricated a Hybrid LEDs using a free heavy metal quantum dot and work all the layers were deposit in air conditions except MoO3 and Ag, they were evaporated . Further optimization is necessary to achieve competitive results. This include optimization of the device fabrication and also testingy different capping ligands. However, we show here that it is possible to obtain monocolor white light emission devices using CQDs.

5. References.

1. Scalbi, S., Fantin, V. & Antolini, F. Environmental assessment of new technologies: Production of a Quantum Dots-Light Emitting Diode. *J. Clean. Prod.* **142,** 3702–3718 (2017).
2. Wang, G., Pan, X., Kumar, J. N. & Liu, Y. One-step synthesis of hollow carbon nanospheres in non-coordinating solvent. *Carbon N. Y.* **83,** 180–182 (2015).
3. Ding, H., Yu, S.-B., Wei, J.-S. & Xiong, H.-M. Full-Color Light-Emitting Carbon Dots with a Surface-State-Controlled Luminescence Mechanism. *ACS Nano* acsnano.5b05406 (2015). doi:10.1021/acsnano.5b05406
4. Anikeeva, P. O., Halpert, J. E., Bawendi, M. G. & Bulović, V. Quantum Dot Light-Emitting Devices with Electroluminescence Tunable over the Entire Visible Spectrum. *Nano Lett.* **9,** 2532–2536 (2009).
5. Gupta, V. *et al.* Luminscent graphene quantum dots for organic photovoltaic devices. *J. Am. Chem. Soc.* (2011). doi:10.1021/ja2036749
6. Zhou, Y. *et al.* A Universal Method to Produce Low{\textendash}Work Function Electrodes for Organic Electronics. *Science (80-.).* **336,** 327–332 (2012).

COMBINED PULSED UV AND TEMPERATURE ACTIVATION OF METAL OXIDE NANOMATERIALS IN BREATH ANALYSIS APPLICATIONS

O. Gonzalez [1], C. Jaeschke[2] ,T. Welearegay[1] , S. Roso[1,3], X. Vilanova[1] and E. Llobet[1]

[1]MINOS-EMaS, Universitat Rovira i Virgili, Avda. Països Catalans, 26, 43007, Tarragona, Spain.
[2]JLM Innovation, Tübingen, Germany
[3]ICIQ, Institute of Chemical Research of Catalonia, Avda. Països Catalans, 16, 43007, Tarragona, Spain.

Abstract

The aim of this work is to develop a system for breath analysis, introducing a new methodology for improving the discrimination between ethanol and acetone at high humidity levels. Ethanol and acetone are present in exhaled breath and have been identified as biomarkers of different diseases especially in patients suffering from colorectal cancer [1]. The system comprises a 6-element sensor array employing In_2O_3 and WO_3 nanomaterials, which are operated under pulsed-UV and at two different temperatures. Two response variables are obtained for each sensor: the rate of electrical resistance change when UV is on and the same when UV is off. Those rates are input to a non-supervised method: PCA. The results obtained strongly suggest that this setup could be useful for detecting these biomarkers in breath analysis applications.

1. Introduction

Nowadays lot of efforts are focused in developing non-invasive systems to diagnose diseases by analyzing exhaled breath. But there are challenging problems in such an approach as the high levels of humidity and the low concentrations of biomarkers for the different diseases.

The capacity of UV light to clean and desorb the species previously adsorbed on the surface of metal oxides has been reported [2]. It is also known that temperature modulation of metal oxide gas sensors is useful for extracting additional information and ameliorating their selectivity. When combined, the pulsed UV operation results in response patterns that appear to depend on the species present in the sensor environment. This is illustrated in Figure 1 from [3]. In the present work we use Pulsed-UV to discriminate between acetone and ethanol in a high humidity background.

2. Experimental

Pure or metal doped tungsten oxide (WO_3) nano-needles were directly grown on ceramic substrates [3]. The ceramic substrates have printed Pt electrodes on one side and a Pt heater on the other side. Indium oxide nano-octahedra were synthesized [2]. The sensor array is listed in Table 1

id	Material	R0
1	WO3 NW	26 kΩ
2	WO3 NW + Ni NP	100 kΩ
3	WO3 NW + Pt & Au NP	218 kΩ
4	WO3 NW + Pd NP	787 kΩ
5	WO3 NW + Fe NP	1.42 MΩ
6	In2O3 Octahedra	842 Ω

Table 1: Sensor array, Ro is the baseline resistance at 40 ºC

A sensor test chamber with inner volume of 24 cm^3 was designed and constructed in Teflon. The chamber contains sockets to which up to six sensors can be plugged in to be tested. The cover lid houses two UV LEDs with a maximal emitting optical power of 400 µW at 355 nm. Therefore, sensors can heated when a

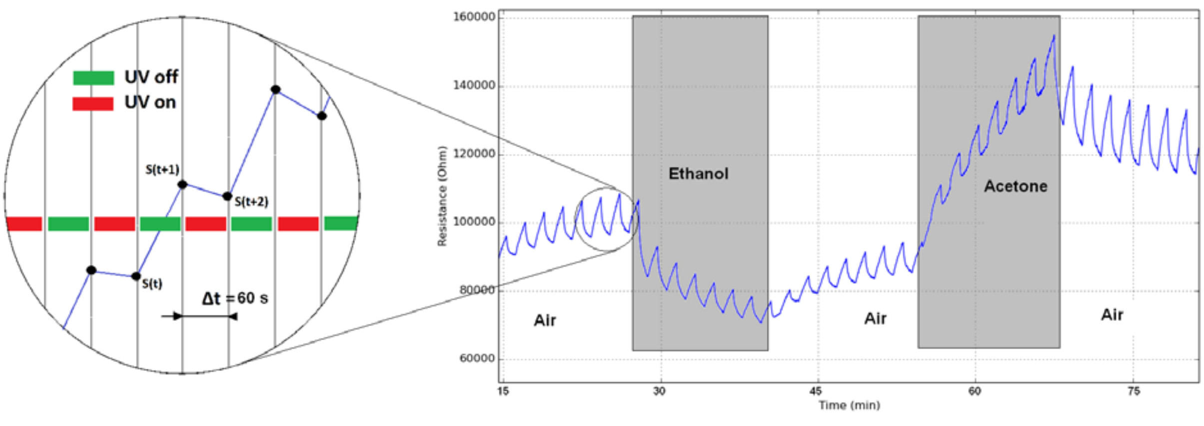

Figure 1: Ripple of the resistance in sensor WO3 + Fe (sensor id 5) produced by UV effect at 40 ºC

constant current is driven through their heating element and simultaneously can be activated by UV light. For the sample gas generation we have developed a breath simulator. This system consists of 4 proportional valves controlling the flow of synthetic dry air as well as the flow rates from 3 different head-spaces. The concentrations in the headspace have been fixed in a previous work [4]. Using this mixing system, we have programed a pattern of vapors in a balance of humidified air (70 % RH) to be delivered to the sensors, figure 2

RESULTS AND DISCUSION

The lower part of Figure 2 shows the temporal evolution of the electrical resistance of the indium oxide sensor under the different operating modes described above. It is easy to see that each operating mode produces a different response pattern of the sensor under gas exposure. The data set is composed by rates defined in [2] (UV_ON and UV_OFF). So we have the data organized in 16 variables (4 sensors x 2 temperatures x 2 UV-rates) that is synchronized with gas concentrations. This means that switching the UV source at a 2 min period and considering that each vapor concentration is held constant during 15 min, 7 to 8 points are acquired for a given species and concentration. With those considerations, we have obtained the PCA analysis that is plotted in figure 3.

CONCLUSIONS

The effects of heating and UV irradiation in the response toward ethanol and acetone in an array of WO_3 nano-needles and screen-printed sensors employing vapor-phase transport synthesized indium oxide octahedra as active material have been studied under 70% RH. It was found that at almost RT (40 ºC), pulsed-UV irradiation and no heating was unsuitable for discriminating between those compounds. On the other hand, combining mild heating with pulsed UV light irradiation of the sensor surface, resulted in a dramatic enhancement in sensitivity and selectivity, combined to the possibility of making significant savings in power consumption. This has been achieved by exploiting the dynamics of sensor response under pulsed UV light (i.e., the rates of oxidation and reduction of the indium oxide).

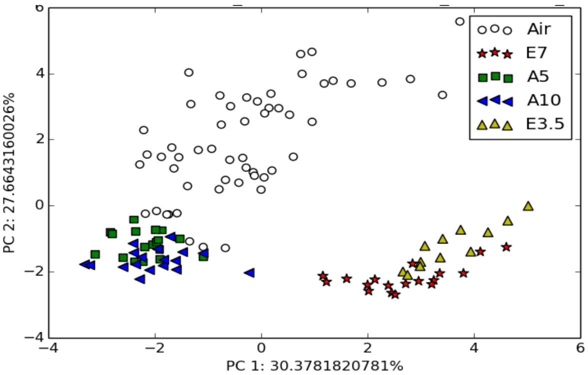

Figure 3: PCA result, for discriminate compounds.

REFERENCES

[1] H. Amal, M. Leja et al. *Breath testing as potential colorectal cancer screening tool*, International Journal of Cancer 138, 229–236 (2016); doi: 10.1002/ijc.29701

[2] O.Gonzalez, S.Roso, X.Vilanova and E.Llobet, Enhanced detection of nitrogen dioxide via combined heating and pulsed UV operation of indium oxide nano-octahedra, Beilstein J. Nanotechnol. 2016, 7, 1507–1518. 2016

[3] O. Gonzalez, T. Welearegay, E. Llobet, X. Vilanova. Pulsed UV Light Activated Gas Sensing in Tungsten Oxide Nanowires Procedia Engineering Pages 351-354 2016

[4] A. Tripler. An introduction to headspace sampling in gas chromatography fundamentals and theory. PerkinElmer, Inc. 1014 (3-12)

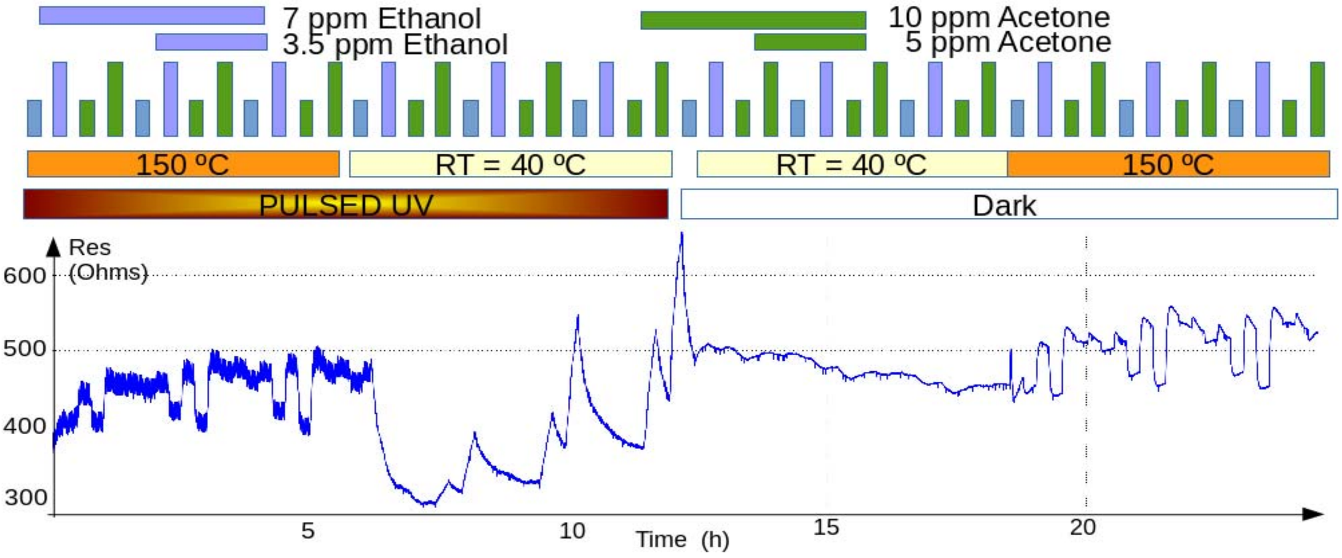

Figure 2: In2O3 octahedra (sensor id 6) response under different modes and gas concentrations.

Raman spectroscopy studies of gold/polypyrrole nanorods in nitrogen and oxygen ambient

Milena Šetka[1a], Jana Drbohlavová[1,2], Stella Vallejos[1], Eduard Llobet[3], Jaromír Hubálek[1,2]
[1]Central European Institute of Technology, Brno University of Technology, Purkyňova 123, 612 00 Brno, Czech Republic
[2]Department of Microelectronics, Faculty of Electrical Engineering and Communication, Brno University of Technology, Technická 3058/10, 616 00 Brno, Czech Republic
[3]Minos-Emas, Universitat Rovira i Virgili, Av. Pasios Catalans 26, 43007 Tarragona, Spain

Abstract

This work describes the preparation of gold/polypyrrole nanorods (AuPPy NRs) using anodized alumina oxide (AAO) template and both pulsed galvanic deposition and electropolymerization for the deposition of Au and polypyrrole (PPy) nanorods (NRs), respectively. Characterization of the whole structure after AAO etching revealed the formation of a high density of NRs along the substrate with uniform diameters of approximately 50 nm and total lengths of 700 nm, the last corresponding to 1/3 and 2/3 of the length of the Au and PPy NRs, respectively. The Raman spectroscopy characterization of AuPPy NRs, and its interaction with nitrogen (N_2) and oxygen (O_2) are provided in this work.

1. Introduction

Gold nanostructures have attracted a great attention due to their potential application in chemical and biochemical sensing, medical diagnostics, and biological imaging because of their unique optical and electrical properties, high chemical stability, facile synthesis, surface functionalization and biocompatibility [1]. PPy is one of the most studied and promising conductive polymers thanks to its high conductivity, which results from π-electron conjugation. The π-electron conjugation belongs to single and double bonds of chains in the aromatic ring of PPy. This material has a p–type conductive behaviour and it is attractive due to its unique features such as fast charge-discharge mechanism, high energy density, good thermal stability, and low cost production [2].Therefore, in this work we focus on the fabrication of nanostructured inorganic/organic frameworks of AuPPy NRs.

2. Experimental part

AuPPy NRs were synthesized via combination of three techniques: electrochemical anodization, pulsed galvanic deposition and electropolymerization in a two electrode system with potentiostatic (constant potential) mode.

Four-inch Si wafer (cut it into pieces (1.5x1.5 mm)) covered with 1 µm layer of SiO_2 was used as starting substrates. Subsequently, Ti (20 nm thick), W (150 nm thick) and Al (500 nm thick) layers were sputter-deposited by ion beam sputtering method using a RFICP Kaufman ion-beam source (KRI®).

The electrochemical anodization of Al and W was carried out in 0.3 M oxalic acid at 40 V with the electrolyte temperature at 10 °C. These conditions led to the transformation of Al layer into the nanoporous AAO template, oxidizing the bottom W layer and creating WO_3 nanodots, which were selectively etched in a phosphate buffer solution (pH= 7, T= 25 ^{0}C). This etching process created W nano-dimpled structure on the surface, which were used as a base for the Au NRs to improve their stability.

Next, pulsed galvanic deposition of Au was carried out in potassium dicyanoaurate solution (35 pulses, pulse length of 400 ms, period between pulses of 2 s, 1 mA, 5 V). After 1/3 of AAO pores were filled with Au, the electrochemical deposition of PPy was performed. Thus, PPy was deposited applying a voltage of 2 V for 120 s during the electropolymerization. The PPy reaction was carried out in a solution, containing a mixture of Py monomer and anionic doping salt, $TEABF_4$, with the molar ratio 2:1, dissolved in acetonitrile solvent. Finally, the AAO template was selectively etched in the aqueous solution of chromium trioxide and phosphoric acid at 60 °C for 600 s.

Morphology analysis was examined by TESCAN MIRA II field emission SEM. Raman analysis was carried out using a Renishaw InVia Raman microscope employing 633 nm laser beam, and the spectra were recorded at a power lower than 1 mW using 20× objective.

3. Results and discussion

3.1. Morphology analysis

---

[a] milena.setka@ceitec.vutbr.cz

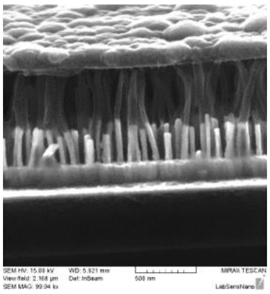

Figure **1**. presents a SEM image of the AuPPy NRs. It can be seen that AuPPy NRs appeared in the 'sandwich structure', connected from the bottom part with the metallic layer of W (100 nm thick) and from the top part covered with the over deposited layer of PPy (100 nm thick). AuPPy NRs arrays were grown perpendicularly to the W layer, and they are well packed and have uniform diameters of 50 nm. The total length of the AuPPy NRs is 700 nm, from which Au and PPy parts take 1/3 and 2/3 of the total length, respectively. SEM imaging confirmed that almost each pore of the template is filled with AuPPy NRs, which indicates a good efficiency and high density of nanorods arrays along the substrate.

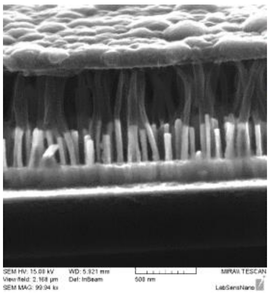

Figure 1. SEM image of the AuPPy NRs after the etching of Al_2O_3, electropolymerization time of 120 s.

3.2. Raman spectroscopy analysis

Raman spectroscopy was performed to characterize the the AuPPy NRs, either in open air (reference-spectra) or in a continuous flow of N_2 or O_2. Figure 2 shows the Raman spectrum of AuPPy NRs, before and after the exposure to N_2 and O_2 for 5 min at room temperature.

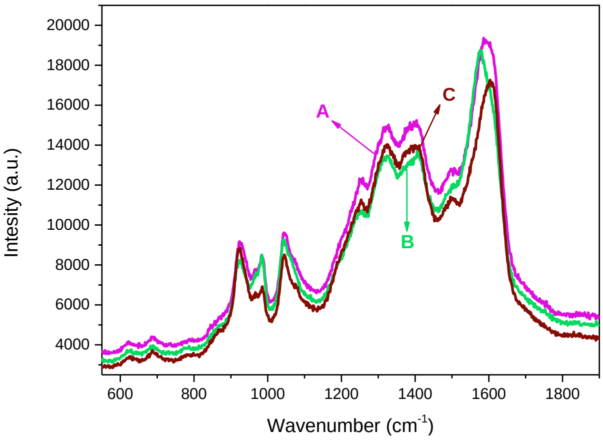

Figure 2. Raman spectrum of: **A**-AuPPy NRs, **B**-AuPPy NRs after the exposure to 5 min of N_2, **C**-AuPPy Nrs after exposure to 5 min of O_2

The reference Raman spectra obtained for AuPPy NRs correspond to PPy, with the peak appearing at 1592 cm^{-1} being related to the C═C backbone stretching [3]. The PPy peaks located at 1560, 1580, and 1610 cm^{-1} are associated with neutral, oxidized (polaronic), and fully oxidized (bipolaronic) bands, respectively[4]. We observed that the exposure of the AuPPy NRs to N_2 shifts the C═C backbone stretching peak to lower wavenumber (1575 cm^{-1}), whereas the exposure to O_2 shifts the peak to higher wavenumber (1605 cm^{-1}). These peak shifts suggest a fully oxidized PPy after O_2 exposure, whereas the smaller wavenumber observed after N_2 exposure indicate C═C backbone stretching peak in a range between neutral and oxidized PPy [5]. On the other hand, peaks at 1406 and 1320 cm^{-1} are attributed to the antisymmetric C–N stretching of PPy, whereas the peak at 1258 cm^{-1} is assigned to the ring stretching of the PPy [6], and the peaks located at 1074 and 1045 cm^{-1} to the symmetrical C–H in-plane bending [7]. These peaks did not displayed a significant change after the exposure to N_2 or O_2. However, peaks at 984 and 927 cm^{-1}, associated to the polaron and bipolaron structure and assigned to ring deformation vibrations [6] show significant changes after the exposure to N_2 or O_2. For instance, the intensity of the polaron peak decreased with respect to the reference spectra after the exposure to O_2, inducing a deformation of the peak's shape. In contrast, the intensity of the bipolaron peak increased with O_2. This fact is consistent with the C═C backbone stretching peak shift to the fully oxidized (bipolaronic) bands of AuPPy NRs after the O_2 exposure. As O_2 is an electron acceptor, it causes the oxidation of polymer chain, removing the free electrons form polarons (cations) and changing them in bipolarons (dications). Reversely, when AuPPy NRs are exposed to N_2, the polarons increase noticeable with a subtle change in the bipolarons as noticed by the changes in the intensity of these peaks in Figure 2.

4. Conclusions

In summary, the synthesis of inorganic/organic framework in 'sandwich structure' containing AuPPy NRs with diameters of 50 nm and lengths of 700 nm has been developed. The Raman spectra of these samples demonstrated to be in agreement with those reported previously for PPy. Further Raman characterizations in a flow of O_2 or N_2 revealed the oxidation and neutralization of the AuPPy NRs, respectively, suggesting the potential of these structures for their use in gas sensing.

References

[1] PENG, G. et al. Diagnosing lung cancer in exhaled breath using gold nanoparticles. *Nature Nanotechnology*, 2009, vol. 4, no. 10, pp. 669-673. ISSN 1748-3387.

[2] ŠETKA, M. et al. Nanostructured Polypyrrole-Based Ammonia and Volatile Organic Compound

Sensors. *Sensors*, 2017, vol. 17.

[3] LIU, Y. C. Characteristics of vibration modes of polypyrrole on surface-enhanced Raman scattering spectra. *Journal of Electroanalytical Chemistry*, 2004, vol. 571, no. 2, pp. 255-264. ISSN 0022-0728.

[4] LIU, Y.-C. et al. In situ cyclic voltammetry-surface-enhanced Raman spectroscopy: studies on the doping–undoping of polypyrrole film. *Thin Solid Films*, 2000, vol. 374, no. 1, pp. 85-91. ISSN 0040-6090.

[5] ISHPAL a KAUR, A. Spectroscopic and electrical sensing mechanism in oxidant-mediated polypyrrole nanofibers/nanoparticles for ammonia gas. *Journal of Nanoparticle Research*, 2013, vol. 15, no. 5, pp. 1637. ISSN 1572-896X.

[6] LI, M. et al. Polypyrrole nanofiber arrays synthesized by a biphasic electrochemical strategy. *Journal of Materials Chemistry*, 2008, vol. 18, no. 19, pp. 2276-2280. ISSN 0959-9428.

[7] LIU, Y.-C. a HWANG, B.-J. Identification of oxidized polypyrrole on Raman spectrum. *Synthetic Metals*, 2000, vol. 113, no. 1–2, pp. 203-207. ISSN 0379-6779.

Organic Solar Cells Based on Azafullerene Acceptors

Montero-Rama, M.P; Viterisi, A and Marsal, L.F*

Departament d’Enginyeria Electrónica, Eléctrica i Automática, ETSE, Universitat Rovira i Virgili. Avda. Països Catalans, 26, 43007 Tarragona, Spain, E-mail: mariadelpilar.montero@urv.cat; aurelien.viterisi@urv.cat; Corresponding author: lluis.marsal@urv.cat; Tel: (+34) 977 55 85 24

Abstract

Bulk Heterojunction (BHJ) solar cells were fabricated based on blended films of a PTB7 (Figure 1) polymer and library of five different azafullerenes (AF) (Figure 2).

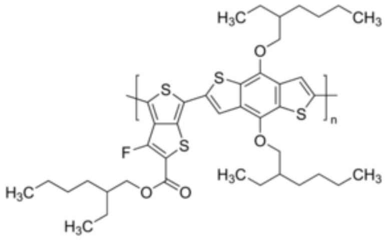

Fig.1.PTB7

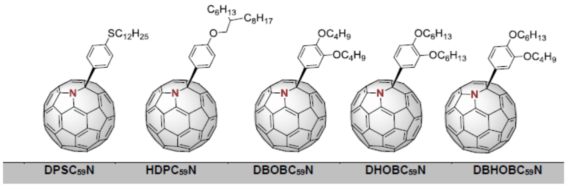

Fig.2. Azafullerenes

1. Introduction

Organic Solar Cells (OSCs) have attracted great interest in the field of renewable energy, due to their recent increase in power conversion efficiency, their potential low manufacturing costs and the expectation of a longer life. [1] Most research has focused on Bulk Heterojunction (BHJ) Polymers Solar Cells (PSCs), whose active layer is composed of bicontinuous donor and acceptor phases. This increases the interfacial area between the donors and acceptors, where the exciton dissociation occurs. The most common donor are polymers and the most common acceptors are fullerenes ($PC_{70}BM$). [2] Although PCBM fullerenes have been by far the most used acceptors, alternative fullerenes with stronger absorption in the visible region have been considered in recent years. For example, Cambarau et. al have synthesized an azafullerene (AF) and applied it to P3HT-based solar cells. They demonstrated that the azafullerene accounted for enhanced light absorption in the visible region compared to $PC_{60}BM$ without affecting the frontier orbital energies. The results of their study suggested that the enhanced absorption leads to an increase of almost 10% in the short circuit current (Jsc) in comparison with reference devices. [3] Herein we set out to extend this study with a library of five parent azafullerenes. These new acceptors were functionalized as to provide enhanced solubility and crystallinity.

2. Experimental and Results

Fabrication of solar cells: The BHJ solar cells were prepared as follows: The pre-patterned ITO substrates were cleaned by ultra-sonication in semiconductor-grade acetone, methanol and isopropyl alcohol and afterwards dried in a stream of nitrogen. Then the ITO was exposed for 30 min to the UV/ozone treatment in order to remove residual organic impurities. The hole transport material (PEDOT:PSS) was spin-coated on the top of the ITO surface (two steps: 4800 rpm and second at 3500 rpm for 30 s each), yielding a film thickness of *ca.* 30 nm, and subsequently annealed at 120ºC for 15 min in an inert atmosphere glove box. The PTB7/AF (donor/acceptor) blend solutions were prepared from a 1:1 D/A weight ratio in Chloroform (10 mg/mL total weight concentration) with 3% w/w of DIO additive. The blend solution were dissolved by ultra-sonication for 30 min. and then left at 50ºC under stirring overnight. PTB7/AF active layers were deposited by spin coating at different rpms: 700, 1000, 1300 and 1600 rpm, for 30 s on top of the ITO/PEDOT:PSS surface. The solution was sonicated for 30 min, and was filtered with a 0.2µm filter prior to deposition. After spin-coating, the samples were placed in a thermal evaporator and a Ca layer (20nm) and an Ag layer (100nm) were deposited under high vacuum ($1x10^{-6}$ mbar). The active area of the devices were 0.09 cm^2. Figure 3 shows the structure of the solar cells.

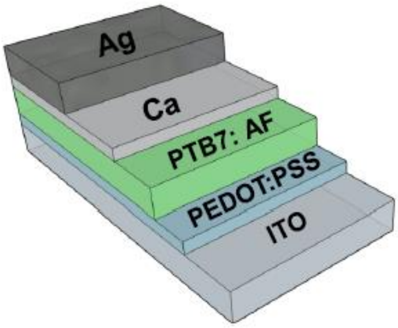

Fig 3. Schematic structure of BHJ solar cells

Solar cells characterization: The *J-V* characteristics of the devices were recorded using a Sun 2000 solar simulator (150W, ABET Technologies). The illumination intensity was measured to be 100mW/cm2 with a calibrated silicon photodiode (NREL). The results are summarized in the following tables (1-5) for each fullerene, and the *J-V* characteristics of the best performing devices plotted in Figure 4.

	rpm	**Voc (V)**	**Jsc (mA/cm^2)**	**FF**	**η (%)**
A$_1$d$_1$	700	699.9	6.33	39	1.74
A$_2$d$_2$	1000	699.9	6.20	41	1.79
A$_3$d$_3$	1300	699.9	6.37	41	**1.89**
A$_4$d$_1$	1600	699.9	5.96	42	1.75

Table1. Devices with PTB7/DPSC$_{59}$N active layer. Voc is the open circuit voltage, Jsc is the short current circuit density, FF the fill factor and η the efficiency.

	rpm	**Voc (V)**	**Jsc (mA/cm^2)**	**FF**	**η (%)**
B$_1$d$_1$	700	679.9	2.2	33	0.49
B$_2$d$_1$	1000	680.1	2.5	32	0.55
B$_3$d$_4$	1300	679.9	2.6	32	0.53
B$_4$d$_2$	1600	679.9	2.7	33	**0.60**

Table2 Devices with PTB7/HDPC$_{59}$N active layer. Voc is the open circuit voltage, Jsc is the short current circuit density, FF the fill factor and η the efficiency.

		rpm	**Voc (V)**	**Jsc (mA/cm^2)**	**FF**	**η (%)**
C$_1$d$_4$		700	579.8	1.9	34	0.37
C$_2$d$_1$		1000	639.9	2.2	33	0.45
C$_3$d$_3$		1300	619.9	1.9	33	0.41
C$_4$d$_2$		1600	629.9	2.3	33	**0.46**

Table3. Devices with PTB7/DBOBC$_{59}$N active layer. Voc is the open circuit voltage, Jsc is the short current circuit density, FF the fill factor and η the efficiency.

	rpm	**Voc (V)**	**Jsc (mA/cm^2)**	**FF**	**η (%)**
D$_1$d$_3$	700	659.9	2.52	36	0.60
D$_2$d$_1$	1000	659.9	2.87	35	**0.67**
D$_3$d$_2$	1300	659.9	2.97	33	0.65
D$_4$d$_4$	1600	659.9	2.55	36	0.61

Table4. Devices with PTB7/DHOBC$_{59}$N active layer. Voc is the open circuit voltage, Jsc is the short current circuit density, FF the fill factor and η the efficiency.

	rpm	**Voc (V)**	**Jsc (mA/cm^2)**	**FF**	**η (%)**
E$_1$d$_1$	700	559.9	0.54	0.29	0.089
E$_2$d$_2$	1000	570.0	0.56	0.29	**0.095**
E$_3$d$_4$	1300	570.0	0.62	0.29	0.083
E$_4$d$_3$	1600	570.0	0.59	0.29	0.085

Table5. Devices with PTB7/DBHOBC$_{59}$N active layer. Voc is the open circuit voltage, Jsc is the short current circuit density, FF the fill factor and η the efficiency.

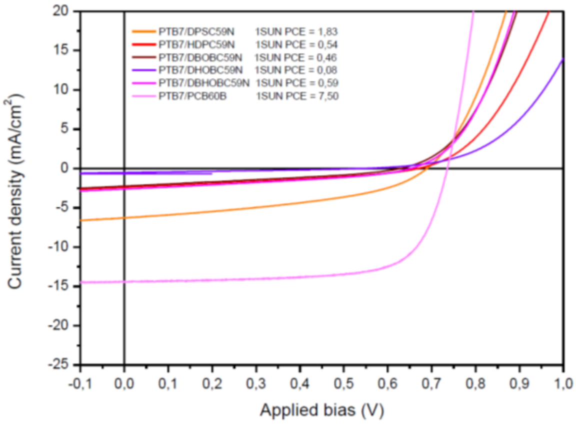

Fig 4. *J-V* Characteristics of devices made from each fullerene in comparison with the PTB7/PCB60B reference device. (at 1 SUN). PCE is the power conversion efficiency.

3. Conclusions

We observed that devices fabricated with PTB7/DPSC$_{59}$N as active layer exhibited the highest efficiency among all azafullerenes. On the other hand, the solar cells made from the PTB7/DBHOBC$_{59}$N blend exhibited the lowest PCE. In addition, samples with PTB7/HDPC$_{59}$N, PTB7/DBOBC$_{59}$N and PTB7/DHOBC$_{59}$N led to similar results. We demonstrated that, to some extent, the efficiency is linked to the active layer thickness. In samples with PTB7/DPSC$_{59}$N the best results were obtained using 1300 rpm in the spin coating process, while in samples with PTB7/DHOBC$_{59}$N and PTB7/DBHOBC$_{59}$N the best results were obtained at 1000 rpm. In samples made from PTB7/HDPC$_{59}$N and PTB7/DBOBC$_{59}$N the best results were obtained with very thin active layers. Further works will focus on the improvement of solar cells characteristics using the azafullerene DPSC$_{59}$N by modifying several fabrication variables such as the polymer:azafullerene ratio, solvent:DIO concentration and layer thickness.

4. Acknowledgment

This work was supported in part by the Spanish Ministry of Economy, Industry and Competitiveness (MEIC) under grant numbers TEC2015-71324-R and TEC2015-71915-REDT, the ICREA under the ICREA Academia Award and the Catalan authority under project AGAUR 2014 SGR 1344.

5. References

[1] Nevena Marinova, Silvia Valero, Juan Luis Delgado, "Organic and perovskite solar cells: Working principles, materials and interfaces" Journal of Colloid and Interface Science 488 (2017) 373-389.

[2] Barry C. Thompson and Jean M.J. Fréchet, "Polymer-Fullerene composite solar cells" Angew. Int. Ed. 200/8, 47, 58-77.

[3] Werther Cambarau, URs F. Fritze, Aurelien Viterisi, Emilio Palomares and Max von Delius, "Incresed short circuit current in an azafullerene-based organic solar cell", Chemcomm, 2014, 00, 1-3.

Output voltage regulation of a boost converter with constant power load by means of sliding mode control

Blanca A. Martínez-Treviño, Abdelali El Aroudi, and Luis Martínez-Salamero
Universitat Rovira I Virgili (URV), Tarragona,Spain, Email: blancaareli.martinez@urv.cat

***Abstract*—Cascade connection of DC-DC switching converters is often required in multi-converter systems with the aim of distributing power in electric vehicles or renewable energy installations. The resulting electrical architecture involves the cascade connection of converters. In the connection of two converters, the first one is called source while the second one is denominated load.A particular operation mode of this connection arises when the load converter absorbs constant power or, equivalently, when the operation of the source converter supplies a constant power load (CPL). The operation of the load converter absorbing constant power can provoke unstable behavior in the cascade connection, the optimal solution of this problem being still open.**

The work here reported tackles the problem of controlling in sliding-mode a boost converter supplying a constant power load (CPL). A linear switching surface is proposed to overcome the intrinsic unstable behavior of the converter in both on and off states. PSIM simulations are in perfect agreement with the theoretical predictions.

***Keywords*—Power converters, constant power load, sliding-mode control.**

1. BOOST CONVERTER WITH CPL

Fig. 1 shows a boost converter supplying a CPL, which is characterized by the following current-voltage relationship:

$$i_{CPL} = \frac{P}{v_C} \tag{1}$$

where $P > 0$ is the power absorbed by the load and $v_C > 0$ is the output capacitor voltage. The corresponding state equations can be expressed in compact form as follows:

$$\begin{aligned} \frac{dv_C}{dt} &= \frac{i_L}{C}(1-u) - \frac{P}{Cv_C} \\ \frac{di_L}{dt} &= -\frac{v_C}{L}(1-u) + \frac{V_g}{L} \end{aligned} \tag{2}$$

where i_L is the inductor current, V_g is the input voltage and u is a binary signal so that, u=1 during the T_{on} interval and u=0 during the T_{off} interval.

A. Equilibrium point locus

The equilibrium points locus (EPL) is obtained assuming that the derivatives of the trajectories in the phase-plane during on and off states are opposite with equal absolute value. Hence, the EPL will be determined by:

$$i_L = \frac{P}{V_g} \tag{3}$$

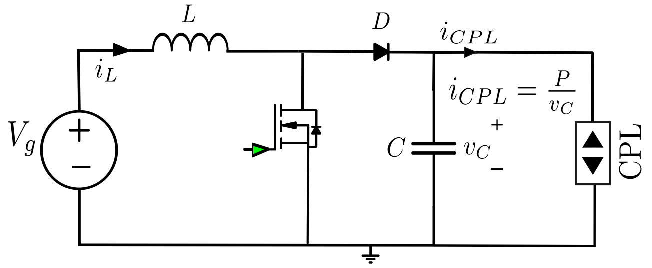

Fig. 1. Boost converter with CPL.

2. SLIDING MODE CONTROL

In order to drive the system to EPL in spite of the unstable behavior of T_{on} and T_{off} states, the following linear surface, $\Sigma = \{x | S(x) = 0\}$, is proposed:

$$S(x) = K_C(v_C - V_{REF}) + K_i(i_L - I_{REF}) \tag{4}$$

where V_{REF} and I_{REF} are the reference values for the capacitor voltage and inductor current respectively and K_C and K_i are positive constants. The equilibrium point $({i_L}^*, {v_C}^*)$ will be given by the intersection of (3) and (4) leading to:

$$({i_L}^*, {v_C}^*) = \left(I_{REF} = \frac{P}{V_g}, V_{REF}\right) \tag{5}$$

The control law can be expressed as follows

$$\begin{aligned} &\text{u} = 0 \quad \text{when} \quad S(x) > 0 \\ &\text{u} = 1 \quad \text{when} \quad S(x) < 0 \end{aligned} \tag{6}$$

There will exist sliding motions if the reachability condition $\dot{S}S < 0$ is satisfied. Hence, the region of sliding motions is determined by the following inequality.

$$i_L < \frac{1}{v_C}\left(\frac{CK_i}{LK_C}{v_C}^2 + P\right) - \frac{CK_iV_g}{LK_C} \tag{7}$$

Fig. 2 shows EPL, $S(x)$ and the region for the existence of sliding motions (ESM). Note that ESM is colored in grey.

Besides, the ideal sliding dynamics corresponding to the average trajectory of the converter on the switching surface will be expressed in terms of the equivalent control (u_{eq}) by imposing the conditions $S = 0$ and $\dot{S} = 0$ leading to:

$$u_{eq} = 1 - \frac{K_CLP - K_iCV_gv_C}{v_C(LK_CI_{REF} - v_C(\frac{LK_C{}^2}{Ki} + CK_i) + \frac{V_{REF}LK_C^2}{K_i})} \tag{8}$$

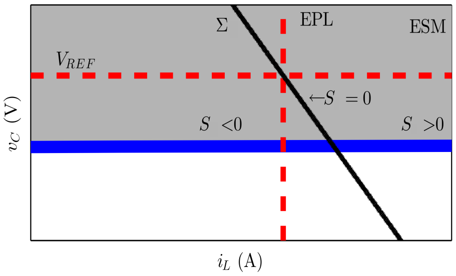

Fig. 2. Phase-plane depiction of switching surface Σ_1, EPL and ESM

In steady-state the previous expression becomes

$$u_{eq_{ss}} = 1 - \frac{V_g}{V_{REF}} \tag{9}$$

The ideal sliding dynamics of the converter, obtained by substituting the control action (u) by the equivalent control (u_{eq}) in the state equations in (2), is as follows:

$$\frac{dv_C}{dt} = \frac{\left(K_1 {v_C}^2 + K_2 v_C + K_3\right)}{C(K_4 {v_C}^2 + K_5 v_C)} - \frac{P}{C v_C} = f_{v_C}(v_C) \tag{10}$$

where:

$$K_1 = K_C K_i C V_g$$
$$K_2 = -({K_i}^2 I_{REF} C V_g + K_C K_i C V_{REF} V_g + L {K_C}^2 P)$$
$$K_3 = K_C K_i I_{REF} L P + L {K_C}^2 V_{REF} P$$
$$K_4 = -(L {K_C}^2 + C {K_i}^2)$$
$$K_5 = L K_C K_i I_{REF} + L {K_C}^2 V_{REF}$$

From (4) and (10) the coordinates of the equilibrium point will be given by $(P/V_g, V_{REF})$, which corresponds to the desired values given by (5).

The ideal sliding dynamics will be stable if $(df_{v_C}/dv_C|^*_{v_C}) < 0$, which implies that:

$$P > P_{min} \tag{11}$$

where,

$$P_{min} = \frac{V_g I_{REF} + K_C V_{REF} V_g}{\frac{{K_C}^2}{{K_i}^2}\frac{L}{C} + 1} \tag{12}$$

3. SIMULATION RESULTS

The proposed controller is validated by PSIM simulations illustrating the effect of the linear switching surface coefficients, the converter start-up and its response in front of input and load variations for the set the parameters V_g=200 V, L=50 μH, C=10 μF, P=3 kW and V_{REF}=350 V. The controller uses a hysteric comparator with a hysteresis band (H) in order to obtain a finite switching frequency. Furthermore, an auxiliary diode branch connecting input and output voltage has been added to mitigate the inrush current.

Fig. 3 illustrates the effect of the linear switching surface parameters on the inrush current. It can be noted that the smallest inrush current is achieved with combination 5 but the corresponding output voltage response is slower than the one obtained with combination 1. For that reason, in order to obtain a good compromise between a low inrush current and fast output voltage response, combination 4 has been selected for the switching surface.

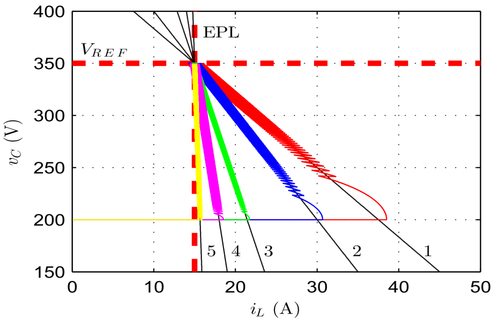

Fig. 3. Switching surfaces with different values of K_i, K_C given by 1:(1,15), 2:(1.5,15), 3:(3.5,15), 4:(1,2) and 5:(4.5,2) respectively.

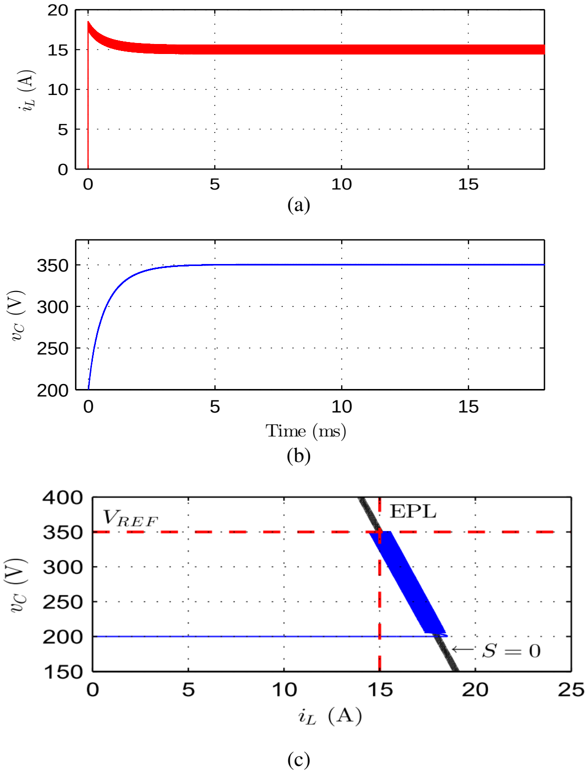

Fig. 4. Converter current and voltage waveforms corresponding to the proposed SM control during start-up.

Fig. 4 shows the converter start-up and the steady-state behavior, the latter being in close agreement with the theoretical prediction given by (5). Note the first order behavior exhibited by the state variables due to the one order reduction introduced by the sliding motion. Besides, the steady-state is attained in a relatively short time.

Fig. 5 shows the converter response for a load change of step type from 3 kW to 3.5 kW. Note that the voltage capacitor remains constant while the inductor current absorbs the load variation. On the other hand, a step perturbation in the input voltage has been simulated in Fig. 6 by changing it from

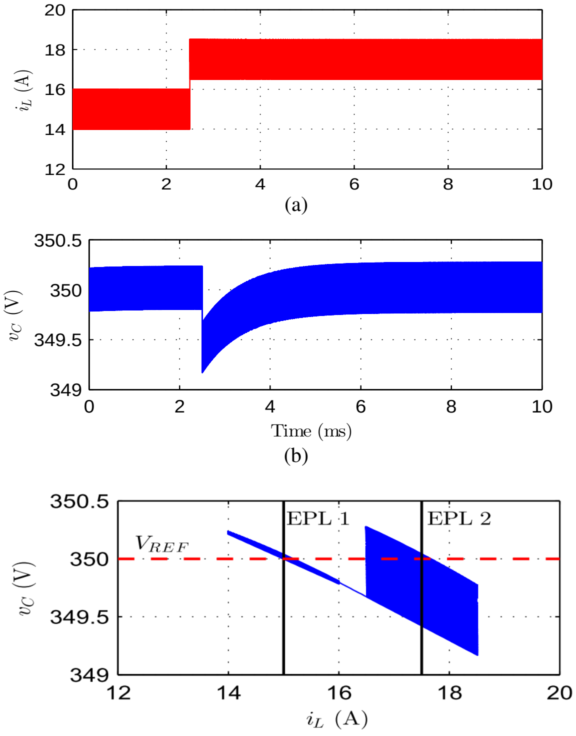

(a)

(b)

(c)

Fig. 5. Simulated response for a step load perturbation. (a) Inductor current waveform, (b) Capacitor voltage waveform, (c) Phase-plane trajectory.

200 V to 250 V. Also, besides a fast recovery of the output voltage, the inductor current coordinate in the equilibrium point changes from EPL 1 to EPL 2, mitigating the effect of the disturbance.

4. CONCLUSIONS

Sliding-mode control based on the use of a linear switching surface has proven to be an effective solution to regulate a boost converter feeding a CPL. The switching surface leads to small values of inrush current and guarantees output voltage regulation in face of load perturbations and input voltage variations. The theoretical predictions have been verified by PSIM simulations.

ACKNOWLEDGMENT

This work was supported by the Spanish Ministerio de Ciencia e Innovación under grant DPI2013-47293-R, DPI2016-80491-R and DPI2015-67292-R.

REFERENCES

[1] A. Emadi and A. Ehsani, “Dynamics and control of multi-converter dc power electronic systems,” in *Power Electronics Specialists Conference, 2001. PESC. 2001 IEEE 32nd Annual*, vol. 1. IEEE, 2001, pp. 248–253.

[2] M. Belkhayat, R. Cooley, and A. Witulski, “Large signal stability criteria for distributed systems with constant power loads,” in *Power Electronics Specialists Conference, 1995. PESC’95 Record., 26th Annual IEEE*, vol. 2. IEEE, 1995, pp. 1333–1338.

[3] A. Emadi, A. Khaligh, C. H. Rivetta, and G. A. Williamson, “Constant power loads and negative impedance instability in automotive systems: definition, modeling, stability, and control of power electronic converters and motor drives,” *IEEE Transactions on Vehicular Technology*, vol. 55, no. 4, pp. 1112–1125, 2006.

[4] V. Utkin, J. Guldner, and J. Shi, *Sliding mode control in electromechanical systems*. CRC press, 2009, vol. 34.

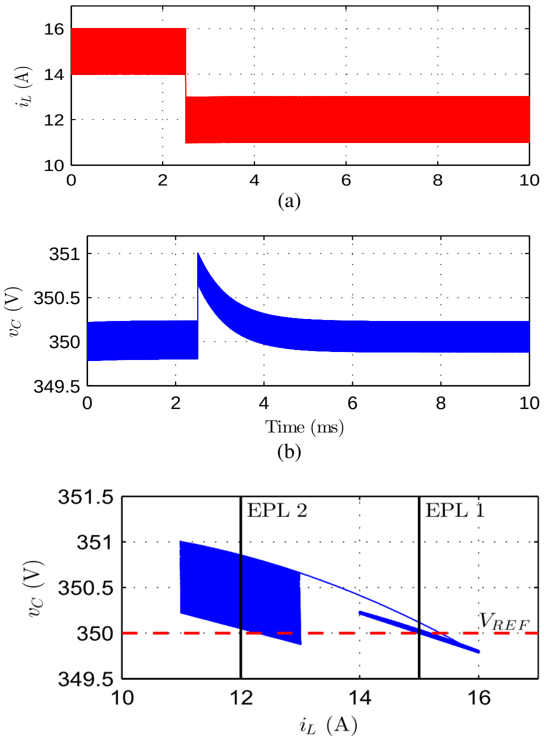

(a)

(b)

(c)

Fig. 6. Simulated response for a step input voltage perturbation. (a) Inductor current waveform, (b) Capacitor voltage waveform, (c) Phase-plane trajectory

Low-Power Isolated DC/DC Converters for Mismatch Mitigation in Photovoltaic Systems

Md Nazmul Hasan, Luis Martinez-Salamero and Carlos Olalla
Dept. of Electrical, Electronics and Automatic Control Engineering
Rovira i Virgili University, Tarragona, Spain.
mdnazmul.hasan@urv.cat

Abstract— To mitigate the ageing related mismatch, Differential Power Processing (DPP) is one of the possible solution. Differential Power Processing (DPP) has several advantages over Full Power Processing (FPP), such as improved efficiency, reduction of power rating of the converter as well as the size, weight and cost. In order to balance currents in DPP architectures, DC-DC converters require bidirectional power transfer, 1:1 conversion ratio and isolation between the input and the output. Two possible candidates featuring these properties are the Ćuk and the LLC resonant converter. In this report, a comparative study has been done between these two candidates. The comparison has considered the cost, efficiency, simplicity of control, robustness and practical realization of the converter parameters.

Keywords—DPP, LLC, ĆUK, DC-DC transformer

I. INTRODUCTION

Differential power processing (DPP) has been proposed as an alternative to µ-inverters and dc optimizers in order to mitigate the effects of mismatch in photovoltaic (PV) systems [1]-[5]. DPP architectures typically feature DC-DC converters named subMICs, which are connected at submodule level and replace bypass diodes. The approach has been demonstrated to be effective in PV systems affected by partial shading, increasing the energy yield by more than 5% [6].

DPP has also been proposed to reduce the effects of ageing mismatch in unshaded unity-scale PV systems [6]. In absence of shading, only small currents are processed and the low power efficiency of the converter is a relevant parameter. In this report, a qualitative comparison has been done first between Ćuk and LLC resonant converter. Later, by taking in to account power conversion losses, simulation has been done to evaluate the efficiency of these two converters.

II. SPECIFICATIONS OF THE SUBMIC CONVERTER

In a previous study [6], it was shown that a converter rating of 20% of the submodule rating could provide full mitigation in the case of ageing related mismatches during 25 years. Based on this fact, the power ratting of the converter has been considered to be 20% of the maximum power rating of the submodule. In the case of a Trina TSM-230PC05 module, this results in a power rating of 15 W. The remaining specifications of the converter are presented in Table I, where an arbitrary switching frequency of 100 kHz has been considered in order to carry out the comparison.

Table I: Specification of the converter.

Input voltage(V)	10
output voltage(V)	10
Switching frequency(kHz)	100
Power Output Max(W)	15

III. SUBMIC DESIGN

A. *Design of the LLC converter*

In order to recover fully symmetrical bidirectional power transfer, an additional resonant tank in the secondary side of the transformer of the conventional LLC converter has been proposed, such that a fully symmetrical tank can be obtained, as shown in Fig.1. Since the additional tank will act as series resonant tank, at resonant frequency of unity gain, the converter will act as a conventional LLC converter; additionally fully symmetrical bidirectional power transfer can be achieved.

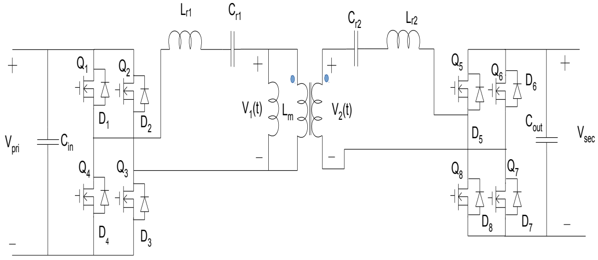

Figure 1: Bidirectional isolated LLC converter

By following the method in [8], the parameters of the LLC resonant converter for 1W-15W are as follows. The resonant inductance is 25µH, the resonant capacitance is 0.1µF and the magnetizing inductance of the transformer is 125µH. With these parameters output voltage ripple of the LLC converter can be found as 9.5mV with 100µF output capacitor. Following the design procedure of [7], with a pot core 905 can be used for the transformer.

B. *Design of the Cuk converter.*

For a fair comparison the parameters considered for the LLC converter has also used for the Ćuk converter. A bidirectional isolated Ćuk converter is shown Fig.2. The transformers of the converters as well as the coupled inductor of the Ćuk converter have been designed by following the procedure described in [7]. The size of the core required for the transformer is same as the transformer of the LLC converter. However for realization of the input-output inductor an extra core of EE12 has been used. With the same size of output capacitor the output voltage ripple of 12.5mV has been observed.

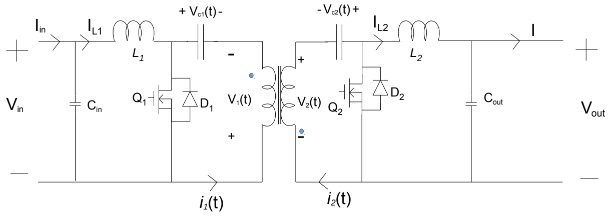

C. *Qualitative comparison*

The transformer utilization factor is the same for the Ćuk and the LLC converter. However, in the Ćuk converter, the switch has to withstand at least an off-voltage of $2V_g$. On the contrary, in the LLC converter, the switch has to experience only an off-voltage equal to the input voltage.

The resonant inductor of the LLC can be integrated in the transformer using the leakage inductance. LLC converter has the ability to be operated in ZVS and ZCS modes, which significantly reduces the switching losses. However LLC converter requires a large number of switches, which may offset the advantage of ZVS/ZCS. Whereas the Ćuk converter requires less switches which provide simplicity in control and low cost. Another important advantage is that as the switches are connected to the low voltage side, much simpler driver circuitry can be used. However, the Ćuk converter is typically operated in hard-switched mode which can reduce efficiency significantly specially at low power. Another disadvantages regarding the Ćuk converter is it usually requires different cores for the inductors and transformer. In summary, each converter has its own advantages and disadvantages. The following section tries to classify which topology is suited for the realization of very low power conversion subMICs.

IV. COMPARISION OF THE LLC AND THE CUK CONVERTER AS LOW POWER SUBMICS

With the aim of comparing the conduction losses analytical expressions have been derived to calculate the efficiency of LLC and Ćuk converter. Later simulation with PSIM software has been done with the exactly the parameters to justify the mathematical model. If Inductors of the Ćuk converter can be combined in a single core; the effective inductance will be doubled. That is why simulation and the algorithm have been constructed considering that the primary inductance is 25 µH and the secondary inductance is also 25 µH instead of 12.5 µH. Figure.3 shows the efficiency curves of Ćuk and LLC converter. It should be noted that effect of leakage inductance has also been considered.

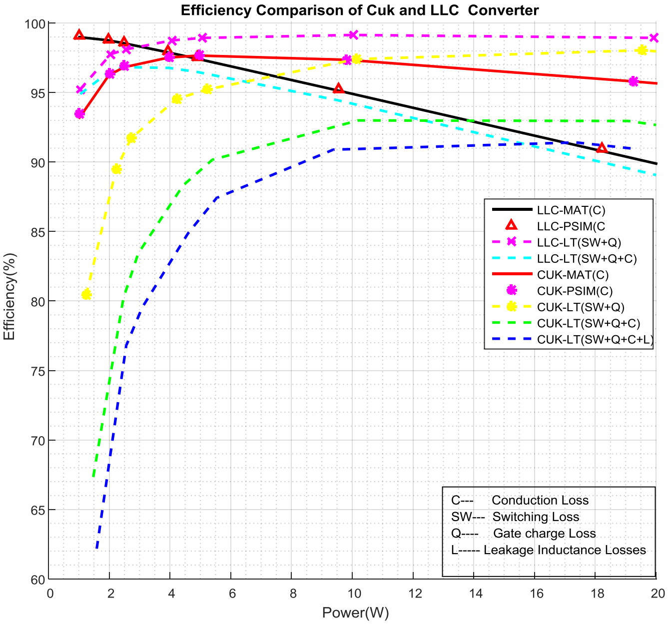

Figure 3: Efficiency of the LLC and the Ćuk converter

V. CONCLUSION

In this article, an overall comparison of performance has been done between the Ćuk and the LLC converter for photovoltaic system application. It can be seen that at low power the LLC converter provides an efficiency of close to 95% at 1W with a maximum efficiency of 97% at 2 to 5 W. The efficiency remains above 90% even after 15W. One the contrary, due to leakage inductance and hard switching nature of Ćuk converter, at low power, this converter provides low efficiency. But as the power goes above 7 watt, the efficiency reaches to more than 90%.

References

[1] P. S. Shenoy, K. A. Kim, B. B. Johnson, and P. T. Krein, “Differential power processing for increased energy production and reliability of photovoltaic systems,” IEEE Trans. Power Electron., vol. 28, no. 6, pp. 2968–2979, 2013.

[2] Y. Nimni and D. Shmilovitz “A returned energy architecture for improved photovoltaic systems efficiency,” in Proc. IEEE Int. Symp. Circuits Sys. 2010, pp. 2191–2194

[3] J. Stauth,M. Seeman, and K. Kesarwani, “A high-voltage CMOS IC and embedded system for distributed photovoltaic energy optimization with over 99% effective conversion effciency and insertion loss below 0.1%,” in Proc. IEEE Int. Solid-State Circuits Conf., 2012, pp. 100–102.

[4] C. Olalla, M. Rodriguez, D. Clement, and D. Maksimovic, “Architectures and control of submodule integrated DC-DC converters for photovoltaic applications,” IEEE Trans. on Power Electron., vol. 28, no. 6, pp. 2980–2997, 2012.

[5]T. Shimizu, M. Hirakata, T. Kamezawa, and H. Watanabe, “Generation control circuit for photovoltaic modules,” IEEE Trans. Power Electron., vol. 16, no. 3, pp. 293–300, 2001.

[6] C. Olalla, C. Deline, D. Clement, Y. Levron, M. Rodriguez, and D. Maksimovic, “Performance of power-limited differential power processing architectures in mismatched pv systems,” IEEE Trans. Power Electron., vol. 30, no. 2, pp. 618–631, 2015.

[7]R.W. Erickson and D. Maksimovic, Fundamentals of Power Electronics. New York: Springer-Verlag, 2001

[8] Sam Abdel-Rahman ,”Resonant LLC Converter: Operation and Design 250W 33Vin 400Vout Design Example” Infineon Technologies North America (IFNA) Corp. 2012

[9] Slobodan Ćuk, “Modelling, Analysis, and Design of Switching Converters, ” Ph.D. thesis, California Institute of Technology, 1976.

[10] “MOSFET Gate-Charge Origin and its Applications Introduction”-OnSemiconductor-AND9083/D-2016

[11] “Ferrite Cores, 2013 catalog” by Magnetics

Piezoelectric Effect in AlGaN/GaN HEMTs

Wondwosen Eshetu Muhea*[1], Fetene Mulugeta Yigletu[2], and Benjamin Iñiguez[1], Senior *Member, IEEE*

[1]Department of Electronics, Electrical, and Automation Engineering, Universitat Rovira I Virgili, 43007, Tarragona, Spain

[2] Department of Electrical and Computer Engineering, University of California Davis, 1 Shields Ave, Davis, CA, USA.
wondwosen.eshetu@urv.cat

Abstract

The effect of polarization charge in AlGaN/GaN HEMTs is studied in this work at a device level. A threshold voltage model that depends on the induced spontaneous and piezoelectric polarization charges and considered the effect of surface donor states is presented. DC transfer and output characteristics of a *0.7µm* device are simulated using the model and verified with experimental data.

1. Introduction

AlGaN/GaN HEMTs are promising candidates for the next generation high frequency and high power applications. The existence of a high density of two dimensional electron gas (2DEG) at the heterojuction interface is the most important feature of these devices that makes them meet the demand of high power electronics. Results of different researches show that the surface donor states residing on the top of AlGaN layer are the source of the 2DEG [1].

In this paper, we extend the DC charge control model presented in [2] to include the effect of spontaneous and piezoelectric induced charges. The dependence of the surface barrier height in the surface donor state density and donor energy level is also considered as well.

2. Threshold voltage model

It is assumed in [1] that the bare surface donor states distribution can be characterized by a constant density of state n_0 and donor level E_d. A simple relation between bare Surface Barrier Height (SBH) $q\phi_b$ and the n_0 and E_d is derived in [1] as:

$$q\phi_b \approx \frac{k_1 d + k_2}{n_0\left(d + k_3\right)} \qquad (1)$$

where $k_1=\sigma_{PZ}/q+n_0E_d$, $k_2=\varepsilon_{AlGaN}\Delta E_c/q^2$ and $k_3=\varepsilon_{AlGaN}\Delta E_c/q^2n_0$, σ_{PZ} is the polarization charge, ΔE_c band gap offset, ε_{AlGaN} the dielectric constant of the barrier layer, and n_0 is the population of surface donor states per unit area below the donor lever E_d.

It is experimentally shown that the formation of a Schottky contact will decrease the SBH as the deposition of the gate metal will partially deplete the surface donor states. This corresponds to a reduction in surface donor density n_0 and donor level E_d. With the assumption that the nature of the surface states remain unchanged, the SBH value after the gate metal deposition can be calculated with a reduced value of n_0 and E_d using (1). From the physics of heterojuctions, the threshold voltage of GaN HEMT is calculated as:

$$V_{off} = q\phi_b - \Delta E_c - \frac{qN_D(d_d)^2}{2\varepsilon} - \frac{q\sigma_{pz}(d_d+d_i)}{\varepsilon} \qquad (2)$$

where $q\phi_b$ is calculated using (1), N_D and d_d is the doping concentration and thickness of the n-AlGaN layer, d_i is the thickness of the un-doped space layer. The total polarization charge σ_{PZ} in (1) and (2) is dependent on the *Al* mole fraction of the barrier layer and is calculated based on the expressions in [4].

3. Results and discussion

We have incorporated the polarization dependent threshold voltage expression in the charge control and the resulting DC model proposed in [2]. Using our model we have simulated DC characteristics of a 0.7µm device. This device has a doped barrier layer thickness (d_d) of 15nm with a spacer layer (d_i) of 3nm. Fig.1 and Fig. 2 show the transfer and output characteristics respectively. The model shows reasonable agreement with the measurement data.

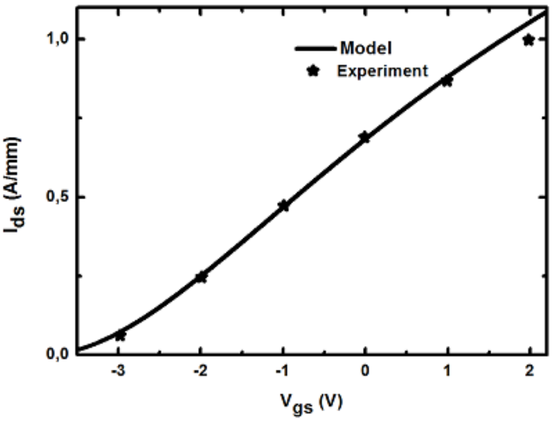

Fig.1. Transfer characteristics of a device with gate length of 0.7μm at Vds=7v (data from [3]).

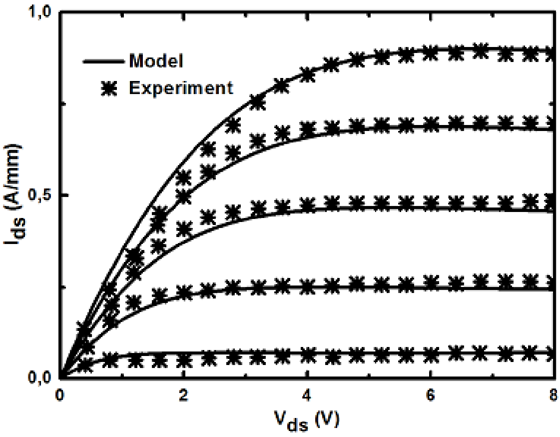

Fig.2. Output characteristics of a device with gate length of 0.7μm. Vgs variy from -3 to 1V (data from [3]).

4. Conclusions

We have presented an expression of the threshold voltage of AlGaN/GaN HEMT incorporating the effects of induced polarization charge, the surface donor states density, and donor energy level. This expression has been incorporated to our DC AlGaN/GaN HEMT model. The model predicts experimental data reasonably well.

References

[1] Nitin Goyal and Tor A. Fjeldly, “Impact of gate metal on surface states distribution and effective surface barrier height in AlGaN/GaN heterostructures”, *Material Research Society, Spring Meeting*, San Francisco, Vol. 1538, USA, April 2013.

[2] F. M. Yigletu, S. Khandelwal, T. A. Fjeldly, and B. Iniguez, “Compact charge-based physical models for current and capacitances in AlGaN/GaN HEMTs,” *IEEE Trans. Electron Devices*, vol. 60, no.11, pp. 3746–3752, 2013.

[3] Y. F. Wu et al., “High Al-content AlGaN/GaN MODFETs for ultrahigh performance,” *IEEE Electron Device Lett*., vol. 19, no. 2,pp. 50–53, Feb. 1998.

[4] O. Ambacher et. al, “Two-dimensional electron gas induced by spontaneous and piezoelectric polarization charge in N-and G-face AlGaN/GaN hetrostructures,” *Appl. Phys*. 85, 3222 (1999).

Bio-Immobilization Strategies in Nanoporous Anodic Alumina for Optical Biosensing via Capillary Filling

Chris Eckstein, Josep Ferré-Borrull, Lluis F. Marsal

Departament d'Enginyeria Electrònica, Elèctrica i Automàtica, Universitat, Rovira i Virgili, Avda. Països Catalans 26, Tarragona 43007, Spain. Contact via chris.eckstein@urv.cat or +34601625951

Abstract

As an optofluidic method, fluid imbibition coupled laser interferometry monitors light interferences of a laser beam caused by capillary filling in real-time. Here we address the accuracy of this method in comparison to classical characterization techniques such as Environmental Scanning Electron microscopy (ESEM) and we found that FICLI provides more consistent radius estimates across two different types of materials. We further advanced FICLI towards a novel biosensing technique by characterizing different bio-immobilization strategies: electrostatic and covalent silane coupling. Bovine Serum Albumin (BSA) was successfully immobilized electrostatically and its dimensions were reasonably estimated across a large size range of pores (15-43nm) and two different types of NAA materials. FICLI was further able to characterize the thickness of a multilayer of the silane coupling agent APTES+GTA and the successful covalent immobilization of Streptavidin.

Introduction

Nanoporous anodic alumina (NAA) is a widely used carrier matrix for optofluidic characterization and sensing devices due to its great tissue compatibility and ease of modification by wet chemical etching and functionalization and immobilization of molecules to the inside walls of the pores. [1,2] We previously presented fluid imbibition-coupled laser interferometry (FICLI) as a novel optofluidic technique to estimate the pore radius of NAA before and after chemical modification by monitoring capillary filling time. [2,3]

FICLI, in brief, monitors light intensity fluctuations of a single wavelength in real-time upon fluid imbibition in NAA. The time difference between adjacent extrema serves as the basis to estimate the pore radius.

We determine the accuracy of FICLI in comparison to traditional methods (ESEM) after a series of pore widening steps for NAA of different as produced radii and materials (sulfuric, oxalic acid).

We then electrostatically immobilized BSA onto the pore walls and assess the effects of as produced radii and NAA material on the detection capability of FICLI.

Finally the characterization of the thickness of silane coupling agent (APTES+GTA) was estimated with FICLI and the covalent immobilization of Steptavidin was assessed.

Materials & Methods

Sample fabrication (in brief)

NAA of 75µm thickness were produced in oxalic acid electrolyte following a two-step anodization protocol. The aluminum bottom was removed by a mixture of $CuCl_2$-HCl (saturated) and 68% HNO_3 and the pores were opened by reactive ion etching. The pore radius was increased by stepwise wet chemical etching with a controlled pore widening time t_{PW}. The pore walls were subsequently hydroxylated in > 30% H_2O_2 and incubated with protein solutions at 4°C overnight.

FICLI

The light intensity of a laser beam reflected off the bottom of an NAA is registered over time. Capillary forces readily draw in a liquid dropped onto the NAA.

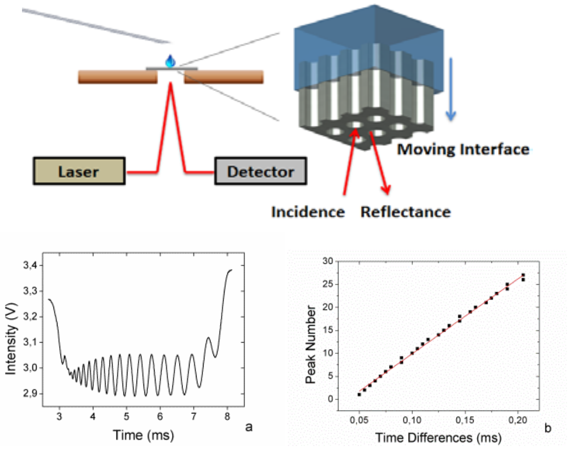

Figure 1: experimental set-up, raw data and time differences over indexed extrema pair.

The moving liquid interface within the pores changes the optical path between the two reflected waves leading to successive intensity extrema. The extrema in the pattern are indexed and the time of occurrence is registered. The time difference between two consecutive extrema is plotted against the extremum index, producing a linear trend. The pore radius can then be estimated from the slope of this linear trend (S) with the expression:

$$R_0 = \left(\frac{\alpha\, L_0{}^6}{S}\right)^{\frac{1}{5}} \text{ with } \alpha = \frac{4\mu}{\pi^2 \gamma \cos\theta} \text{ and } L_0{}^3 = \frac{\lambda}{4(n_2 - n_3)\delta}.$$

Results and Discussion

Figure 2 shows the estimated pore radius as a function of pore widening time (t_{PW}) for NAA produced in oxalic (top) (NAA_{ox}) and sulfuric (bottom) (NAA_{sul}) acid. The radii were estimated by ESEM (black) and FICLI (white). The pore etching rates estimated by ESEM deviate by a factor of 3 between NAA_{ox} and NAA_{sul}. Due to the lack of resolution ESEM image analysis render pore size estimations more uncertain for pores below 30nm. Using FICLI, identical etch rates of 0.8 ± 0.1 nm / min were found for NAA_{ox} and NAA_{sul} which are both in good agreement with the literature. FICLI presents a more robust alternative to traditional methods especially for pores below 30nm.

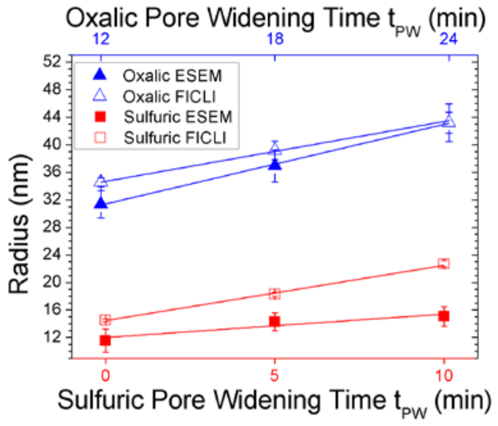

Figure 2: Estimated pore radii as a function pore widening time t_{PW}, obtained by FICLI and ESEM image analysis.

Figure 3 shows estimated radius reductions upon electrostatic BSA immobilization as a function of as produced radius for NAA_{ox} and NAA_{sul} with BSA_{ox} = 7.0 ± 1.0 nm and BSA_{sul} = 9.8 ± 1.5 nm. The pore radius reductions are not affected by the as produced pore radius but by the NAA material, most likely due to liquid-surface parameter adjustment during the slope to radius conversion. Nonetheless all BSA estimates are in good agreement with the literature.

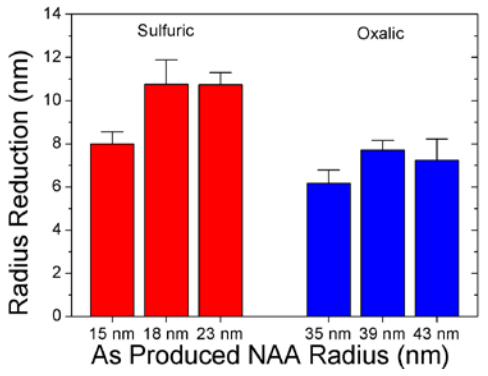

Figure 3: FICLI estimates of pore radius reductions as a function of widening time t_{PW} after BSA immobilization.

Figure 4 shows estimated pore radius and slopes of an NAA after a series of modification steps. The functionalization reduced the slopes by a factor of 3 which produced a radius reduction of APTES+GTA = 10.7 ± 0.7 nm. According to the reaction conditions, this represents a multi-layer of APTES and is in good agreement with the literature. The covalent immobilization of streptavidin resulted in a 3900 fold decrease in slope, producing a radius reduction of Streptavidin = 24.5 ± 0.2 nm. The radius reduction due to the covalent immobilization of streptavidin is reasonable, though over-estimated, most likely due to multilayer formation.

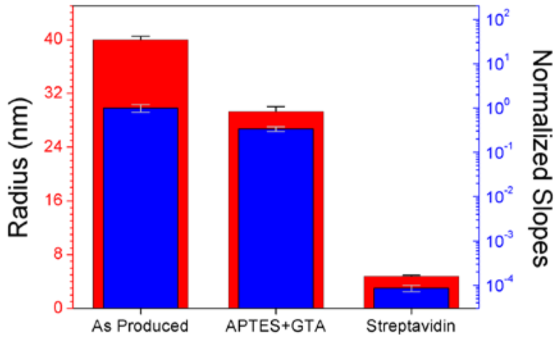

Figure 4: Pore radii estimated by FICLI before and after the immobilization of Protein A and antibody binding.

Conclusion

We presented FICLI as a more accurate NAA characterization technique compared to ESEM by showing more consistent pore etching rates. We successfully demonstrated that the FICLI detection and characterization of electrostatically immobilized BSA is independent of the initial pore radius and that it is applicable to different NAA materials as long as the correct liquid-surface interface parameters are used. All BSA radius reductions were in good agreement with the literature. We successfully characterized the multilayer formation of APTES+GTA and we were able to further detect the covalent immobilization of streptavidin. Considering the functionalization and immobilization conditions all radius reductions are reasonable estimates indicating multi-layers formation.

References

(1) Macias, G.; Ferré-Borrull, J.; Pallarès, J.; Marsal, L. F. Effect of Pore Diameter in Nanoporous Anodic Alumina Optical Biosensors. *Analyst* **2014**.

(2) Eckstein, C.; Xifré-Pérez, E.; Porta-I-Batalla, M.; Ferré-Borrull, J.; Marsal, L. F. Optical Monitoring of the Capillary Filling Dynamics Variation in Nanoporous Anodic Alumina toward Sensing Applications. *Langmuir* **2016**, *32* (41), 10467–10472.

(3) Urteaga, R.; Acquaroli, L. N.; Koropecki, R. R.; Santos, A.; Alba, M.; Pallarès, J.; Marsal, L. F.; Berli, C. L. A.; Marsal, F.; Berli, C. L. A. Optofluidic Characterization of Nanoporous Membranes. *Langmuir* **2013**, *29* (8), 2784–2789.

Design and fabrication of nano-structured Au-Si wafers for LDI-MS analysis

S. A. Iakab[1*], P. Ràfols[1], D. Vilalta[1,2], O. Yanes[1,2], R Calavia[1], L. Vojkuvka[3], X. Correig[1,2]

[1] Department of Electronic Engineering, Rovira i Virgili University, IISPV, Avinguda Països Catalans 26, 43007 Tarragona, Spain
[2] Spanish Biomedical Research Centre in Diabetes and Associated Metabolic Disorders (CIBERDEM), C/ Monforte de Lemos 3-5, 28029 Madrid, Spain
[3] Servei Recursos. Cientifics i Tecnics, Rovira i Virgili University, Tarragona, Spain
*Corresponding author: S. A. Iakab tel.: 977256570 email: stefania-alexandra.iakab@urv.cat

Abstract

Texturizing silicon wafers, a popular technique in the solar cell industry, can also be used in laser desorption/ionization mass spectrometry (LDI-MS) analysis. Nano- and micro-structured Si wafers have unique characteristics which allow their use in bioanalytical measurements such as laser desorption ionization mass spectrometry (LDI-MS). This work focuses on developing novel solid-state substrates consisting in textured silicon wafers recovered with a sputtered gold nanolayer (AuTSi) for LDI-MS analysis of liquid samples.

1. Introduction

The main disadvantage of the MALDI-MS spectroscopy is that standard organic matrix interferes the obtained spectrum with interfering peaks, especially in the low mass range spectrum (<1000 Da.). One of the most successful alternative is to replace the organic matrix, which facilitates the ionization and desorption processes during analysis, with solid-sate substrates. Nano- and micro-structured materials such as porous silicon surfaces, nanoparticles, nanostructured coatings, polymers, sol-gels and carbon-based materials have shown promising results (1). Semiconductor-based materials, for instance, nanostructured silicon, have a unique morphology that allows LDI-MS analysis at a lower laser energy and a faster response time (2). Likewise, gold nanoparticles have been reported to offer advantages in terms of high ionization efficiency by reducing required laser energy for desorption and ionization and increasing the detection sensitivity (3). Considering the advantages of the above-mentioned materials, designing a nanostructured silicon based substrate with Au nano-coating could be an innovative solid-state substrate that complies with the necessities of a LDI-MS sample support and also improves the conventional technique.

In this work we present the fabrication and application of gold-coated nano-textured silicon wafers (AuTSi) as promising LDI-MS sample substrates. The experimental workflow is described in section 2. Materials and Methods and the characterization of the substrates is detailed in section 3. Results. We report the successful use of the as described novel AuTSi substrates for LDI-MS analysis of liquid samples.

2. Materials and Methods

The texturing process of the silicon wafers was carried out in a reactive ion etching (RIE) reactor Oxford Instruments NPG80 ICP65. For all experiments, we used n-type (100) CZ-Si wafers of 4 inch diameter, 520 µm thickness. Different plasma treatments were used to obtain the desired morphology and the physical and chemical properties. Two samples have been obtained: bare texturized silicon (TSi) and Au covered texturized silicon (AuTSi). The texturizing plasma consisted of a mixture of O_2 and SF_6 of ratio 1:1 with pressure of 30 mTorr, RF power 100 W and etching time 15 min. In case of the AuTSi sample, a 4 nm layer of Au was deposited via sputtering (60W for 50s) over the texturized silicon. To obtain areas of different hydrophobicity, CHF_3 plasma treatment (50W, 20 mTorr, 14 min) was used with a negative mask. The area exposed to the plasma became super-hydrophobic while the areas “protected” by the mask kept their previous hydrophilic behavior.

The surface morphology was characterized by SEM. Reflectance measurements were carried out with a Lambda-950 spectrophotometer in a 200-800 nm spectral range. Optical Tensiometer Theta Lite 100 together with Oneattension software from Biolin Scientific Holding was used to determine the contact angle of the different types of surface regions. Finally, LDI-MS analysis was carried out using standard solutions: D-(+) glucose, folic acid, and 1,2-dioleoyl-sn-glycero-3-phosphocholine were dissolved in a solution of water:methanol (1:1 ratio) obtaining final standard solutions of 1% concentration (mg/ml). LDI-MS measurements were performed with a Voyager De STR MALDI-TOF spectrometer equipped with a N_2 laser (337 nm), operating with a frequency of 20 Hz and 3 ns pulses.

3. Results

The texturization process was inspired in the black silicon method described in detail by Gao et al. (2) The fabrication parameters for this work were adapted from (2) in order to obtain a needle-like structure of maximum roughness below 1µm. SEM images from Fig 1. show the needle-like morphology of the surface (a) and an average height of the needle structure around 900 nm (b). The density of the needles was determined as 61.8 needles/µm^2 with an average needle diameter of 80 nm.

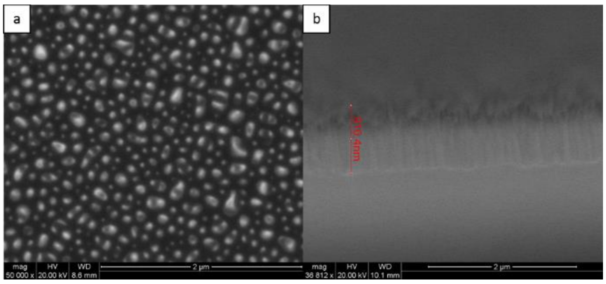

Fig.1. SEM images of TSi showing surface morphology (a) and cross-section view of the surface (b).

The obtained needle-like morphology has specific characteristics such as high anti-reflectivity (Fig. 2) and good hydrophilic behavior.

Reflectance measurements show that both samples have changed their reflectance from 50-60% to less than 2% at 337 nm light, which is the wavelength of the N_2 laser thanks to the needle-like morphology of the surface. Moreover, it has been observed that the Au covered sample reflects slightly less light as seen in Fig. 2. This indicates that light is absorbed better in the presence of Au nano-structures and it is further converted into energy necessary for the desorption and ionization processes of the analyte.

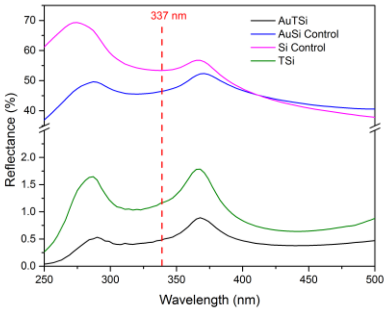

Fig.2. Reflectance measurements of all samples and their respective control sample.

Contact angle measurements have confirmed the expected effect of the plasma treatments. The needle-like structure obtained by the black silicon method provides preferable hydrophilic surface with mean contact angle (CA) of 44° for TSi and 75° for AuTSi, while the CHF_3 plasma treatment changed the nature of the surface from hydrophilic to super hydrophobic (CA>120°) in both cases (167° and 154°, respectively). This method of fabricating regions of selective surface properties improves the analyte deposition operation, because allows to spread and confine the aqueous analyte in the hydrophilic area and gives more robustness to the measurement. The high surface area and hydrophilic nature of the substrates also facilitate the crystallization of liquid samples.

Laser/desorption ionization measurements of the prepared standard solutions have provided favorable results. Low mass compounds have been successfully identified, as demonstrated by the sodium adduct of glucose (M+Na 203.0531) from Fig.3. below.

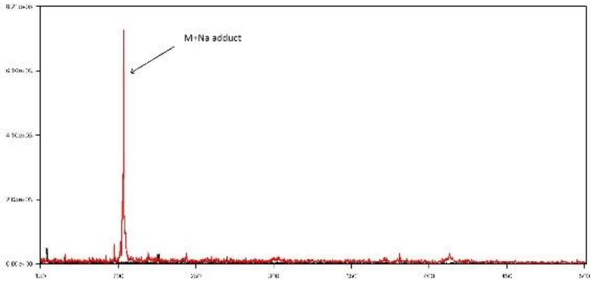

Fig.3. LDI-MS analysis of glucose. The high intensity peak represents the Na adduct of glucose.

The morphology of the surface along with the Au nano-layer provided ideal environment for a more effortless ionization process of the analyte. This process resulted in a "clean" raw spectra that affirms the good functionality of the novel sample substrate for LDI-MS analysis.

7. Conclusions

In this work we have successfully designed, fabricated and tested a novel solid-state substrate that facilitates LDI-MS analysis for liquids. All results support the appropriate use of the texturized gold-coated silicon wafers as sample support and as well as promoter of desorption and ionization processes in LDI-MS analysis.

Acknowledgements

The authors want to acknowledge the financial support of the Spanish Ministry of Economy and Competitivity through project TEC2015-69076-P and SAI´s pre-doctoral grant No. BES-2016-076483. SAI also acknowledges all the help of José Ferré Borrull and M. Carme Crespo Blázquez

References

[1] Y. E. Silina, D. A. Volmer, "Nanostructured solid substrates for efficient laser desorption/ionization mass spectrometry (LDI-MS) of low molecular weight compounds", *Analyst*, 2013, 138, 7053.

[2] J. Gao, M. de Raad, N. P. Bowen, R. N. Zuckermann, T.R. Northen, "The Application of Black Silicon for Nanostructure-Initiator Mass Spectrometry", *Anal. Chem*, 2016.

[3] M. Dufresne, J.F. Masson, P. Chaurand, "Sodium-Doped Gold-Assisted Laser Desorption Ionization for Enhanced Imaging Mass Spectrometry of Triaylglycerols from Thin Tissue Sections", *Anal Chem*, 2016. 88, 6018-6025.

Inverted Polymer Solar Cells using Pd-doped TiOx as Cathode Buffer Layer

J. G. Sánchez[1], V. S. Balderrama[2], M. Estrada[2], J. Ferré-Borrull[1], J. Pallarès[1**] and L.F. Marsal[1*]

[1]Departament d'Enginyeria Electrònica Elèctrica i Automàtica Universitat Rovira i Virgili
Av. Països Catalans 26, 43007 Tarragona, Spain
[2]Centro de Investigación y de Estudios Avanzados del Instituto Politécnico Nacional (CINVESTAV-I.P.N)
Av. Instituto Politécnico Nacional 2508, 07360 Ciudad de México, México
Corresponding authors email: **josep.pallares@urv.cat and * lluis.marsal@urv.cat

Abstract

We studied the effects of Pd-doped TiOx layer on the performance of inverted polymer solar cells based on thieno[3,4-b]-thiophene/benzodithiophene (PTB7) and [6,6]-phenyl-C71-butyric acid methyl ester ($PC_{70}BM$). The polymer solar cells with inverted structure were fabricated using titanium suboxide with several Pd concentrations as cathode buffer layer. Some devices were fabricated using pristine TiOx as cathode buffer layer as control samples. The solar cells fabricated with lowest Pd-doping concentration show a significantly improvement of the devices performance. On the other hand, high Pd concentrations are detrimental to devices performance.

1. Introduction

The polymer solar cells (PCSs) have attracted much attention in recent years due to of their lightness, flexibility, low-cost and large scale fabrication. In conventional PSCs (c-PSCs) the poly-(3,4-ethylene dioxythiophene):poly-(styrenesulfonate) (PEDOT:PSS) and calcium (Ca) are commonly used as anode buffer layer (ABL) and cathode buffer layer (CBL), respectively.[1] It is well known that the highly oxidation of Ca under air environment and the hygroscopic nature of PEDOT:PSS can degrade the active layer and the indium tin oxide (ITO), resulting in a low stability and lifetime of c-PSCs.[2] In order to improve the performance, life-time and long-term stability, PSCs with an inverted structure (i-PSCs) have been developed.[3]. In i-OSCs, transition metal oxides (e.g. molybdenum oxide (MoO_3) and vanadium oxide (V_2O_5)), are used as ABL due to their high work-functions (>5 eV) allows to obtain low resistance ohmic contacts.[4] On the other hand, titanium suboxide (TiOx) and zinc oxide (ZnO) are commonly used as CBL.[3, 5] TiOx has been widely used in i-PSCs as electron-collecting layer because presents good transparency as thin films, high stability and high electron mobility. In addition, TiOx can act as an optical spacer and redistribute the light intensity into the active layer.[6] Recently, it has been reported that doping the TiOx with some metal ions is a well strategy to tune the Fermi level position and modify the structural, electrical and magnetic properties.[7]

In this work, we present the synthesis of TiOx thin film doped with Palladium (Pd-doped TiOx) via sol-gel methods using several Pd concentrations. In order to study the effects of Pd-doped TiOx on the i-PSCs performance, some devices based on the blend of thieno[3,4-b]-thiophene/benzo-dithiophene (PTB7) and [6,6]-phenyl-C71-butyric acid methyl ester ($PC_{70}BM$) were fabricated using Pd-doped TiOx as CBL. In addition, i-PSCs with pristine TiOx were fabricated as control samples.

2. Experimental and Results

Pristine and Pd-doped TiOx precursor solutions were synthetized via sol–gel methods by mixing titanium (IV) isopropoxide, 2-methoxyethanol and ethanolamine. Pd-doped TiOx solutions were prepared by adding Palladium (II) acetylacetonate to the pristine TiOx solution. All solutions were stirred and heated at 120 °C under inert atmosphere. Subsequently, the solution were diluted in anhydrous methanol with a volume ratio 1:6 and stirred at room temperature for 1 hour. The blend solution was prepared dissolving PTB7 and $PC_{70}BM$ (weight ratio of 1:1.5) in a solvents mix of chlorobenzene (CB) and 1, 8-diiodooctane (DIO) (97:3 v/v) with a final solution concentration of 25 mg mL^{-1}. The solution was left stirring and heating under inert atmosphere at 40 ºC overnight. The i-PSCs were fabricated on ITO-coated glass. The pristine TiOx and Pd-doped TiOx precursor solutions were spin-cast on ITO substrates at 6000 rpm. Afterwards, the samples were left in ambient conditions for 1 hour to convert the precursor in TiOx by hydrolysis. Then, samples were annealed at 400 °C. Subsequently, blend solution of PTB7:$PC_{70}BM$ was spin-cast on top of pristine and Pd-doped TiOx layers at 800 rpm for 30 s. Finally, 5 nm of V_2O_5 and 100 nm of Ag were thermally evaporated onto the photoactive layer in a vacuum chamber. The active area for all devices was 9 mm^2.

Figure 1 shows the inverted structure of the BHJ polymer solar cells fabricated. The sample names and the Pd concentration used to dope the TiOx are shown in Table 1. Figure 2 shows the normalized open circuit voltage (V_{OC}), short circuit current density (J_{SC}), fill factor (FF) and power conversion efficiency (PCE) of i-PSCs using Pd-doped TiOx as CBL with several Pd concentrations. The sample Pd0 and Pd3 exhibited the highest V_{OC}, while the V_{OC} decreases as the Pd concentration increases in samples Pd6, Pd12 and Pd24. The sample using pristine TiOx (Pd0) presents the highest J_{SC}. On the other hand, J_{SC} decreases as the Pd concentration increases. Note that sample Pd24 exhibited a similar J_{SC} than sample Pd3. In sample Pd3, the FF increased by ~4% in comparison to sample Pd0, while that FF slightly decreased as the Pd concentration increased in samples Pd6, Pd12 and Pd24. In comparison to samples with pristine TiOx (Pd0), the PCE was slightly increased in samples with the lowest Pd concentration (Pd3). Nevertheless, the PCE decreased using higher Pd concentrations (samples Pd6, Pd12 and Pd24).

3. Conclusions

We showed that TiOx doped with Pd affects the performance parameters of i-PSCs. The results exhibited that using lower Pd concentration of 3mg the efficiency of solar cells was slightly improved. However, the performance parameters of i-PSCs were reduced in samples with the Pd concentration higher than 3mg. Finally, we demonstrated that using TiOx doped with Pd as cathode buffer layer is a promising approach to improve the performance of i-PSCs.

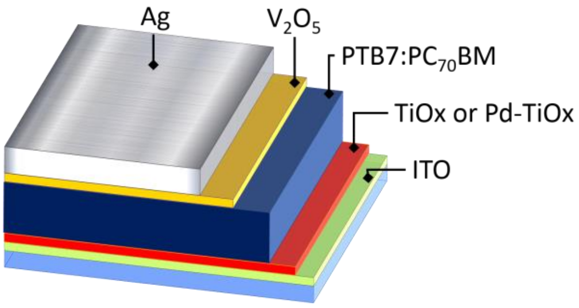

Figure. 1 Inverted structure.

Sample	Pd concentration [mg]
Pd0	0 (pristine)
Pd3	3
Pd6	6
Pd12	12
Pd24	24

Table 1. Pd concentrations of Pd-doped TiOx used as cathode buffer layer.

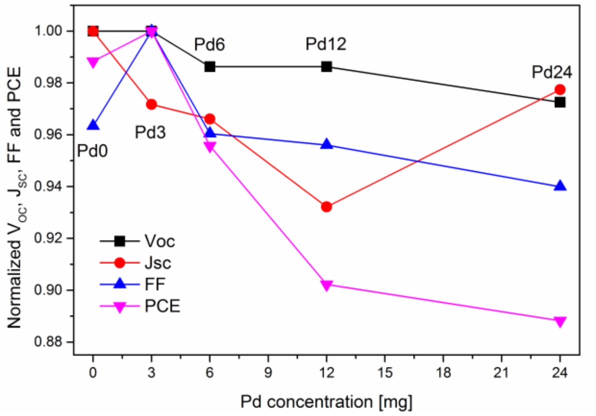

Figure 2. Normalized performance parameters: V_{OC} (black square), J_{SC} (red circle), FF (blue triangle) and PCE (pink triangle) of i-PSCs using Pd-doped TiOx as CBL with several Pd concentrations.

Acknowledgements

This work was supported in part by the Spanish Ministry of Economy, Industry and Competitiveness (MEIC) under grant numbers TEC2015-71324-R and TEC2015-71915-REDT, the ICREA under the ICREA Academia Award, the Catalan authority under project AGAUR 2014 SGR 1344 and the CONACYT Project 237213 in Mexico.

References

[1] V. S. Balderrama, F. Avila-Herrera, J. G. Sanchez, J. Pallares, O. Vigil-Galan, L. F. Marsal, and M. Estrada, “Organic Solar Cells Toward the Fabrication Under Air Environment,” *IEEE J. Photovoltaics*, vol. 6, no. 2, pp. 491–497, Mar. 2016.

[2] V. S. Balderrama, M. Estrada, P. L. Han, P. Granero, J. Pallarés, J. Ferré-Borrull, and L. F. Marsal, “Degradation of electrical properties of PTB1:PCBM solar cells under different environments,” Sol. Energy Mater. Sol. Cells, vol. 125, pp. 155–163, 2014.

[3] J. G. Sánchez, V. S. Balderrama, M. Estrada, E. Osorio, J. Ferré-Borrull, L. F. Marsal, and J. Pallarès, “Stability study of high efficiency polymer solar cells using TiOx as electron transport layer,” Sol. Energy, vol. 150, pp. 147–155, 2017.

[4] J. Meyer, S. Hamwi, M. Kröger, W. Kowalsky, T. Riedl, and A. Kahn, “Transition metal oxides for organic electronics: Energetics, device physics and applications,” *Adv. Mater.*, vol. 24, no. 40, pp. 5408–5427, 2012.

[5] M. Thambidurai, J. Y. Kim, J. Song, Y. Ko, H. Song, C. Kang, N. Muthukumarasamy, D. Velauthapillai, and C. Lee, “High performance inverted organic solar cells with solution processed Ga-doped ZnO as an interfacial electron transport layer,” *J. Mater. Chem. C*, vol. 1, no. 48, p. 8161, 2013.

[6] J. Li, S. Kim, S. Edington, J. Nedy, S. Cho, K. Lee, A. J. Heeger, M. C. Gupta, and J. T. Yates, “A study of stabilization of P3HT/PCBM organic solar cells by photochemical active TiOx layer,” *Sol. Energy Mater. Sol. Cells*, vol. 95, no. 4, pp. 1123–1130, 2011.

[7] B. Roose, S. Pathak, and U. Steiner, “Doping of TiO 2 for sensitized solar cells,” *Chem. Soc. Rev.*, vol. 44, no. 22, pp. 8326–8349, 2015.

Multi-Scale Simulation Approach Combining NEGF-Based Current Calculation With Classical Compact Models Applied to Source/Drain Tunneling in Ultrashort MOSFETs and TFETs

F. Hosenfeld[1,2,✠], F. Horst[1,2], F. Lime[2], B. Iñíguez[2], A. Kloes[1]
[1]NanoP, TH Mittelhessen University of Applied Sciences, Giessen, Germany
[2]DEEEA, Universitat Rovira i Virgili, Tarragona, Spain
[✠]Fabian.Hosenfeld@ei.thm.de

***Index Terms*—Analytical Potential Model, Non Equilibrium Green's Function (NEGF), Multi-Scale Simulation, Compact Model, Current Model, Double-Gate (DG) FET, Tunnel FET, non-iterative**

I. INTRODUCTION

Modeling future devices using classical transport theory will not be sufficient because emerging quantum mechanical effects dramatically change the device behavior. In contrast to classical physics, quantum physics allows electrons to tunnel through the forbidden zone. This effect is well known as Source-to-Drain (SD) tunneling in ultrashort MOSFETs as well as band-to-band (B2B) tunneling in TFETs.

Based on Schrödinger's wave equation, the Non Equilibrium Green's Function (NEGF) formalism has been established to consider quantum physics in TCAD simulations of ultra-scaled devices [1]. The iterative coupling between Poisson solver and NEGF heavily increases the simulation time and consequently forbids its usage for circuit simulations. In order to perform circuit simulations with few to thousands of transistors, numerical efficient compact models are necessary. The only drawback to these models are the physical simplifications which do not consider accurately quantum effects. Multi-scale simulation bridges the gap between compact models and device simulation. The introduced model gives a fundamental approach to consider quantum effects in a compact way. In the case of a MOSFET, the NEGF replaces the compact form solution of the classical transport equation. In the case of a TFET the NEGF replaces the Wentzel-Kramers-Brillouin (WKB) approximation (Fig. 1). Whether the combination of a classically calculated potential and a NEGF based current calculation is sufficient, must be validated by comparing with self-consistent numerical device simulations. For this purpose, the paper provides positive results.

II. ANALYTIC MODEL DERIVATION

In order to transfer these physics into a compact transistor model, the iterative coupling of the Poisson solver with the transport solver is omitted. Therefore, the conduction band is calculated accurately, using a proved potential solution presented in [2]. The electron density and the current are calculated by a 1D NEGF formalism derived from [1]. Merging both parts lead to a non-iterative model which considers quantum based current transport in DG transistors. In a last step, mathematical approximations for gaining the numerical efficiency are applied. Based on the potential solution, the 1D conduction band and valence band $U(x)$ are calculated, which are used as input parameter for the NEGF.

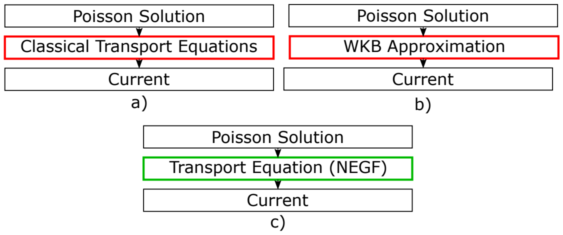

Figure 1. Flowchart of a) common compact MOSFET models b) common compact TFET models c) the introduced compact NEGF based model.

The NEGF formalism applies an effective mass Hamiltonian $H = -(\hbar^2/2m)\nabla^2$ to describe electrons in an parabolic conduction band. The longitudinal part of the Hamiltonian is given by:

$$H_L = E_c - \frac{\hbar}{2m} \cdot \frac{d^2}{dx^2} + U(x). \tag{1}$$

The finite difference method is used to represent the 1D wave equation as the Hamiltonian matrix H_L. Open boundary conditions are considered by the connection of the device to the semi-infinite contacts, which are described by the self-energy functions $\Sigma_{1,2}$. The retarded Green's function $[G]$ represents the device's system response to an input stimulus:

$$G(E) = \left[EI - H_L - \Sigma_1 - \Sigma_2\right]^{-1}, \tag{2}$$

where E is the considered energy and I is the identity matrix. Together with the Fermi function of each contact, the retarded Green's function leads to the electron density and hence to the current density of one energy E. In order to gain numerical efficiency, the current density is calculated only at certain energies and positions. The subsequent interpolation leads to the drain current.

III. MODEL VERIFICATION

A simulation of a DG MOSFET (Fig. 2a) has been performed using numerical NanoMOS TCAD [3] by applying the following device parameters: $l_{sd} = 10\,\mathrm{nm}$, $t_{ox} = 1\,\mathrm{nm}$, $t_{ch} = 2\,\mathrm{nm}$, $N_{sd} = 2 \cdot 10^{20}\,\mathrm{cm}^{-3}$, $\epsilon_{ox} = 25 \cdot \epsilon_0$ and an applied bias of $V_{ds} = 0.05\mathrm{V}$. The simulation obtains an good shape of the conduction band (Fig. 3), as well as an accurate current characteristic (Fig. 4).

Performing a DG TFET (Fig. 2b) simulation applying the parameters: $l_{sd} = 20\,\mathrm{nm}$, $l_{ch} = 22\,\mathrm{nm}$, $t_{ch} = 10\,\mathrm{nm}$, $t_{ox} = 2\,\mathrm{nm}$, $N_{sd} = 2 \cdot 10^{20}\,\mathrm{cm}^{-3}$, $\epsilon_{ox} = 25 \cdot \epsilon_0$, shows an good shape of the conduction and valence band (Fig. 5), as well as an accurate current characteristic (Fig. 6). The potential profile as well as the drain current are validated with numerical Sentaurus TCAD [4] data by using the nonlocal tunneling model. In consequence of neglecting the electron scattering in the TFET model in contrast to TCAD simulation, the current is overestimated for high gate bias.

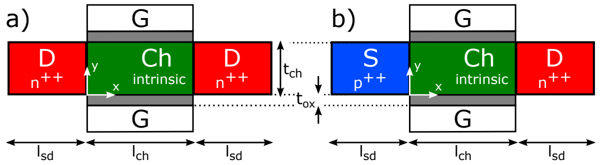

Figure 2. Geometry of the considered device a) DG MOSFET b) DG TFET.

IV. CONCLUSION

Introduced is a non-iterative NEGF approach to consider quantum- and thermionic emission current transport in a physical way, which is suitable for implementation in compact models. In the modeling approach for DG MOSFET as well as for DG TFET, a 2D analytical closed-form potential model [2] is coupled with NEGF formalism [1] in a numerically efficient way. The results validate the presented approach, which shows a way to bridge the gap with regard to multi-scale simulation between a NEGF based current calculation, including fundamental quantum mechanics and an efficient compact model which allows the simulation of complex circuits.

ACKNOWLEDGMENTS

This work was supported by the German Federal Ministry of Education and Research under contract No.03FH001I3 and the Spanish Ministry of Economy and Competitiveness through project GREENSENSE (TEC2015-67883- R). We would like to thank Keysight Technologies for the license donation of the software IC-CAP and AdMOS GmbH for support.

REFERENCES

[1] S. Datta, "Nanoscale Device Modeling: the Green's Function Method." *Superlattices and Microstructures*, vol. 28, no. 4, pp. 253 – 278, 2000.
[2] M. Graef, T. Holtij, F. Hain, A. Kloes, and B. Iniguez, "Improved Analytical Potential Modeling in Double-Gate Tunnel-FETs." in *Mixed Design of Integrated Circuits Systems (MIXDES), 2014 Proceedings of the 21st International Conference*, pp. 49–53, June 2014.
[3] Z. Ren, S. Goasguen, A. Matsudaira, S. S. Ahmed, K. Cantley, Y. Liu, Y. Gao, X. Wang, and M. Lundstrom, "NanoMOS." https://nanohub.org/resources/1305, Mar 2016.
[4] Synopsys, Inc., *Sentaurus Device User Guide*, g-2012.06 ed., 2012.

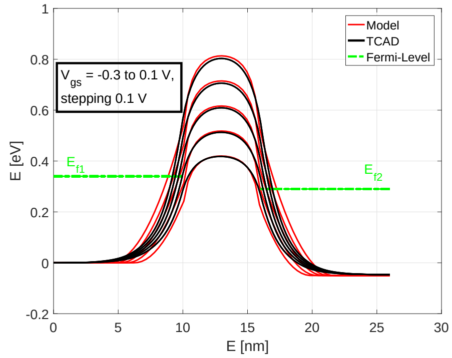

Figure 3. Conduction band calculated by the DG MOSFET model and NanoMOS TCAD for a channel length $l_{ch} = 6\,\mathrm{nm}$.

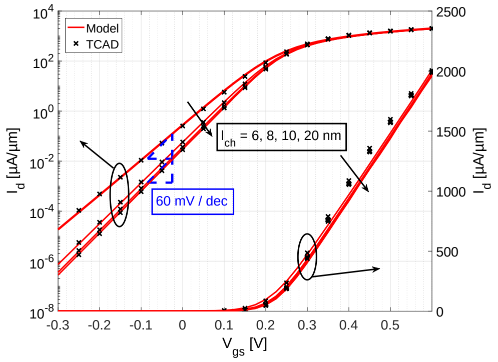

Figure 4. Transfer characteristics of the DG MOSFET in log-scale on the left y-axis and in linear scale on the right, compared with NanoMOS TCAD data.

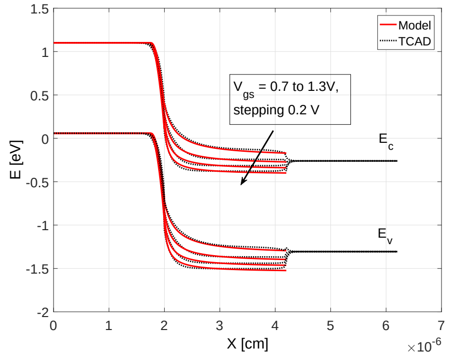

Figure 5. Comparison between the Sentaurus TCAD data of the energy bands and the model for a DG TFET with an applied bias of $V_{ds} = 0.2\mathrm{V}$.

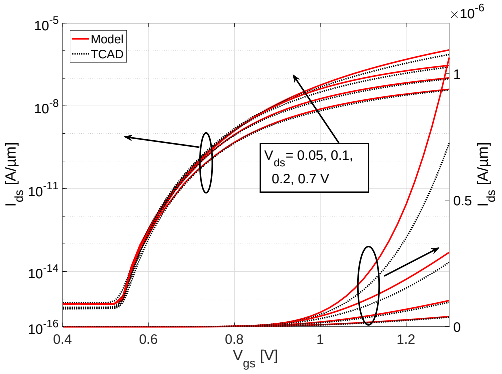

Figure 6. Resulting transfer characteristics of the TFET in log-scale on the left y-axis and in linear scale on the right, compared with TCAD Sentaurus data.

Tuning Optical Properties of Rugate Structures based on Nanoporous Anodic Alumina

L. Karen Acosta, Elisabet Xifré-Perez, Josep Ferré-Borrull, and Lluis F. Marsal*

Departament d'Enginyeria Electrònica, Elèctrica i Automàtica, Universitat Rovira i Virgili, Avinguda Països Catalans 26, 43007 Tarragona, Spain; Phone: 977 55 85 24
***Email: lluis.marsal@urv.cat**

Abstract

In this work, we design and fabricate Rugate Structures based on Nanoporous Anodic Alumina in the UV and VIS, a spectral range especially interesting for photonic applications like sensing and data coding. We make a systematic study of the influence of each design parameter on the optical properties of NAA-RS, emphasizing the influence of the design parameters on the quality factor and position of the photonic stop band.

1. Introduction

Rugate structures (RS) are one-dimensional photonic crystals with a continuous and periodic variation of its refractive index with depth. They can be obtained on the based on nanoporous anodic alumina (NAA), by the electrochemical anodization of high-purity aluminum foils by means of a sinusoidal anodization current [1]. The sinusoidal modulation of the refractive index results in an interesting optical behavior consisting of a well-defined photonic stop band. Furthermore, several sinusoidal profiles can be overlapped in order to produce films with several forbidden phonic bands [2, 3].The optical properties of NAA-RS can be engineered by adjusting several design parameters such as the average anodization current, the current amplitude, the period and the number of periods of the sinusoidal current component. This way, high quality and selective photonic bands located in the ultraviolet (UV), visible and near infrared (NIR) range can be precisely defined.

2. Materials and Methods

Materials

High purity Aluminium foils (thickness 0.5 mm and purity 99.99%), Ethanol (C2H5OH), perchloric acid (HClO4), oxalic acid (H2C2O4) , hydrochloric acid (HCl), copper chloride (CuCl) were purchased from Sigma-Aldrich. Double deionized water (DI) (18.6 MΩ) was used for all the solutions unless other specified.

Fabrication

First Al substrates were degreased in acetone, cleaned with ethanol and DI water and finally dried under steam of air. Before the anodization, Al substrates were electropolished in a mixture of Ethanol and Perchloric acid 4:1 at 20 V and 5ºC for 5 min. During the electropolishing step the stirring direction was alternated every 60 s. After the electropolishing the samples were cleaned with ethanol and DI water and dried under steam of air [4]. Then, the anodization was carried out in $H_2C_2O_4$ 0.3 M at 5ºC applying a sinusoidal current profile with several design parameters like offset current (I_0), amplitude current (I_1), Period (T) and number of periods (N) (equation 1). Figure 1 shows the sinusoidal current profile and involved parameters during the fabrication.

$$I(t) = Io + I_1 \sin\left(\frac{2\pi}{T}t + \varphi\right) \tag{1}$$

Where I(t) is the current at time t, I1 is the amplitude current, T is the period and I0 is the offset current.

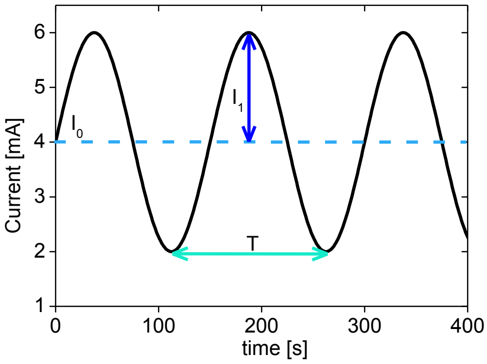

Figure 1. Current profile of Rugate structures based on nanoporous and alumina and involved fabrication parameters.

3. Results

Figure 2 shows the reflectance spectra of the samples. S1 (T=100s), S3 (T= 150s) and S4 (T=200s) can be compared as they have different period lengths. We can observe that the longer the anodization period the longer the wavelength of the R peak (shift to the red). We can observe the effect of the offset current (I_0) samples (S3 with I_0=4 mA and S5 with I_0=3 mA), when I_0 is higher the wavelength of R peak increases. We analyzed the influence of the number of periods (samples S2 with N=100 and S3 with N=200) a slightly shift to the left (UV range) is observed also we can observe there is a slightly increment in the reflection due to the increment of number of periods. Finally, figure 3 shows the effect of the amplitude current (I_1).We can observe that in the sample S3 (I_1= 2mA) is higher than the sample S6 (I_1= 1mA) due to the decrement of amplitude current. Note that the position of the maximum is in the same wavelength (580 nm).

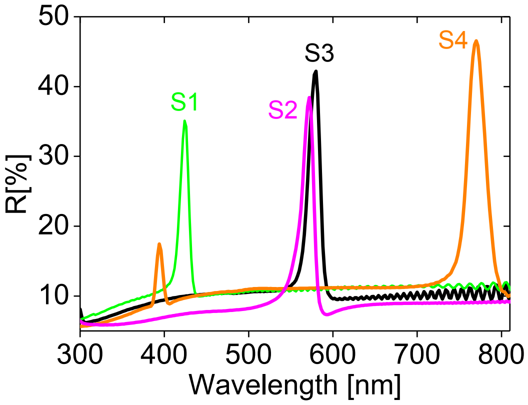

Figure 2. Reflectance spectra of Nanoporous Anodic Alumina Rugate Structures samples with different fabrication parameters (T, I_0 and N)

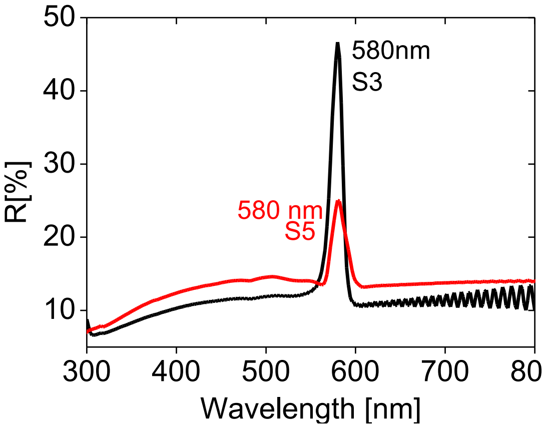

Figure 3. Reflectance spectra of Nanoporous Anodic alumina Rugate Structures of the samples wit different amplitude current I_1.

4. Conclusions

Rugate Structures were fabricated applying a sinusoidal current profile with different fabrication parameters in order to study their influence in the wavelength peak. Each parameter has a different influence on the resultant reflectance spectra. The offset current and the period tune the wavelength position of the peak , the amplitude current contributes to the height and width of the peak and finally the number of periods induces a slightly shift that could be ascribed to a small porosity gradient in depth. The fabrication parameters (N, T, I_0 and I_1) not only determine the position of the wavelength peak but also contribute to their height and width.

Acknowledgements

This work was supported in part by the Spanish Ministry of Economy, Industry and Competitiveness (MEIC) under grant numbers TEC2015-71324-R and TEC2015-71915-REDT, the ICREA under the ICREA Academia Award and the Catalan authority under project AGAUR 2014 SGR 1344.

References

[1] J. Ferre-Borrull, E. Xifre-Perez, J. Pallares, L.F. Marsal. Optical properties of nanoporous anodic alumina and derived applications. In: D. Losic, A. Santos editors. Nanoporous Alumina. Fabrication, Structure, Properties and Applications, Springer Series in Materials Science Vol. 219 (2015) p. 185-217.

[2] G. Macias, L.P. Hernández-Eguía, J. Ferré-Borrull, J. Pallares, L.F. Marsal, ACS Appl. Mater. Interfaces, **5** (2013) 8093.

[3] G. Macias, J. Ferré-Borrull, J. Pallares, L.F. Marsal, Nanoscale research letters, 9 (2014) p. 315

[4] A. Santos, J.H. Yoo, C. Vashisth, T. Kumeria, Y. Wang, D. Losic, Nanoscale, 8 (2016) 1360.

Studying charge transfer reactions in novel solar cells using advanced time-resolved spectroscopy.

Ilario Gelmetti, Nuria F. Montcada, Emilio J. Palomares Gil

igelmetti@iciq.es, epalomares@iciq.es
Institute of Chemical Research of Catalonia (ICIQ), Avda. Països Catalans 16, E-43007 Tarragona, Spain

Abstract

Hybrid lead halide perovskite semiconducting material is a good candidate for being used as absorber in cheap and efficient solar cells. In Prof. Emilio Palomares group we fabricate various compositions and dimensionalities (from bulk to quantum dots) of this material in order to characterize it and the complete devices using optical and electrical nanosecond resolved techniques. This allows us to have an insight on the fundamental physics involved and in turn helps in identifying and targeting energy loss pathways.

1. State of the Doctorate

In my third year of PhD I will apply my knowledge of photophysical characterization techniques and perovskite solar cells fabrication (up to 18 % power conversion efficiency) for various kind of studies. Additionally a collaboration with Prof. Di Fonzo (IIT, Italy) is starting for joining a water-splitting device with a perovskite solar cell in a single complex device. In the fourth quarter of 2017 I will go for a 3 months stay in the group of Prof. Jenny Nelson (ICL, London) with focus on computational modelling of charges and ion kinetics in the perovskite material.

2. Studies on Charge Accumulation

We have fabricated methylammonium lead iodide (MAPI) perovskite solar cells using as selective contacts PEDOT:PSS polymers blend for holes and PCBM-C_{70} fullerene derivative for electrons. The thickness of MAPI, PCBM-C_{70}, and PEDOT:PSS layers has been varied in order to evaluate the contribution of each layer to the final device performance. We have measured the devices capacitance under illumination and the charge carrier's lifetime using photo-induced time resolved techniques [1]. The results show that in this kind of devices the limiting layer is the PCBM-C_{70} due to its relative reduced mobility compared to PEDOT:PSS that makes the control of the fullerene thickness crucial for device optimization. Moreover, capacitive measurements (see Fig.1) show differences for the devices having different PCBM-C_{70} layer thicknesses in contrast with the measurements on the different PEDOT:PSS thickness. These give indications about holes and electrons storage and their distribution.

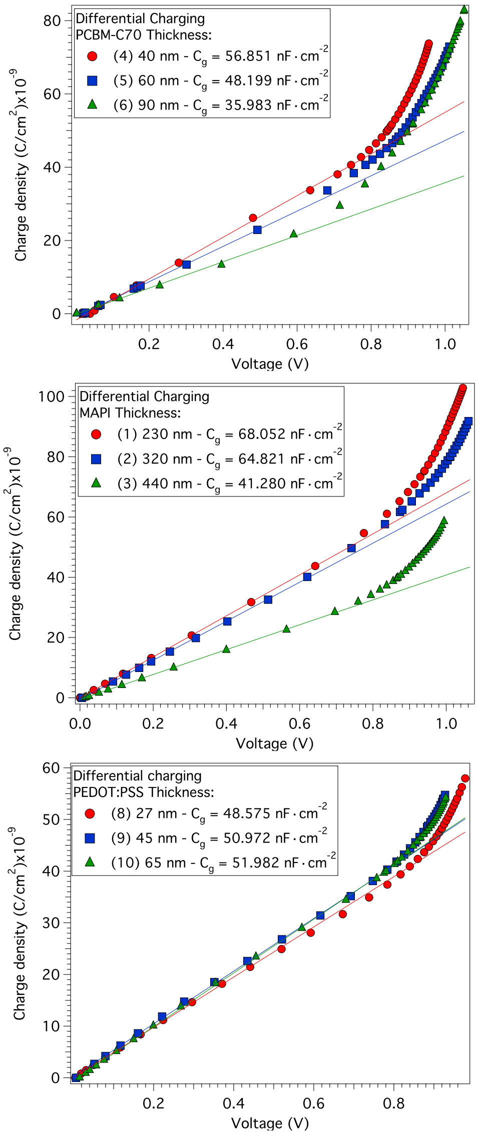

Fig.1. Differential charging characterization for top cathode perovskite solar cells with different layers thicknesses.

3. Application of Photophysical Characterization in Hole Transporting Materials Comparison

We studied the variations of open circuit voltage (V_{OC}) in mixed cation [2] (cesium, methylammonium, formamidinium) lead iodide bromide (CsFAMAPIBr) perovskite solar cells with bottom cathode planar architecture (FTO/compact-TiO2/CsFAMAPIBr/HTM/Au) when using two different hole transporting materials (HTM): the reference spiro-OMeTAD and the new 1,1,2,2-tetrakis{4-[bis(4-methoxyphenyl)amino]phenyl} ethene (TAE-1). TAE-1 is a promising HTM because of its easy and cheap synthesis [3], giving performances similar to the reference material.

We observed lower V_{OC} in current-voltage swaps (see Fig.2) for devices with TAE-1 and this can't be explained neither considering energetic levels of the HTMs in solution (HOMO measured via cyclic voltammetry, HOMO-LUMO band gap measured via absorbance and photoluminescence, see Fig.3), nor charge recombination kinetics as studied via photo-induced transient photo voltage (PI-TPV, see Fig.4). We hypothesize that HOMO-LUMO levels for TAE-1 deposited onto a MAPI layer varies greatly from the ones in solution. This could happen because of iodine ions migration into the organic layer or other chemical reactivities between the two layers.

Deeper investigation of the material layered on perovskite by means of Kelvin probe force microscopy and ultraviolet photoelectron spectroscopy is ongoing.

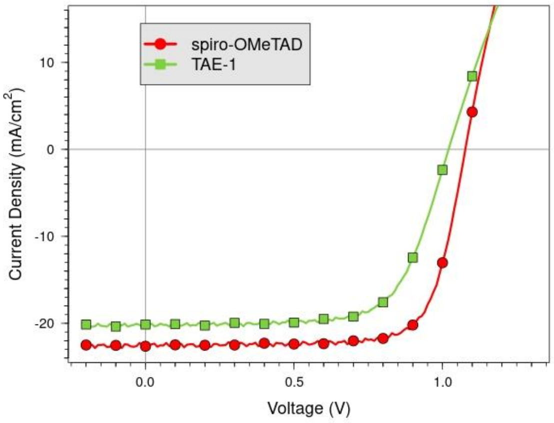

Fig.2. Current-voltage sweep for perovskite solar cells with two different HTMs.

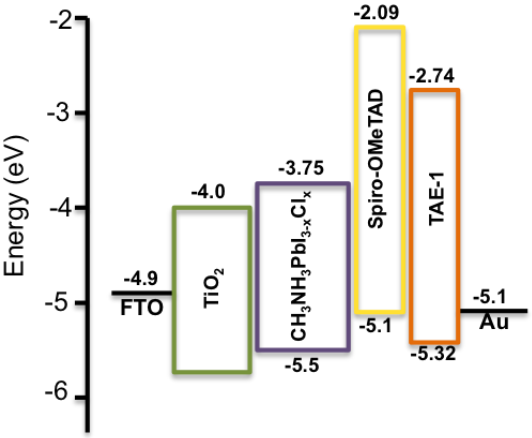

Fig.3. Energetic levels for the materials used in the bottom cathode perovskite solar cells.

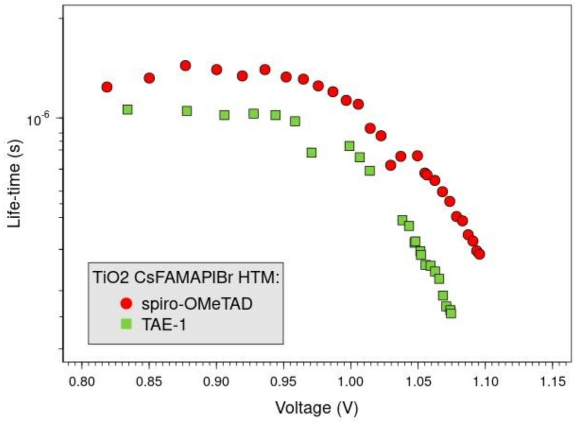

Fig.4. PI-TPV for perovskite solar cells with two different HTMs.

References

[1] Ryan, J. W., & Palomares, E. (2017). "Photo-Induced Charge Carrier Recombination Kinetics in Small Molecule Organic Solar Cells and the Influence of Film Nanomorphology." https://doi.org/10.1002/aenm.201601509

[2] Saliba, M., Matsui, T. et al., (2016). "Cesium-containing triple cation perovskite solar cells: improved stability, reproducibility and high efficiency." Energy Environ. Sci., 9 (6), 1989–1997. https://doi.org/10.1039/C5EE03874J

[3] Cabau, L., Garcia-Benito, I., Molina-Ontoria, A., Montcada, N. F., Martin, N., Vidal-Ferran, A., & Palomares, E. (2015). "Diarylamino-substituted tetraarylethene (TAE) as an efficient and robust hole transport material for 11% methyl ammonium lead iodide perovskite solar cells." Chem. Commun., 51(73), 13980–13982. https://doi.org/10.1039/C5CC05236J

WO_3 nanowires doped with cobalt oxide nanoparticles for gas sensing applications

E. Navarrete[1], E. Llobet[1]

[1]MINOS-EMaS, Universitat Rovira i Virgili, Tarragona, Spain; eduard.llobet@urv.cat
*Correspondence: eric.navarrete@urv.cat; Tel.: +34-682-511-711

Abstract

A two-step procedure was implemented to obtain tungsten oxide nanowires (WO_3) doped with cobalt oxide nanoparticles from metal-organic precursors, $W(CO)_6$, $Co(acac)_2$. In the first step, nanowires were grown at 400ºC using an aerosol assisted chemical vapor deposition system (AA-CVD) and subsequently annealed at 500ºC for 2 hours. In the second step, metal loading (at different doping levels) of the nanowires using the same system. These hybrid nanomaterials were grown on top of commercial alumina substrates that comprised interdigitated electrodes. The response of these nanomaterials toward H2S and H2 is investigated and discussed.

1. Introduction

Due to the worldwide rise of environmental harmful emitted gases such as car's exhausting gases, industrial byproducts and daily emissions there is a growing concern towards the air quality and the detection of possible health threatens, therefore huge efforts have been put in develop new materials and sensing systems with the aim of detecting and monitoring such gases. The aim of this work is to produce an operative sensor using a nanostructured metal oxide layer with semiconductor properties, modified to be selective towards a specific gas.

2. Materials, methods and synthesis

Available commercial alumina sensors with an interdigitated platinum paste circuit on top and an integrated platinum paste heater on the bottom layer are used as a substrates. The sensor active layer is composted of a randomly-oriented layer of WO_3 nanowires grown on top of the interdigitated electrodes as contact bridge and subsequently doped with CoO_x nanoparticles.

Through an aerosol assisted- chemical vapor deposition method, hereon AACVD, the layer of nanowires is synthetized**[1]**. To obtain such structures 50 mg of $W(CO)_6$ are dissolved in 15 ml acetone and 5 ml methanol. Using a high frequency wave's generator the solution is brought to a spray state which is driven by a N2 current, 15 ml/min, flow towards a hot wall CVD reactor where the substrates had been placed previously. The temperature set for the nanowires growth is 400ºC. After the deposition an annealing step is performed at 500ºC during 2h to remove the impurities and fully oxidize the layer of nanowires.

Once the layer is obtained the proceedure to dope it with cobalt nanoparticles is the same as the nanowires synthesis**[2]**. To obtain different doping concentrations, two solutions were prepared; 5 mg and 10 mg $Co(acac)_2$ as precursor were each dissolved into 10 ml of methanol. The nanoparticles deliver was performed at 350ºC, under a flow of 15 ml/min, through the AACVD process. Once the doping was completed, the sensors underwent a second annealing, under the same conditions, in which the impurities are removed and the nanoparticles are oxidized. The nanoparticle (p-type) and the nanowires (n-type) would create active heterojunctions were the gas would interact with them.

The sensors were fully characterized through environmental scanning electron microscope (E-SEM), high resolution tunneling electron microscope (HR-TEM) and X-Ray diffraction (XRD), in order to obtain information of the whole sensing layer structure.

The sensors performance as gas sensors was tested through a series of different gases at diverse concentrations under dry air conditions**[3]**. The experiment was set as 30 minutes pulses, in which each pulse consisted on shifting synthetic air with a target gas (**Figure 1**). The steps were designed in order to expose the sensor, clean it with air and exposing it again to a higher gas concentration. Different temperatures, (150, 200 and 250ºC), were also tested in order to determine which were the best operating conditions for each gas tested

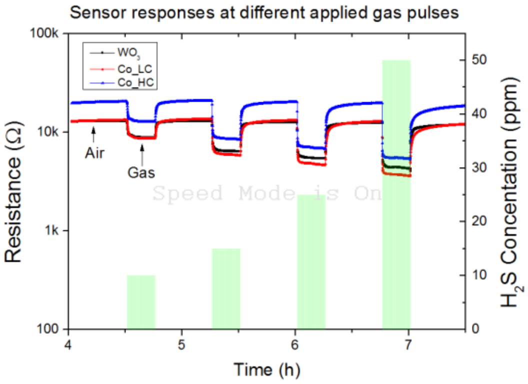

Figure 1. Sensor response at different applied gas pulses.

3. Results and discussion

The structural results for the sensor's characterization showed the growth of nanowire forest in which, typically, with an average nanowire width was 50 nm and average length was 11.5 µm as it can be seen in **Figure 2**. The XRD results for the analyzed nanowires displayed a triclinic crystal phase belonging to the spatial group P-1. Due to the sizes and the low wt% of CoOx nanoparticles they could not be analyzed as they were found to be under XRD detection limit.

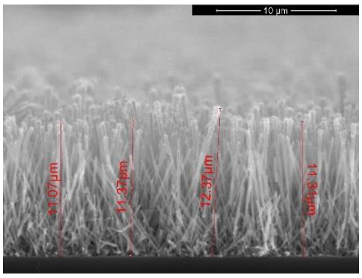

Figure 2. E-SEM WO_3 nanowires layer cross-section.

Even though, the cobalt nanoparticles presence was confirmed using EDX.

The gases tested were H_2S, H_2, EtOH. For each gas the sensors displayed different behaviors giving the higher response towards H_2S among the others. Also one important parameter was the temperature. In order to compare and contrast the effect of the dopant, a pure WO_3 sensor was also tested under the same conditions. The results are shown in **Figure 3**.

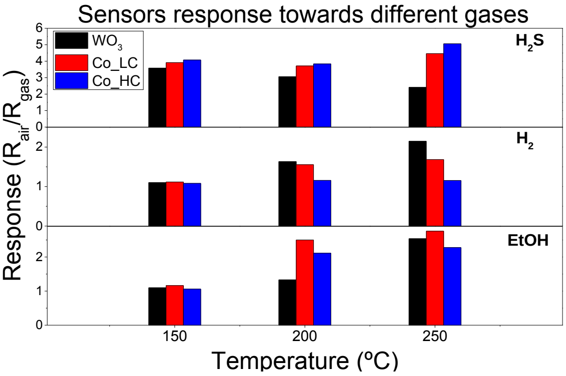

Figure 3. Sensors response at different temperatures and gases.

The response is given in means of the difference between the resistance (ohms) under the synthetic air and the resistance (ohms) of the target gas.

For all temperatures H_2S was the gas which displayed the highest signal, for all the cases. As it can be seen the addition of cobalt at the sensors surface enhances the sensitivity of the layer. Furthermore, a higher concentration of CoO_x nanoparticles leads to a higher response even though the increase is slight. For the H_2 results it can be seen that the addition of CoO_x nanoparticles have an opposite behavior in comparison to H_2S. At higher concentrations of CoO_x nanoparticles the sensing properties and the response given by the sensors decrease. This effect is also affected by the temperature, high temperatures boost the deactivation of the sensing layer in comparison to the pure WO_3 sensor. Ethanol results have shown an increase in sensors response after the doping in comparison to the pure WO_3 sensor. The sensor which displays the best response is the one doped with the lower amount of CoO_x which can lead to the conclusion that higher concentrations could lead to a deactivation of the sensing layer.

4. Conclusions

We have been able to develop a new nanostructured sensors using a two steps methodology. The results have shown that cobalt oxide nanoparticles doping leads to a selectivity and sensitivity increase towards H_2S. Temperature is a key parameter which has to be controlled as it modifies the system behaviour either in a positive (increase the response) or negative (decrease of the response) way. Furthermore, the doping wt% it also have different behaviours among the gases tested. Therefore, combining the operation temperature and the correct loading the sensor can be successfully tuned to be more selective to gases.

5. References

[1] Fatima E. Annanouch, Z. Haddi, M. Ling, F. Di Maggio, S. Vallejos, T. Vilic, Y. Zhu, T. Shujah, P. Umek, C. Bittencourt, C. Blackman, E. Llobet (2016): Aerosol-Assisted CVD-Grown WO_3 Nanoneedles Decorated with Copper Oxide Nanoparticles for the Selective and Humidity-Resilient Detection of H_2S. ACS Appl. Mater. Interfaces, **8**, 10413.

[2] S. Vallejos, P. Umek, T. Stoycheva, F. Annanouch, E. Llobet, X. Correig, P. De Marco, C. Bittencourt and Chris Blackman (2013): Sensors: Single-Step Deposition of Au- and Pt-Nanoparticle-Functionalized Tungsten Oxide Nanoneedles Synthesized Via Aerosol-Assisted CVD, and Used for Fabrication of Selective Gas Microsensor Arrays. Adv. Fun. Mat, **23**, 1226.

[3] S. Roso, C. Bittencourt, P. Umek, O. González, F. Güell, A. Urakawa, E. Llobet (2016): Synthesis of single crystalline In_2O_3 octahedra for the selective detection of NO_2 and H_2 at trace levels. J. Mater. Chem. C, **4**, 9418.

Use of chemical shift information to improve profiling quality and insights in 1H-NMR datasets

Daniel Cañueto

1. Introduction

Metabolomics consists of the study of metabolites in biofluids and cell or tissue extracts of animals and plants. 1H-NMR is a high-throughput technique that enables the quantification of metabolites in a reliable and reproducible manner [1]. Quantification of metabolite concentration in 1H-NMR spectra is performed through the quantification of the area below the curve of a signal present in the spectrum. Every metabolite present in a sample has a characteristic pattern of signals in a 1H-NMR spectrum. Recent tools have been published to perform the automatic quantification of signals in 1H-NMR spectra.

Nevertheless, the sample properties and preparation and the selection of NMR spectral acquisition and preprocessing parameters can incorporate variability to the generated data sets. Misalignment of signals along a spectrum dataset represents one of the biggest challenges to overcome in the reliable identification and quantification of signals in automatic quantification approaches. This misalignment is caused by intervariability in properties such as pH or ionic strength [2]. This variability causes different chemical environment of a metabolite in every sample, and the location (called in NMR “chemical shift”) of its signals is altered by this different chemical environment. The misalignment of signals may hamper the right identification and optimal deconvolution of overlapping signals.

Current strategies to overcome signal misalignment try to minimize it through sample preparation or signal alignment algorithms. Nonetheless, sample preparation has limited effectiveness and can produce unwanted metabolite concentration variations. Likewise, alignment algorithms cannot align low-intensity signals and are liable to wrong identifications. Furthermore, the chemical shift of signals gives valuable information about sample properties that may be useful to increase the insights found in samples. Ideally, a spectrum dataset should maintain as much information provided by the chemical shift variability as possible, but this variability should be predicted during the quantification of signals.

2. PhD Objectives and Methods

2.1. Redesign of tool developed by the group into an open-source R package with expanded functionalities

The R-based reimplementation, called rDolphin, is more robust to most common challenges (reliable identification, robustness to variability in signal parameters) in the automatic quantification of metabolite signals and is able to output more information necessary to expand the analysis of signal properties.

Examples of new capabilities allowed by this redesign are:

- Post-profiling and evaluation of sub-optimal quantifications caused e.g. by appearance of overlapping signals to the one of interest in some spectra.
- Improvement of evaluation of identification of signals using dendrogram heatmaps of quantification and chemical shift information. Metabolites with similar functionality will share quantification patterns with the signal of interest. Metabolites with similar chemical structure will share chemical shift patterns with the signal of interest.

Published results in improvements enabled by this redesign should be published during last PhD year.,

2.2. Use of compiled chemical shift information to achieve better separation between groups of samples

The redesign of the tool enables the acquisition of reliable chemical shift information of dozens of signals. This information can be added to the quantification information to generate a better separation in multivariate analyses between groups of samples of public datasets. Results show that there is a much better separation between samples that is justified by reported pH differences between these groups. These findings could help NMR to increase its diagnostic and predictive properties for promising areas such as precision medicine.

Published results of this study should be published during last PhD year.

2.3. Prediction of chemical shift of signals according to the chemical shift of other signals.

Automatic approaches to quantify signals tend to rely on the optimization of the signals parameters (e.g. intensity, chemical shift or half bandwidth) to perform the best possible line shape fitting of a spectrum region. The more variability needed during the parameters optimization, the higher number of wrong identifications and suboptimal fittings because of signal overlapping and misalignment. Both wrong identifications and suboptimal fittings can be greatly reduced if the allowed variability to chemical shift is minimized.

This bottleneck can be greatly reduced taking advantage of the multicollinearity of the data. Chemical shift of metabolite signals follows several general patterns related to the functional groups of metabolites. This causes high correlation between signals coming from relatively similar metabolites. This collinearity can be used to predict the chemical shift of a signal based on the chemical shift of other signals. This approach helps find quantifications where the chemical shift of a signal behaves as a multivariate outlier (Figure 1).

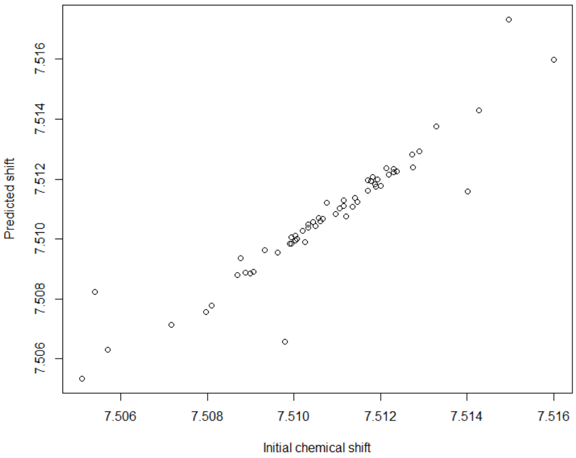

Fig.1. Comparison between during chemical shift of a signal in automatic quantification and predicted chemical shift. The signal is suboptimally identified in several cases. Prediction is able to constrain the chemical shift tolerance from 0.01ppm (7,516-7.506) to less than 0.001 ppm.

References

[1] Barding, Gregory A., Jr, Ryan Salditos, and Cynthia K. Larive. 2012. “Quantitative NMR for Bioanalysis and Metabolomics.” Analytical and Bioanalytical Chemistry 404 (4): 1165–79.

[2] Xiao, Chaoni, Fuhua Hao, Xiaorong Qin, Yulan Wang, and Huiru Tang. 2009. “An Optimized Buffer System for NMR-Based Urinary Metabonomics with Effective pH Control, Chemical Shift Consistency and Dilution Minimization.” The Analyst 134 (5): 916–25.

Design of a bidirectional DC/DC converter with coupled inductor for an electric vehicle application

Catalina González Castaño, Enric Vidal Idiarte, Javier Calvente

Automatic Control and Industrial Electronics Group (GAEI). Universitat Rovira I Virgili. Avinguda dels Paisos Catalans, 26 Tarragona-Spain.
Email: catalina.gonzalez@urv.cat

Abstract

The aim of this work is to implement a bidirectional buck-boost converter prototype to regulate DC voltage in a powertrain of an electric vehicle. To validate the design of the proposed converter start-up transient experiments are realized in open loop. The activation signals are implemented in a microcontroller. Experimental results show its works properly, keeping the criteria design parameters.

1. Introduction

Nowadays, the demand of DC power devices for automotive electronic is continuously being increased. Important applications involving electric cars powered. Therefore, the high efficiency of the power system is a topic important in the electric vehicle system. Efficient topologies of DC-DC converter have been used to connect the battery with the inverter-motor in a vehicle application to regulate DC voltage and improve the performance of traction motor [1], [2]. With the aim to hold the battery rated voltage independent from the high-voltage DC bus necessary to deliver power to the motor and the optimization of vehicle operation, we consider a bidirectional DC/DC converter with inductor coupled at the input and the output. The characteristics of this converter are high stability, efficiency and wide bandwidth. Recently, this converter is widely used in any system that needs to charge and discharge backup batteries and can be applied in space, fuel cell, photovoltaic and telecom power systems [3], [4], [5], [6]. In this work, we propose the design and implementation of a bidirectional buck-boost converter with coupled inductor prototype. The design of converter was made taking into account the specifications of a powertrain emulator of an electric vehicle. Finally, experimental results are shown, which are developed using a active load in constant resistance mode and a power resistor. Proposed prototype works properly in buck and boost mode, and according with the criteria design, begin a good alternative to start with the application for an electric vehicle operation.

2. System description

To describe the operation of the proposed application, a block diagram is considered and it is detailed in Figure 1, which consists in a battery and a buck-boost converter block that has as function to keep the different rating voltage between the battery and the inverter to deliver power to the motor. The converter cell showed in Figure 2(a) is bidirectional, thereby, works in traction mode to allow power deliver from the battery to the motor and in regenerative brake mode to recharge the battery when the vehicle brakes.

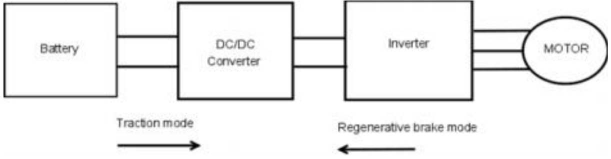

Fig 1. Block diagram of the DC/DC converter in traction system.

3. Buck-boost dc/dc converter with coupled inductor

A buck-boost dc/dc converter is described in [4]. The buck-boost cell is shown in Figure 2(a), and it includes a damping network composed by a resistor R_d and a capacitor C_d, they are connected in series between them and in parallel with the capacitor C. The components R_d and C_d are calculated as follows:

$$R_d = 0.65\sqrt{\frac{L_m}{C}}, C_d = 8C \qquad (1)$$

$$P_{Rd} = \frac{\Delta v_{cpp}^2}{12 R_d}$$

Where C is the intermediate capacitor and L_m is the magnetic inductance value of the coupled inductor. The power losses in R_d (P_{Rd}) are presented in [3]. The value P_{Rd} is given by the value rms of alternate component of v_{cpp} and assume that it has a triangular shape.

The buck-boost cell works as follows: u_{1H} and u_{1L} are switched in complementary manner while u_{2H} is set at 1 and u_{2L} is set at 0, in boost mode. In this way, u_{2H} and u_{2L} are switched in complementary manner while u_{1H} is set at 1 and u_{1L} is set at 0, in buck mode. These activation signals are generated using a duty cycle for each operation mode, $d_1(t)$ and $d_2(t)$. This allows to operate in boost mode when Q_1 and Q_2 are switched with the duty cycle $d_1(t)$ and in buck mode when Q_3 and Q_4 are switched with the duty cycle $d_2(t)$ in Figure (2).

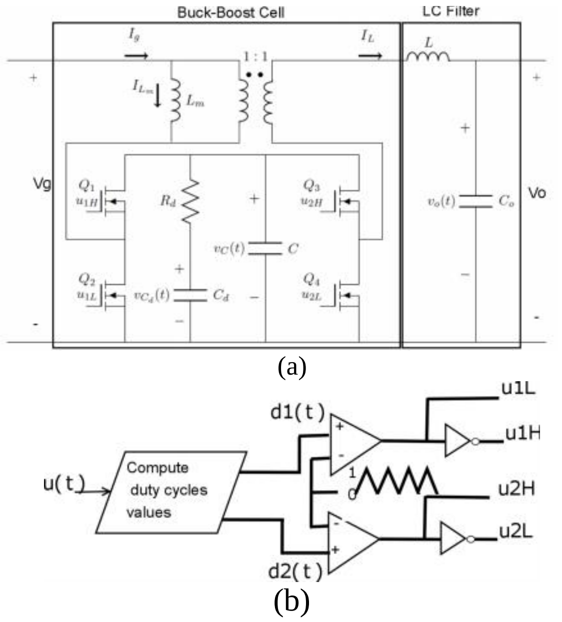

Fig 2. Diagram of: (a) buck-boost converter (b) switch signals generation.

4. Experimental results

Experiments are carried out over a buck-boost cell prototype described in Figure 2. The selected components are summarized in Table I.

Component	Description	Reference
Q_1,Q_2,Q_3,Q_4	Silicon Carbide Power MOSFET	C2M0080120D
C	Polypropylene Capacitor, 4 x 0.33uF	R76PN3330430J
R_d	Damping resistor, 10Ω,10W,500V	BPR10100J
C_d	Damping Capacitor Polypropylene 10uF, 700V	MKP1848S61070JP2C
L_m	Couple inductor 285uH	Core:7908 Magnetics, Wire size:30 AWG, Number turns:93

Table 1. Buck-boost cell components.

A direct voltage source is used as power supply for the buck-boost cell. The Enhanced Pulse Width Modulator (ePWM) module from Texas Instruments TMS320F28377S Digital Signal Control (DSC) has been used to generate the activation signals for the MOSFETs switch. Experimental results are showed in Figure 3.

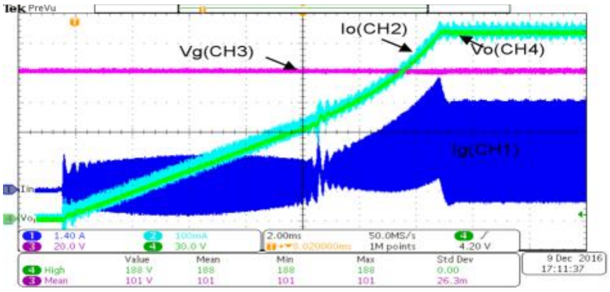

Fig 3. Experimental results with resistor of 300Ω and final output voltage in boost mode. CH1: input current Ig (1.4 A/div); CH2: current in theload Io (100 mA/div); CH3: input voltage Vg = 200 V (20 V/div); CH4: output voltage Vo (30 V/div); time base 4 ms.

7. Conclusions

A bidirectional buck-boost converter with coupled inductor, is presented as an alternative to conventional converter topologies in electric vehicle application.

A buck-boost cell has been design and validated. Such a prototype has proven to be a suitable for operation in buck and boost mode.

Experimental results agree with the simulated ones and again validate the converter design. Although the tests were realized in open loop, the effect of oscillation in the transition was not significant.

As a future work, we are aiming at testing the prototype to high power under different control techniques in close loop, with rated voltage and connecting multiple buck-boost modules in parallel for the application.

References

[1]D. Northcott, S. Filizadeh, and A. Chevrefils, “Design of a bidirectional buck-boost dc/dc converter for a series hybrid electric vehicle using pscad/emtdc,” in *2009 IEEE Vehicle Power and Propulsion Conference*. IEEE, 2009, pp. 1561–1566.

[2] M. Rezal and A. Faiz, “Bidirectional buck-boost controller for electric vehicle using fpga board,” 2014.

[3]E. Sanchis, E. Maset, A. Ferreres, J. B. Ejea, V. Esteve, J. Jordan, J. Calvente, A. Garrigos, and J. M. Blanes, “Bidirectional high-efficiency nonisolated step-up battery regulator,” *IEEE Transactions on Aerospace and Electronic Systems*, vol. 47, no. 3, pp. 2230–2239, 2011.

[4] C. Restrepo, J. Calvente, A. Cid-Pastor, A. El Aroudi, and R. Giral, “A noninverting buck–boost dc–dc switching converter with high efficiency and wide bandwidth,” *IEEE Transactions on Power Electronics*, vol. 26, no. 9, pp. 2490–2503, 2011.

[5] H. Ram´ırez-Murillo, C. Restrepo, J. Calvente, A. Romero, and R. Giral, “Energy management of a fuel-cell serial–parallel hybrid system,” *IEEE Transactions on Industrial Electronics*, vol. 62, no. 8, pp. 5227–5235,2015.

[6] H. Ram´ırez-Murillo, C. Restrepo, J. Calvente, A. Romero, and R. Giral, “Energy management dc system based on current-controlled buck-boost modules,” *IEEE Transactions on Smart Grid*, vol. 5, no. 5, pp. 2644–2653, 2014.

Compact Modeling of Intrinsic Capacitances in Double-Gate Tunnel-FETs

A. Farokhnejad[1, 2,*], F. Horst[1, 2], M. Graef[1,2], C. Liu[3], Q.T. Zhao[3], B. Iñiguez[2], F. Lime[2], A. Kloes[1]
[1]NanoP, TH Mittelhessen University of Applied Sciences, Giessen, Germany
[2]DEEEA, University Rovira i Virgili, Tarragona, Spain
[3]PGI 9-IT and JARA-FIT, Forschungszentrum Jülich, Germany
[*]atieh.farokhnejad@ei.thm.de

***Abstract*—In this paper an AC-model for a TFET is presented. By means of the carrier concentration and current in the channel, the intrinsic capacitances in a Si Double-Gate (DG) n-TFET are calculated. To verify the model, the results are compared with TCAD Sentaurus simulations as well as measurement data. The model represents a particularly good manifestation of the device AC behavior and is a good estimation of TFET capacitances.**

Keywords- Tunnel-FET; compact model; AC model; intrinsic capacitances.

I. INTRODUCTION

Recently TFETs are in the center of the attractions to be the surrogate of the standard MOSFET. This ever increasing interest owes to their feasibility to overcome the 60 mV/dec subthreshold slope limitation of the standard MOSFETs [1].

In order to allow circuit simulations using multiple TFETs, compact models describing different aspects of the device for all operation regions are necessary. In [2] a DC compact model has been presented. This paper presents a compact model for the intrinsic capacitances in TFETs. The modeled device, is a Si DG n-TFET with a highly p-doped source region N_s=10^{20} cm^{-3}, a highly n-doped drain region N_d=10^{20} cm^{-3} and an intrinsic channel (see Fig. 1).

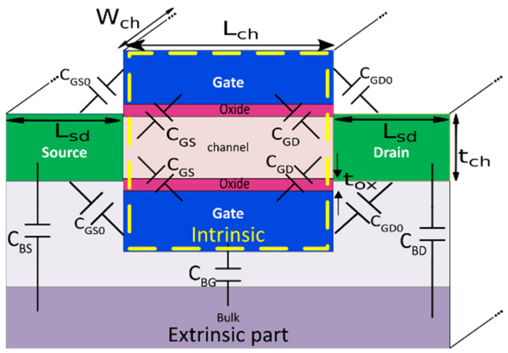

Fig.1. Device geometry and capacitances of a DG TFET. The AC modeling approach focuses on the intrinsic part.

Dimensions of the device are selected as following: L_{sd}=20 nm, t_{ch}=10 nm, W_{ch}=1 µm and t_{ox}=2 nm. Moreover, the high-k oxide material HfO$_2$ is used in the structure. The model can also be adapted to p-channel and single gate devices.

II. MODELING APPROACH

The charges which are stored in the transistor yield to a capacitive behavior of the device. Fig. 1 shows the important capacitances in a DG TFET. Here the focus lays on the intrinsic capacitances which are distinct in this figure.

To calculate C_{gd} and C_{gs}, firstly the charge density has to be calculated. In order to do so, it is assumed that the tunneling barrier is the bottleneck for the current flow in the channel. It is also presumed, that in the on-state, this barrier is in distance of $X_{b,s}$ from the source junction and in the ambipolar-state $X_{b,d}$ from the drain junction.

According to these assumptions and considering the inversion charge in the channel region in a multi-gate device [3], the charge density in the channel region at a position with reference voltage V is given as following

$$Q' = 2C'_{eff}V_{th}\alpha \times \mathcal{L}\left(\frac{Q'_{io}\cdot exp\left(\frac{2C'_{eff}\left(V_{gs}\text{-}V\text{-}V_0\right)+Q'_{io}}{2C'_{eff}V_{th}\alpha}\right)}{2C'_{eff}V_{th}\alpha}\right). \quad (1)$$

Where V_{th} is the thermal voltage and α is the slope degradation factor which expresses the ratio between the degraded and the ideal slope in the channel region. Q'_{i0} is the integral inversion charge for an arbitrary gate bias of V_0 in the subthreshold regime [3]. $\mathcal{L}$ is the first branch of Lambert's W function [4]. C'_{eff} represents the effective capacitance including oxide and depletion capacitances in series.

The analysis of long-channel TFETs has shown, that the voltage drop in the channel (ΔV) has to be taken into account. In order to calculate ΔV, firstly the current has to be determined using the DC compact model [2]. Then by multiplying it to the resistivity of the channel between the junction and the tunneling barrier ΔV is obtained. Next, the charge density at the drain junction ($Q'_{d,j}$) and at the barrier ($Q'_{d,b}$) are calculated by solving (1) for V=V_d and V=V_d−ΔV, respectively.

In the same way, just by applying V_s instead of V_d, Q'_s is obtained and the total inversion channel charge associated with source and drain are given as

$$Q_{ch,s/d} = \frac{\left(Q'_{s/d,j} + Q'_{s/d,b}\right)}{2}\, W_{ch}\left(L_{ch}\text{-}X_{b,s/d}\right). \qquad (2)$$

Considering the $\Delta Q_{ch,s}$ and $\Delta Q_{ch,d}$ in accordance with changes in source or drain voltage, capacitances are obtained. So in on-state the capacitances are given as

$$C_{gs} = \frac{\Delta Q_{ch,d}}{\Delta V_s} \quad \text{and} \quad C_{gd} = \frac{\Delta Q_{ch,d}}{\Delta V_{ds}} \qquad (3)$$

and in ambipolar-state

$$C_{gs} = \frac{\Delta Q_{ch,s}}{\Delta V_s} \quad \text{and} \quad C_{gd} = \frac{\Delta Q_{ch,s}}{\Delta V_{ds}}. \qquad (4)$$

III. MODEL VERIFICATION AND CONCLUSION

To inspect the scalability of the AC model, various V_{ds} and L_{ch} are examined. Increasing the drain voltage leads to a shift of the Fermi potential and it lowers the charge attribution to the drain. This is the reason why in Fig. 2 by increasing the V_{ds} the gate-gate capacitance (C_{gg}), which is the summation of C_{gs} and C_{gd}, decreases in the on-state. The longer the channel, the more charges exist in the channel, and thus a bigger capacitance is expected. In Fig. 3 the modeled C_{gs} and C_{gd} are compared with TCAD simulations for different L_{ch}. The model fulfills the expectations and fits very well to the TCAD results.

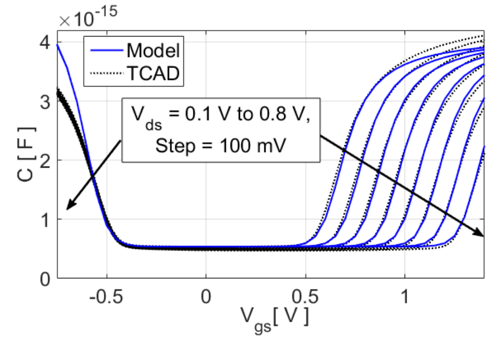

Fig. 2. C_{gg} is compared with TCAD results for various drain voltages. L_{ch}=22 nm, α=1.62, $X_{b,s/d}$ = 3 nm, $V_{0\text{-}gs}$ = -0.19 V, $V_{0\text{-}gd}$ = -0.22 V.

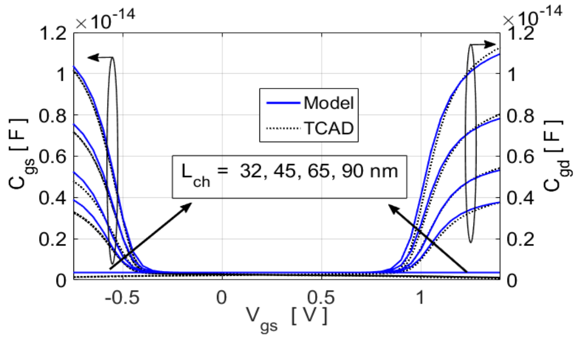

Fig. 3. C_{gs} and C_{gd} are compared with TCAD for various channel lengths. α = 1.53...1.61, $X_{b,s/d}$ = 3 nm, V_{ds} = 0.5 V, $V_{0\text{-}gs}$ = -0.19 V, $V_{0\text{-}gd}$ = -0.22 V.

The model is also compared with measurement data of a p-type single-gate planar TFET. The device dimensions are as following: L_{ch}=11 µm, t_{ch}=10 nm, t_{ox}=5 nm HfO$_2$ and W_{ch} =10 µm. In this case, additionally to the voltage drop along the channel, the influence of the parasitic resistances is also included in the model. Along these lines, C_{gs} and C_{gd} are defined as presented in [5].

In Fig. 4 C_{gd} and C_{gs} of the planar TFET, in both on and ambipolar state, are compared with model results. Considering the voltage drop in the channel, in the on-state part of the charges are attributed to the source and in the ambipolar-state they are under the control of the drain [6]. Hence, an increment in C_{gs} and C_{gd} in respectively on-state and ambipolar-state can be seen. The results are in a good agreement with the measurement data as well.

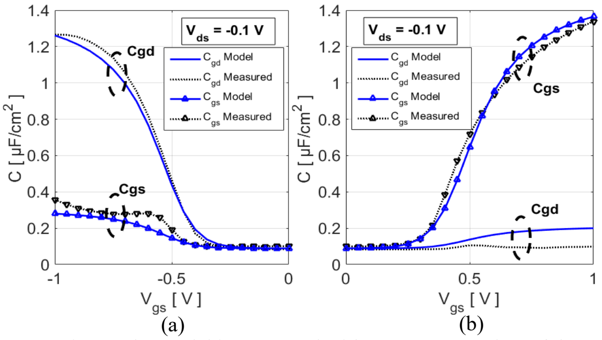

(a) (b)

Fig. 4. The model is compared with measurement data of the planar p-TFET: (a) On-state (b) Ambipolar-state. L_{ch}= 11 µm , α=2.3, $X_{b,s/d}$ = 3 nm, $V_{0\text{-}gs}$ = 0.01 V, $V_{0\text{-}gd}$ = 0.06 V.

ACKNOWLEDGMENT

This project was supported by the German Federal Ministry of Education and Research under contract No. FKZ 03FH010IX5 and Spanish Ministry of Economy and Competitiveness through project GREENSENSE TEC2015-67883- R. We would like to thank Keysight Technologies for the license donation and support of the software IC-CAP and AdMOS GmbH for support.

REFERENCES

[1] A. C. Seabaugh, and Q. Zhang, “Low-Voltage Tunnel Transistors for Beyond CMOS Logic,” *Proceedings of IEEE*, vol. 98, no. 12, pp. 2095-2110, 2010.

[2] F. Horst, et al. "Implementation of a DC compact model for double-gate Tunnel-FET based on 2D calculations and application in circuit simulation." *Solid-State Device Research Conference (ESSDERC), 2016 46th European*. IEEE, 2016.

[3] A. Kloes, M. Schwarz, T. Holtij, and A. Navas, “Quantum Confinement and Volume Inversion in MOS3 Model for Short-Channel Tri-Gate MOSFETs,” *Electron Devices, IEEE Transactions*, vol. 60, pp. 2691-2694, 2013.

[4] R. M. Corless, G. H. Gonnet, D. E. G. Hare, D. J. Jef and D. E. Knuth, “On the Lambert W Function,” *Adv. Comput. Math., vol. 5, pp. 329–359*, Feb. 1996.

[5] T. Smedes, and F. M. Klaassen. "Influence of channel series resistances on dynamic MOSFET behaviour." *Solid-state electronics* 37.2 (1994): 251-254.

[6] C. Liu, et al. "Experimental I–V (T) and C–V Analysis of Si Planar p-TFETs on Ultrathin Body." IEEE Transactions on Electron Devices 63.12 (2016): 5036-5040.

MoS_2-Carbon Nanotube Hybrid Material for Ultrasensitive Gas Sensing

J. Casanova-Chafer [1*], G. Deokar [2], P. Vancso [2], J. Dervaux [3], Ph. Lambin [2],
J-F. Colomer [2], E. Llobet [1*]

[1] MINOS-EMaS, Universitat Rovira i Virgili, Tarragona, Spain
[2] CARBONNAGe, University of Namur, 61 Rue de Bruxelles, 5000 Namur, Belgium
[3] ChIPS, CIRMAP, Research Institute for Materials Science and Engineering, University of Mons, Mons, Belgium

*Correspondence: juan.casanova@urv.cat; eduard.llobet@urv.cat

1. Abstract

Vertically aligned carbon nanotubes (va-CNT) were produced by chemical vapor deposition (CVD) technique and hexagonal-shaped nanoplates (HNPs) of MoS_2 were deposit on va-CNT. Each MoS_2 HNP consists of several (20 - 30) stacked MoS_2 layers having a thickness around 20 nm and a length of a few hundreds of nanometers. We have found that the multilayered MoS_2 HNPs on va-CNT system exhibits sensitive, selective and low limit of detection of NO_2 making it a potential sensor device. The observed NO_2 detection in parts per billion (ppb) range with limit of detection of 2 ppb, achieved by this hybrid material is lower as compared to the literature.

2. Introduction

NO_2 being one of the most common and toxic air pollutants from combustion and automotive emissions, can cause serious diseases even at low concentrations. Therefore, it is of high importance to detect NO_2 accurately and reliably for human health protection by air monitoring. Using CNTs as NO_2 gas sensor was first proposed by Kong et. Al[1], because CNTs presents intrinsic properties such as high electron mobility and adsorption capability, large surface are to volume ratio and physic-chemical stability.

The functionalization of CNTs by organic polymers or catalytic metal nanoparticles was found to be a good strategy to enhance the sensitivity and the selectivity of the CNT-based sensors[2]. Here, we present our work on CNT functionalized with semiconducting material (MoS_2). It has been reported that MoS_2 structural defects including grain boundaries, point defects, and edges, play significant roles in sensing applications. Open challenges, such as large-scale fabrication of sensors, their selectivity tuning and noise reduction, still remain. With the increasing demand of highly sensitive, fast, and stable sensors, a series of sensing applications of nanoscale MoS_2-based composite and hybrids have been of growing interest[3].

In this work, we have exploited MoS_2/CNT hybrid materials for gas sensing application. The hybrid material was synthesized using a two-step CVD technique. The high quality of the produced hybrid material revealed by employing various characterization techniques. The obtained MoS_2 hexagonal-shaped nanoplates (HNPs) consists of highly crystalline structures and have abundant exposed edges. The sensing performance of the MoS_2/CNT hybrid system for NO_2 and NH_3, was studied. The hybrid samples containing MoS_2 HNP with exposed edges showed excellent gas sensing results with NO_2 detection in parts per billion (ppb) range.

3. Material characterization

The hybrid heterostructure synthesis was divided in two steps: 1) growth of va-CNTs on Si surface, 2) sulfurization of Mo film deposited on va-CNTs to produce MoS_2 HNPs.

The morphology of the synthesized material was examined by Scanning Electron Microscope (SEM), and the chemical composition was analysed by Raman spectroscopy (**figure 1**).

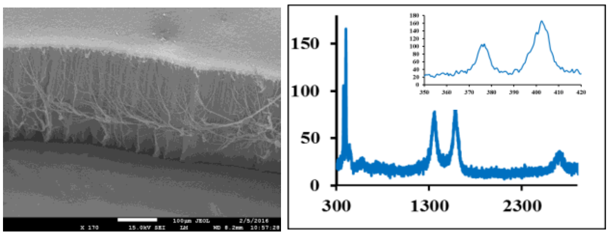

Fig.1. Cross-section SEM and Raman Spectra

The MoS_2 material can be clearly seen, especially on the top of the CNTs with cross-section SEM. Moreover, the Raman measurements revealed the crystalline multi-layered CNTs due to the presence of Raman modes at 1350 cm^{-1} (D band) and 1580 cm^{-1} (G band) and second order 2780 cm^{-1} (2D band). In addition, the presence of E^1_{2g} (376.8 cm^{-1}) and A_{1g} (402.4 cm^{-1}) peaks demonstrate the high crystalline MoS_2 deposit. Finally, the results showed were confirmed by other techniques, such as TEM, Angular-resolved Near-Edge X-ray Absorption Fine Structure (NEXAFS) and XPS.

4. Gas sensing results

To fabricate the sensor device, the MoS$_2$/CNT hybrid samples were processed as follows. Two wire contacts were made on the surface of samples by employing a silver paste and Pt wires. Samples were glued with a thermally conductive epoxy to an alumina heating plate and wire bonded to a printed circuit board, which can be connected inside a 35 ml test chamber (**Figure 2**). This chamber was connected to a fully automated, continuous flow measurement set-up in which reproducible concentrations of dry or humidified gas mixtures could be delivered by mass-flow controllers.

Fig.2. Used test chamber and example of fabricated sensor.

It is well-known that NO$_2$ acts as an electron acceptor while NH$_3$ acts as an electron donor. Thus, for a p-type semiconductors, such as our samples, NO$_2$ decreases their resistance while NH$_3$ increases their resistance based on a charge-carrier transfer mechanism. Our results show a clear enhanced response of the MoS$_2$/CNT system to both NO$_2$ and NH$_3$, however, the response to NH$_3$ is very low in comparison to NO$_2$, in consequence, our hybrid material is quite selective to NO$_2$. The adsorption process was operated at room temperature, but a heating process is required to desorb the molecules and recover the resistance baseline.

The high response to NO$_2$ (ppm range) is clearly visible in **Figure 3**, moreover, the response of the hybrid nanomaterial to lower concentrations was also investigated. **Figure 3** shows also the response to 25 ppb, considering the noise levels present in the signals, the limit of detection (LOD) for NO$_2$ can be estimated to be near 2 ppb. To the best of our knowledge, a successful detection of 25 ppb of NO$_2$ together with a LOD of 2 ppb employing MoS$_2$ has never been reported before.

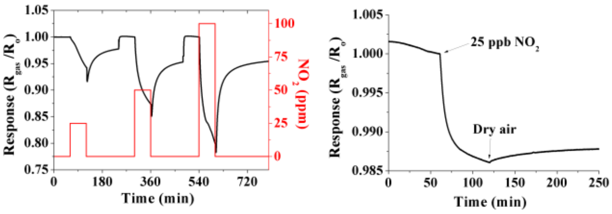

Fig.3. MoS$_2$/CNT **r**esponse to concentrations of NO$_2$.

The pristine va-CNT system has lower sensitivity compared to MoS$_2$/CNT because the exposed edges of MoS$_2$ HNPs might play dominant role in the gas sensing mechanism. For that reason, the increased p-doping at edges explains the enhanced sensitivity.

The MoS$_2$/CNT system performance for NO$_2$ sensing was also tested in humidity conditions (**Figure 4**). In the presence of humidity, the response towards 50 ppm of NO$_2$ significantly increases. A further increase in humidity level (e.g. from 30% to 50%) yields a smaller additional-increase of the response to NO$_2$. In general, the response was enhanced about 60% in humid conditions, independently on humidity level. Because water vapour is considered to be an electron acceptor similar to NO$_2$, the further increase of the response for NO$_2$ at higher R.H values can be qualitatively understood.

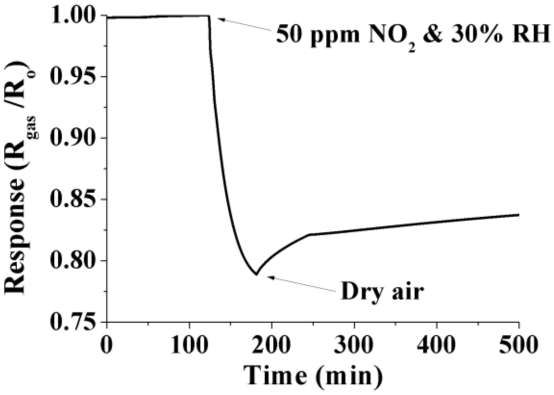

Fig.4. Enhanced response to NO$_2$ in humidity conditions.

5. Conclusions

Hexagonal-shaped MoS$_2$ nano-platelets on the va-CNT template were synthesized by CVD technique. The growth of MoS$_2$ HNPs of high crystallinity was confirmed by Raman, XPS, NEXAFS and TEM characterization. We have further demonstrated an efficient MoS$_2$/CNT hybrid gas sensing systems with: (i) high sensitivity and selectivity; (ii) low analyst consumption; (iii) sensitivity to both low and high concentrations; (iv) stability; (v) reproducible gas sensing cycles. The excellent NO$_2$ sensing response of the MoS$_2$/CNT hybrid system comes from the large affinity of NO$_2$ for MoS$_2$ HNPs edges and the more significant charge transfer at the edges. The current result could be beneficial for future studies to improve further the detection limits in parts-per-trillion sensitivity regime.

References

[1] Kong, J.; Franklin, N.; Zhou, C.; Chapline, M.G.; Peng, S.; Cho, K.; Dai, H. Nanotube molecular wires as chemical sensors. Science 2000, 287 (5453), 622-5.

[2] Zhang, T.; Mubeen, S.; Myung, N. V.; Deshusses, M. A. Recent progress in carbon nanotube-based gas sensors. Nanotechnology 2008, 19 (33), 332001.

[3] He, Q.; Zeng, Z.; Yin, Z.; Li, H.; Wu, S.; Huang, X.; Zhang, H. Fabrication of flexible MoS2 thin-film transistor arrays for practical gas-sensing applications. Small 2012, 8 (19), 2994- 9.

3D-FDTD MODELLING OF GOLD-COATED NANOPOROUS ANODIC ALUMINA FOR OPTICAL BIOSENSING

Francesc Bertó-Roselló, Josep Ferré-Borrull, Elisabet Xifré-Pérez, Lluis F. Marsal*

Universitat Rovira i Virgili, Avinguda Països Catalans, 26, 43007, Tarragona, Spain

* *lluis.marsal@urv.cat*

Abstract

The possibility of using a plasmonic-nanoporous anodic alumina based structure as a platform to be suitable in the development of optical/plasmonic biosensors is investigated here. Reflectance simulations on this kind of photonic structures covered by a gold layer were made employing a 3D-FDTD based numerical procedure.

1. Introduction

Nanoporous anodic alumina (NAA) is a nanomaterial who has gained importance in the last years from the point of view of their physical, chemical and optical properties. The NAA is produced by electrochemical etching of the aluminum by means of the so-called two-step anodization process in acid electrolytes under potentiostatic conditions. The final result is a matrix of aluminum oxide with cylindrical pores perpendicular to the surface in a hexagonal arrangement. The main NAA parameters that can geometrically define the structure are the inter-pore distance (d_{int}), pore diameter (d_p) and the pore length (L), which are strongly influenced by the fabrication conditions, like the acid electrolyte used, the temperature, the anodization voltage, etc [1].

From the optical point of view, the NAA is a good platform to be used in the development of optical biosensors. The optical properties of NAA (reflectance, transmittance, absorbance, etc…) strongly depends on their characteristic parameters and with a precise control of them the NAA can be used to detect specific chemical and biochemical analytes. Unfortunately, the optical behavior of NAA as produced does not becomes particularly suitable for sensing processes. Then, it is necessary to provide mechanisms to enhance the optical properties of the NAA. It is reported in the literature that the presence of a thin gold film in porous alumina enables localized surface plasmons (LSPR), which may increase the optical properties of the structure [2]. Thus, in this line, and in order to design and optimize the gold-coated NAA structure, the optical behavior prediction becomes critical. Therefore, the numerical modelling of this kind of structures speeds up the analysis of the optical behavior and their performance. Numerical methods for optical modelling such as the transfer-matrix method are not adequate since cannot take into account the intrinsic features of the structure interfaces, the great range of structural parameters, or the inhomogeneities in the chemical composition of the oxide. Thus, a 3D-FDTD based numerical procedure permits to take into account all these features, and simulate the optical behavior of the structure [2].

Our goal is to model with a 3D-FDTD based numerical procedure a possible plasmonic–NAA based biosensor, and evaluate the optical performance of the gold-coated NAA to be applied for sensing under changes of the refractive index of the surrounding medium.

2. Methods

In order to study the LSPR behavior in a plasmonic-NAA structure, we calculated the reflectance spectrum for the structures as depicted in Figure 1.a. Starting from a basic structure that consists in a matrix of aluminum oxide with cylindrical pores perpendicular to the surface, we have considered different NAA structures corresponding to two specific ranges of inter-pore distances. The characteristic dimensions of each structure were: d_{int} = 100 nm and d_p = 33 nm for short inter-pore distances, whereas for the corresponding ones with long inter-pore distances were d_{int} = 450 nm and d_p = 150 nm. In both cases, we considered L= 60 μm for the pore length. The existence of the LSPR was checked by adding a gold layer to the NAA. Finally, the sensing process was simulated by considering the pores filled by a dissolution of PBS. The detection of the analytes was done by the binding of theses analytes onto the gold coating surface and into the pores, and was simulated by the addition of a layer, which will be referred to as ‘biolayer’, with a refractive index variable with respect of that of the filling medium.

For the modelling of the NAA structure we used FDTD Solutions from Lumerical as a computational tool. The optical constants of the materials were provided by the employed software. The computational domain was a unit cell of a hexagonal array of cylindrical pores (Fig. 1.b). Periodic boundary conditions in XY directions to reduce computational cost were implemented. Perfectly matched layers for the Z direction were considered to avoid unwanted reflections. The optical source was established as an incident plane wave perpendicular to the surface of the structure (XY plane) propagating in the negative sense of the Z direction, and in a range of wavelengths from 400 nm to 2000 nm. Finally, in order to collect the reflection data as a function of wavelength, a monitor at the top of the computational domain were located.

3. Results & discussion

LSPR enabling on gold-coated NAA

Figure 2 shows the obtained reflectance results for each inter-pore distance gold-coated NAA considered. Both spectra show a similar behavior: a continuous decrease of the reflectance as the wavelength decreases, particularly important at visible wavelengths. For the gold-coated NAA with short inter-pore distances the reflectance exhibits a minor dip around 600 nm, while the corresponding for long inter-pore distances appears shifted approximately at 750 nm. Besides, more additional dips appear for this long inter-pore distances structure, with a one more much markedly dip at 880 nm. These results demonstrate that the gold-coated NAA can be a used as platform basis to provide a coupling between the perpendicular incident light onto LSPR's.

LSPR sensing with gold-coated NAA

Figure 3 depicts the reflectance spectra corresponding to the gold-coated NAA with a gold thin film thickness of 20 nm and a biolayer of 10 nm thickness, and their sensitivity towards changes with the biolayer refractive index. The range of the spectra has been obtained from 850 nm to 1000 nm for a better reading. Figure 3.a shows a sharp reflectance valley around 880 nm, which shifts with the refractive index of the biolayer coating. Figure 3.b depicts the sensitivity of the structure ($S = \Delta\lambda_{dip}/\Delta n$) and shows that the resonant wavelength increases as the biolayer's refractive index increases in a linear dependence. This result demonstrates that this gold-coated NAA with this valley shift permits the possibility of using the structure as a sensor.

4. Conclusions

In this work, we presented a numerical procedure based on 3D FDTD simulations able to deal with the optical behaviour of gold-coated NAA in order to develop a possible plasmonic–NAA based biosensor. The optical performance of the gold-coated NAA was assessed to be applied for sensing under changes of the refractive index of the surrounding medium.

Simulations have demonstrated that gold-coated NAA with long-interpore distances enabled plasmonic effects and that structure was sensitive to changes of the refractive index of the surrounding medium in a linear trend, being the structure suitable for sensing.

Acknowledgements

This work was supported in part by the Spanish Ministry of Economy, Industry and Competitiveness (MEIC) under grant numbers TEC2015-71324-R and TEC2015-71915-REDT, the ICREA under the ICREA Academia Award and the Catalan authority under project AGAUR 2014 SGR 1344.

Figures

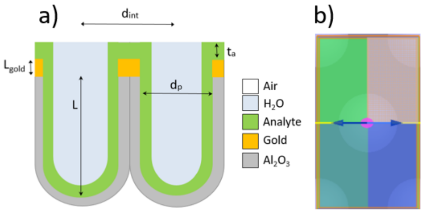

Figure 1. a) Geometric pore model and b) FDTD unit cell.

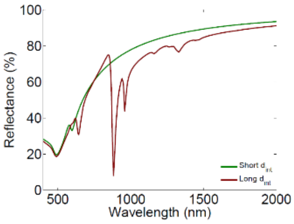

Figure 2. Gold-coated NAA reflectance for short and long inter-pore distances.

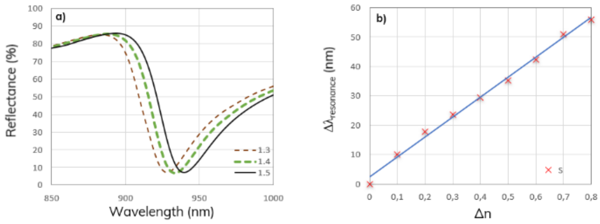

Figure 3. a) Gold-coated NAA reflectance spectra and b) optical sensitivity, both under changes of the biolayer refractive index.

References

[1] T. Kumeria et al., Advanced Structural Engineering of Nanoporous Photonic Structures: Tailoring Nanopore Architecture to Enhance Sensing Properties, ACS Photonics, 2014, 1 (12), 1298–1306.

[2] Prikulis J et al., Optical properties of thin metal films with nanohole arrays on porous alumina–aluminum structures, RSC Adv.,2015, 5,68143–68150

[3] F. Bertó-Roselló et al., Nanoporous Anodic Alumina 3D FDTD Modelling for a Broad Range of Inter-pore Distances, Nanoscale Research Letters 2016, 11, 359.

Ligand-capped AuNPs Gas Sensor Array for Gastric Cancer Diagnosis in Exhaled Breath

Tesfalem G. Welearegay[1,2], A.L. Jaimes[3], O.E. Gualdron[3], C.M. Duran[3], R. Ionescu[1]

[1]MINOS-EMaS, Department of Electronics, Electrical, Automatic and Control Engineering,
Universitat Rovira i Virgili, Av. Paisos Catalans 26, 43007, Tarragona, Spain
[2]Moleculat Fingerprint AB Sweden, SE-75655 Uppsala, Sweden
[3]GISM Research Group, Universidad de Pamplona, Pamplona, Norte de Santander, Colombia
*Email: radu.ionescu@urv.cat, tesfalemgeremariam.welearegay@urv.cat, Tel: +3497755 9610

Abstract

Here we introduce a cross reactive nanomaterial sensor array based on AuNPs capped with different organic ligands, combined with a pattern recognition method for non-invasive early diagnosis of gastric cancer through exhaled breath analysis. The sensor array was directly exposed to exhaled breath collected from volunteers diagnosed with gastric cancer and with non-malignant gastric complains collected using a BioVOC™ breath sampler. The sensor array responses exhibited a clear discrimination of exhaled breath of volunteers with gastric cancer from non-malignant conditions. The classification accuracy achieved success rates between 82.6% and 94.2% employing different supervised and non-supervised pattern recognition methods.

1. Introduction

Gastric cancer (GC) is one of the most common causes of death from cancer, and its earlier diagnosis, treatment and post monitoring could substantially reduce the prognosis and the rate of recurrence as well as its risk factor thereafter.

In line with the search for non-invasive disease diagnostic tools, exhaled breath analysis has brought a great clinical potential not only for disease detection capability but also disease classification as well as therapeutic monitoring of patient's condition, including gastric cancer [1]. The exhaled breath contains certain volatile organic compounds (VOCs) with relatively low molecular weight; which can express the immediate changes in pathological and metabolic process disorders because of being correlated with the existence of a specific disease in the human body as compared with the healthy state. The breath can be analyzed using complex analytical techniques for biomarkers identification [2], but also with cross reactive nanomaterial based chemical sensor arrays that represent a new frontier of non-invasive, rapid and potentially inexpensive diagnostic approach. The chemical sensors are based on monodispersed metallic nanoparticles (MNPs) tailored with different molecular organic ligands that provide sorption sites for the exhaled VOCs, and their interaction changes the chemical and electronic property of the MNPs-ligand nanoassemblies [3-5].

Here we introduce a cross reactive gas sensor array based on AuNPs capped with various organic ligands and demonstrate its suitability for early diagnosis of gastric cancer from exhaled breath samples analysis.

2. Experimental section

The fabrication and deposition of monodispersed metal nanoparticles were achieved using the Advanced Gas Deposition technique [6, 7]. The nanoparticles were deposited between two parallel interdigitated gold electrodes, 15 µm gapped, patterned by rf-sputtering on top of one side polished p-type Si-substrate. The as-deposited nanoparticles were then capped by dip coating the devices in a solution of different thiolated organic ligands such as 4-methoxy-α-toluenethiol (MTT), methyl-3-mercaptopropionate (MMPP), octadecylamine (ODA) and 1-decanethiol (DT), dissolved in ethanol. These organic ligands consist of an aromatic ring and either polar, non-polar or amine functional tails, which maximize the sorption of VOCs from exhaled breath.

Breath samples were collected after written informed consent from a total of n=78 volunteers, where n_s=47 (n_1=18 GC and n_2 =29 healthy control) breath samples were used for breath analysis with the sensor array; and n_{GCMS}=31 breath samples (n_1=16 GC and n_2=15 healthy control) were used for GC-MS analysis. A simple–to-use breath sampler, BioVOC™, was used to collect the alveolar breath part of exhaled breath, which is most likely to contain the metabolites. The collected breath samples were directly injected into the sensor chamber, and the electrical current through the sensors at a constant applied voltage of 5V was recorded. Keysight precision source meter, model B2902A and Keysight data acquisition equipment, model 34972A interfaced with a custom made LabVIEW program were used as source meter and data acquisition systems. Sensor responses were measured as a change in the electrical current upon exposure to the breath samples. Data extracted were further treated and normalized before pattern recognition was applied to build a diagnostic model.

Additionally, a second breath sample provided by the same patient was stored in ORBO™ 420 tubes with

Tenax® TA sorbent material for GC-MS analysis. GC-MS studies were performed in the splitless mode using a GC-MS equipment (Agilent G7200A) coupled with a special Q-TOF detector. Chromatograms analysis was realized employing the Unknown Analysis software operated in the automatic mode with the match factor set to 60, and student t-test with a cut of value α=0.05 was then applied for biomarkers identification.

3. Results and Discussion

3.1 Breath Analysis with Monolayer Capped AuNP Based Sensors Array: **Fig.1** illustrates a representative response of one of the sensors to the exhaled breath of two volunteers.

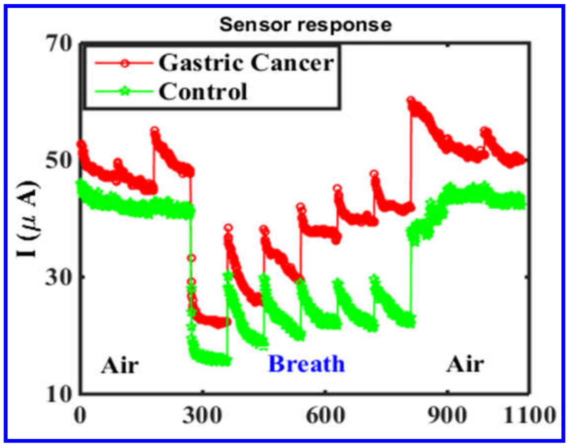

Fig. 1. The response of the [AuNP-ODA] sensor toward exhaled breath samples of a GC patient (red) and control volunteers (green).

The physiochemical sorption of the breath VOCs on the sensing matrix induces the swelling of the AuNPs-ligand matrix and hence increases the distance between neighbouring NPs. The exhaled breath contains a mixture of several thousands of VOCs, and the sensor response observed might be attributed to the collective effect of each VOC interaction with the sensing organic matrix.

For the feature extraction, in one set of measurement with six cycles, one feature per cycle was extracted at the middle of the curve constituting six features per sensor.

The features extracted from each sensor were then used as inputs for different pattern recognition algorithms. **Fig.2** shows the PCA graph obtained with the responses provided by sensor [Sensor 4: AuNPs-ODA] towards the exhaled breath samples of GC patients and patients with non-malignant conditions, indicating a very fair classification between the two groups. Next, two supervised pattern recognition algorithms (probabilistic neural network – PNN, and support vector machines – SVM), were employed for building classification models, and the classification accuracy was predicted employing leave-one-out cross-validation. The maximum classification accuracy obtained was 94.23 % for sensor - 4 with SVM algorithm and leave-one-out cross validation strategy.

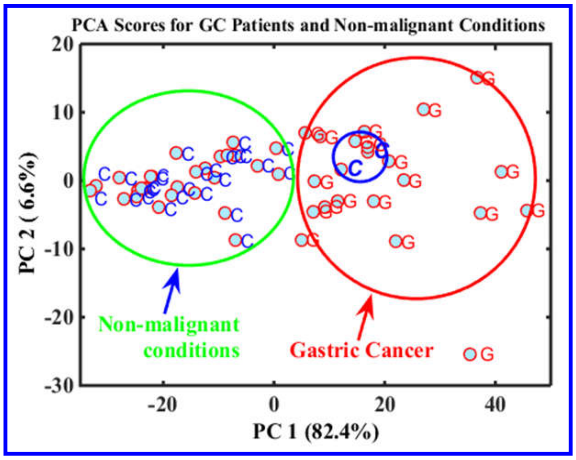

Fig2. PCA classification obtained from the response of the sensor [AuNP-ODA].

3.2. GC-MS Analysis

GC-MS analysis of the breath samples of GC patients and the controls group revealed seven significantly different VOCs between the two study groups: 3-decene, 2,2-dimethyl; octadecane; m-xylene; hexadecane; pyridine;cyclohexane,1,1'-(2-propyl-1,3-propanediyl),bis and eicosane. For all of them p-value was < 0.04. The first five of these VOCs were significantly elevated in the breath samples of the GC patients, whereas the last two VOCs showed a significant increase in the controls group.

4. Conclusions

We have demonstrated that ligand-capped AuNP based gas sensor array could be used as a diagnostic approach for gastric cancer through the analysis of exhaled breath samples. By combing sensors responses with pattern recognition methods provided a powerful classification and discrimination of GC patients from non-malignant gastric conditions. The nanomaterials and ligands used in this study could be tailored to specifically and selectively detect the breath prints of patients with different gastric conditions. The chemical analysis of the breath samples showed that seven VOCs biomarkers were statistically different between GC and other gastric complains.

References

[1] Xu, Z-q, Broza,Y.Y., Ionescu, R., Tisch, U., et al., *Br. J. Cancer*, 2013, 108, pp. 941-950

[2] Amann, A., et al. *Annu. Rev. Anal. Chem*., 2014, 7, pp.455-482

[3] Tisch, U. and Haick, H. *MRS Bulletin*, 2013, 35(10), pp. 797–803

[4] Broza, Y.Y. and Haick, H., *Nanomedicine*, 2013, 8(5), pp.785-806

[5] Barash, O., Peled, N., Hirsch, F.R. and Haick, H., *Small*, 2009, 5(22), pp.2618-2624

[6] Welearegay, T. G, Gualdron, O.E, Jaimes, et al. *Proccedia Engineering*, 2016, 168, pp. 133-136

[7] Granqvist, C.G., Buhrman, R.A., *J. Appl. Phys.1976,* 47, 2200–2219.

CHARACTERIZATION OF GLYCOPROTEIN AND LIPOPROTEIN PROFILES OF RHEUMATOID ARTHRITIS (RA) PATIENS BY ^{1}H-NUCLEAR MAGNETIC RESONANCE SPECTROSCOPY (^{1}H-NMR).

Rocío Fuertes Martín[1], Núria Amigó Grau[1], Joan Carles Vallvé[2], Silvia Paredes[2], Dèlia Taverner[2], Lluis Masana[2]. Xavier Correig Blanchar[3].

[1]Biosfer Teslab,SL; Metabolomics platform, URV; IISPV; CIBERDEM; Reus-Tarragona, Spain.
[2]URLA, Hospital Universitari Sant Joan de Reus; IISPV; CIBERDEM; Reus-Tarragona, Spain.
[3]Metabolomics platform, Universitat Rovira i Virgili, IISPV; CIBERDEM; Reus-Tarragona, Spain.4
rfuertes@biosferteslab.com; rociofrtsm@gmail.com

Aim:

RA is an autoimmune and chronic inflammatory disease associated with a high index of morbidity and mortality by cardiovascular diseases (CVDs). ^{1}H-NMR is a technique capable of determining the lipoprotein and glycoprotein profiles to characterize dyslipidaemias and inflammatory processes. The objective of this study is to characterize the plasmatic glycoprotein and lipoprotein profiles of RA patients using ^{1}H-NMR to identify patterns of the disease's severity.

Methods:

Serum samples of 207 RA patients were analysed by ^{1}H-NMR. Lipoprotein (Liposcale® test) and glycoprotein profiles were characterized. On the other hand, the traditional inflammatory markers such as C-reactive protein (CRP), fibrinogen, glycosylated haemoglobin (HbA1c) and the erythrocyte sedimentation rate (ESR) were determined.

Univariate statistical analysis was conducted to identify associations between the inflammatory markers and the ^{1}H-NMR lipoprotein and glycoprotein profiles. Multivariate statistical methods were used to model the index of disease activity (DAS28) by using inflammatory and NMR-derived parameters as predictor variables.

Results:

There was a modest but significant positive association between HbA1c levels and IDL-cholesterol, IDL-triglycerides and VLDL-triglycerides. Moreover, ESR, CRP and Fibrinogen concentrations were highly associated with glycoprotein profile parameters.

Finally, multivariate analysis showed that the inclusion of glycoproteins along with traditional parameters of inflammation significantly improves the classification of the activity and severity of RA according to DAS28 (area under the ROC cross-validated curve 0.760.

Conclusions:

^{1}H-RMN is a useful tool to identify atherogenic and inflammatory profiles in patients with RA. These profiles, along with the classic inflammatory parameters, provide more accurate information about the severity and activity of the disease.

Surface modification of Nanoporous Alumina towards bio-sensing applications in optical nano-fluidic system

L. Pol, L.K. Acosta, J. Ferré-Borrull, E.
Xifre-Pérez, L.F. Marsal
Departament d’Enginyeria Electrònica, Elèctrica i Automàtica, ETSE, Universitat Rovira i Virgili,

Lluis.marsal@urv.cat

Abstract

A simple and dynamic nanoporous anodic alumina (NAA) biosensing-system is developed in subsequent functionalization steps and provides both aptamer and antibody recognition possibility in an optical nano-fluidic apparatus. In this work we report a new functionalization path for the attachment of aptamers to the NAA and the capability of two optical detection methods to selectively detect target molecules in biosensing probes, effective optical thickness (EOT) and integral average over wavelengths (IAW)

Introduction

The surface functionalization of nanoporous anodic alumina (NAA) is a crucial step to use it like platform for biosensing applications. Antibodies are commonly used in immunosensing applications because of their well-known binding mechanism between a very wide range of antibodies with their antigens. Aptamers, on the other hand, are single-stranded nucleic acid molecules that bind with high affinity and specificity to their target. They are a promising class of compounds for biosensing since their 3D structure can be tailored to bind a wide variety of biomolecules down to the femtomolar range.

In this work, we propose and study a path for the attachment of aptamers and antibodies to NAA based on procedure illustrated in Figure 1and study its validity for biosensing based on the reflectance spectroscopy method in a flow cell.

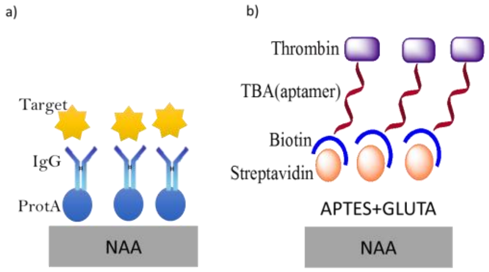

Fig.1: Scheme of surface modification for a) antibody and b) aptamer functionalization

Experimental

For aptamer functionalization in the first step NAA is modified by grafting aminopropyl triethoxysilane (APTES) and glutaraldehyde (GTA). This method has already been demonstrated for protein attachment on NAA[2]. Furthermore, it has also been used for DNA attachment to detect ATP [3]. The second step consists on the covalent attachment of Streptavidin to the APTES-GTA while the final step is the grafting of the biotinylated aptamer to the Streptavidin.

The antibody attachment was performed by protein A capture probe, first the protein A is bound by physical adsorption to the NAA, the antibody binds to protein A in the F_c region and then the antigen (target molecule) binds to the F_{ab} region of antibody [4].

The study of each surface modification to bind Streptavidin is carried out by FTIR spectroscopy (Fig.2) where we observe C-H peak of APTES, amide bounds and one broad peak of Streptavidin whose signal intensity depends on the Streptavidin concentration.

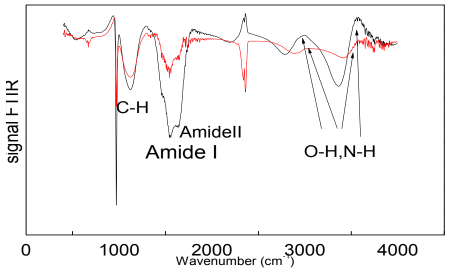

Fig.2: FTIR spectra with APTES+GTA+ Streptavidin 100μg/ml and 10μg/ml

The sensing capabilities of the fucntionalized NAA were tested by in-situ reflectometry in a flow cell. We used two different metrics to evaluate the variations in reflectance spectra: effective optical thickness (EOT) and integral average over wavelengths (IAW).. These methods are based on Fabry Perot interferences between air and porous alumina substrate of white light reflected from the porous alumina which generates a thin film interference spectral pattern (Fig.3) governed by the Fabry Perot relationship.

In the flow cell system, we monitored in-situ reflectance spectra of NAA with successive injections of molecules with washing steps between each one obtaining the corresponding EOT and IAW (Fig.5).

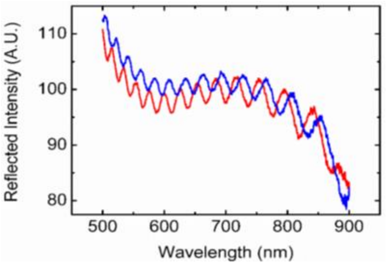

Fig. 3: Reflectance spectra of white light from NAA thin film.

From reflectance spectra, we calculate on one hand EOT (optical thickness) by Fourier Transform (Fig.4a) and on the other IAW (Intensity Average over Wavelengths) by differences between spectra and (Fig. 4b).

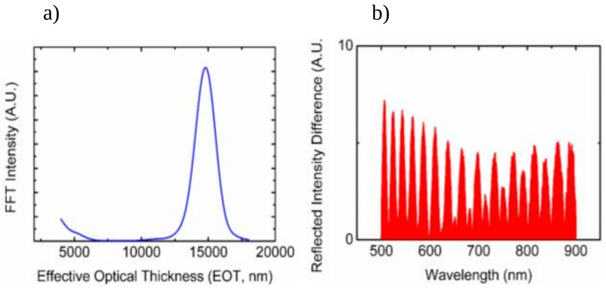

Fig4: Procesed data of white light reflectance spectra a) FFT and b) IAW

Results and discussion

When Streptavidin is injected in pre-functionalized NAA with APTES+GTA (Fig.5a) or Biotin is injected on the Streptavidin-modified NAA (Fig.5b) a signal increase is observed. Such signal variation is maintained after PBS injection. Figure 5c shows the results after the successive injection of protein A and IgG. Both EOT and IAW show a change in signal after each injection.

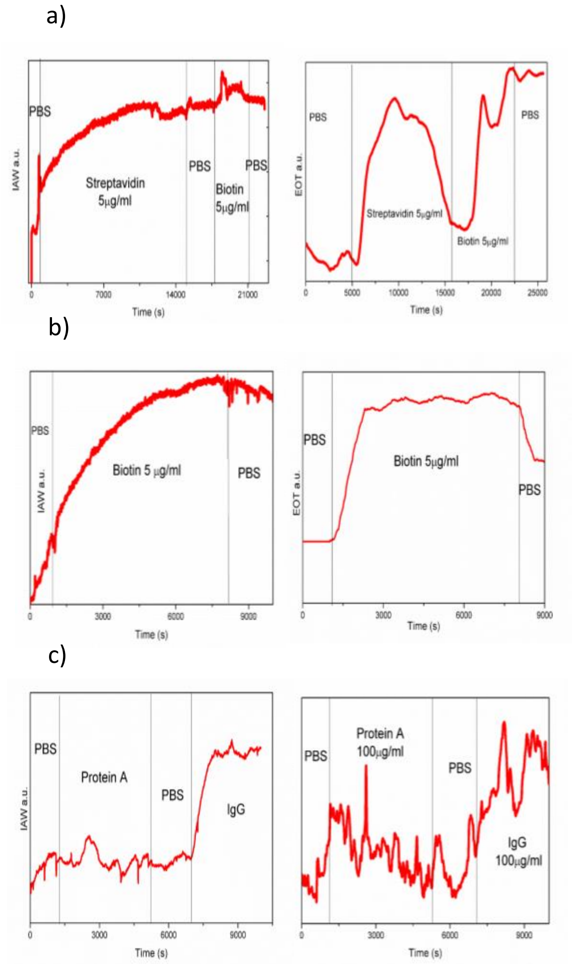

Fig.5: Real-time EOT and IAW with different molecule injections. a) Preincubation with APTES + GTA with injection of Streptavidin at 5µg/ml + injection of Biotin at 5µg/ml, b) Preincubation APTES+GTA + Streptavidin at 5µg/ml with Injection Biotin 5µg/ml, and d) Injections Protein A and IgG both at 100µg/ml.

Conclusions

We demonstrate by FTIR the good attachment of ATPES + GTA + Streptavidin therefore its ability to act as a support for bonding biotinylated compounds; furthermore the results in flow cell confirm that both methods, EOT and IAW are able to monitor the binding events on the pore surface.

References

[1] D. J. Patel, A. K. Suri, F. Jiang, L. Jiang, P. Fan, R. A. Kumar, and S. Nonin, *J. Mol. Biol.*, vol. 272, no. 5, 645–64

[2] M. Baranowska, A. J. Slota, P. J. Eravuchira, G. Macias, E. Xifré-Pérez, J. Pallares, J. Ferré-Borrull, and L. F. Marsal, *C. Sur.B Bio.*, vol. 122, 375–383

[3] Y. Jiang, N. Liu, W. Guo, F. Xia, and L. Jiang, *A. Chem. Soc.*,vol. 134, 15395−15401.

Characterization of human breath profiles by using WO_3 nanowires and commercial SnO_2 gas sensors combined with multivariate analysis

Tarik Saidi[1,2] , Tesfalem Geremariam Welearegay[3], Omar Zaim[1,2], Oriol González León[3],
Radu Ionescu[3], Nezha El Bari[2], Benachir Bouchikhi[1,*]
[1] Sensor Electronic & Instrumentation Group, Moulay Ismaïl University, Faculty of Sciences, Department of Physics, B.P. 11201, Zitoune, Meknes, Morocco
[2] Biotechnology Agroalimentary and Biomedical Analysis Group, Moulay Ismaïl University, Faculty of Sciences, Department of Biology, B.P. 11201, Zitoune, Meknes, Morocco
[3] Department of Electronics, Electrical and Automatic Engineering, Rovira i Virgili University, Tarragona, Spain
*Corresponding author: benachir.bouchikhi@gmail.com

ABSTRACT

The analysis of volatile organic compounds (VOCs) emanating from human breath is an efficient method to appraise information about health status. Electronic nose technology has been emerged as new method to analyze human breath and produce specific VOCs patterns. The goal of this study was to test the feasibility of two sensor arrays to characterize two kinds of breath related to smokers and non-smokers volunteers. The first sensor array contains six interdigitated sensors based on metal-functionalized WO_3 nanowires prepared by aerosol assisted chemical vapor deposition (AACVD); while the second one comprised six MQ sensors based on SnO_2. A total of 96 samples were collected from 32 volunteers containing 11 smokers and 21 non-smokers as well as 15 room air samples. Principal component analysis (PCA) and Support Vector Machines (SVMs) show that WO_3 sensor array gives further accuracy results than SnO_2 sensors. The encouraging results indicate the suitability of the WO_3 based e-nose for breath analysis applications and could be further used in clinical practice for diseases monitoring.

Index Terms— Electronic nose, breath analysis, WO_3 nanowires sensors, SnO2 sensors, Chemometrics, Smoking discrimination.

1. INTRODUCTION

Chemical compounds exist in cigarette smoke, such as benzene, toluene, 2,5- dimethylfuran, and acetonitrile are inhaled through the respiratory system and distributed to various organs as VOCs which were exhaled in breath [1]. Analytical approaches such as Gas Chromatography coupled to Mass Spectrometry (GC-MS) or Proton-Transfer Reaction Mass Spectrometry (PTR-MS) allow detailed quantification of the composition of breath VOCs regarding smoking status [1-3]. Nonetheless, these techniques are usually expensive, bulky and require suitable pre-concentration methods and high skilled operators, which limit their utility in clinical practice and make them unsuitable for personal healthcare. Practical diagnosis approaches which use VOCs as predictive biomarkers to distinguish between individuals according to their health status must be based on an easy-to-use method using point-of-care devices. Therefore, there is an urgent need for developing a new generation of reliable, accurate, robust and cost effective gas sensors with enhanced sensitivity, selectivity and fast response time to facilitate the early detection of certain breath VOCs which are considered as predictive biomarkers of certain diseases. Electronic nose technology could be described as a VOCs pattern recognition system consisting of an array of gas sensors with cross sensitivities that create specific “smell-prints” of different analytes. Several recent studies of breath analysis have investigated diseases as endogenous problems [4]. Few have examined healthy subjects who have inhaled potentially noxious vapors [5]. In the present work, we aimed to compare the feasibility of two sensor arrays based on SnO_2 and functionalized WO_3 devices to discriminate breath VOCs patterns according to the smoking status of studied volunteers taking into account the effect of room air. Datasets gathered from both sensor arrays were considered for analysis by PCA and SVMs. Hence, tobacco smoking detection is an evaluating study for assessing the ability of WO_3 and SnO_2 sensor arrays to characterize breath VOCs pattern.

2. MATERIALS AND METHODS

2.1. Elaboration and structural characterization of pure and functionalized WO_3 sensors

Aerosol assisted chemical vapor deposition (AACVD) method was used to provide a wide range of nanostructured tungsten oxide-based materials which were deposited onto alumina substrates. Tungsten trioxide (WO_3) nanostructures were prepared by using tungsten hexacarbonyl (WC_6O_6) as a precursor, which were synthetized according to the procedure reported in [6]. The reactor temperature was fixed at 500ºC for growing pure WO3 nanostructures and at 380ºC for growing functionalized WO3 with Gold, Platinum, Gold/Platinum, Nickel and Iron nanoparticles. Environmental scanning electron microscopy (ESEM) analysis was used to investigate the morphology of the sensitive surfaces of the different nanostructures grown on alumina substrates.

2.2. Breath samples and experimental set-up

Three breath samples were collected in three Tedlar® bags from each of the 32 volunteers which contain 11 smokers and 21 non-smokers that have never smoked in the past. The unfiltered ambient air in the collection room was also sampled 15 times by pumping room ambient air in Tedlar® bags. The developed e-nose system consists of two set of WO_3 and SnO_2 gas sensors. The first one comprised six elaborated sensors based on WO_3: non-functionalized WO_3, Au/WO_3, Pt/WO_3, Pt/Au/WO_3, Ni/WO_3 and Fe/WO_3 with isolated platinum heaters in their backsides. The second set consisted of MQ-series sensors based on SnO_2: MQ-2, MQ-3, MQ-9, MQ-135, MQ-137 and MQ-138 obtained from Hanwei Electronics Co., Ltd., (Zhengzhou, China). The sensor array responses were acquired using NI USB-6212 from National Instruments. Breath samples were transferred continually by pumping the content of each bag toward sensors chamber at a flow rate of 200 mL/min for 10 min.

2.3. Data preprocessing and multivariate analysis

Data pre-processing is an important step before applying pattern recognition methods. Two sensing features were extracted from the curve of each sensor in order to fully exploit the main information present in the response. One sensing feature is related to $\Delta G/G_0$, while the second sensing feature is related to the area under curve (AUC) during the exposure time. The comparison between these features regarding the discrimination purpose revealed that the first sensing feature of $\Delta G/G_0$ give us more accuracy than the second one. As stated above, two chemometrics were used to analyze data gathered from the e-nose. PCA is a powerful, linear, and unsupervised pattern recognition technique that has been shown to be effective for the classification of electronic nose datasets [7]. SVMs approach was also used, as a supervised learning technique, for identification analysis. This method trains ½C×(C - 1) binary SVM models, where C is the number of individuals. Each ½C×(C - 1) binary SVM classifiers provides a partial decision for classifying every measurement. The prediction accuracy was calculated employing the leave-one-out cross-validation method.

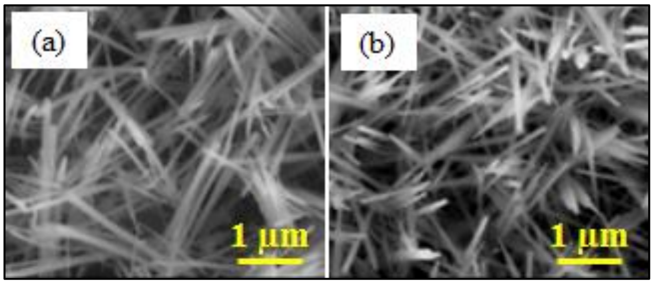

Figure 1. Typical ESEM images for two sensitive areas sensors related to: (a) Au/WO_3; (b) Pt/WO_3.

3. RESULTS AND DISCUSSIONS

3.1. Surface morphology of WO_3 nanostructures

Figure 1.a shows ESEM image of Au/WO_3 deposited on alumina substrate at 380 °C. It can be seen that AACVD method could produce a thicker long layer of non-aligned nanostructures, with high density and homogeneous distribution in the entire substrate. In contrast, the films functionalized with platinum nanoparticles grown at 380 °C showed a mixture of non-aligned uniformly distributed nanowires (NWs) structures (Figure 1.b). The deposited layers were uniform and covered the substrate completely. For instance in gas sensors, the relatively high level of crystallinity has improved stability of sensor response [8].

3.2. Radar plot

Radar plot is typically suitable for illustrating and comparing e-nose responses. Figure 2 displays the breath-prints upon exposure of samples of smoker and non-smoker volunteers, expressed as the conductance change $\Delta G/G_0$ of the normalized data for WO_3 sensor array (Fig. 2.a) and SnO_2 sensors (Fig. 2.b). As it can be seen, a clear pattern variation can be observed for the exhaled VOCs of smoker and non-smoker volunteers.

3.3. Data analysis

Figures 3.a and 3.b show the PCA plot projection of the 96 breath samples and 15 room air with data gathered from six interdigitated sensors based on WO_3 and six MQ sensors based on SnO_2, respectively. It can be seen that the patterns were partially grouped in 3 clusters. Each of these groups corresponds to smokers, non- smoker’s breath and room air samples. PCA results indicate a data variance of 97.63 %

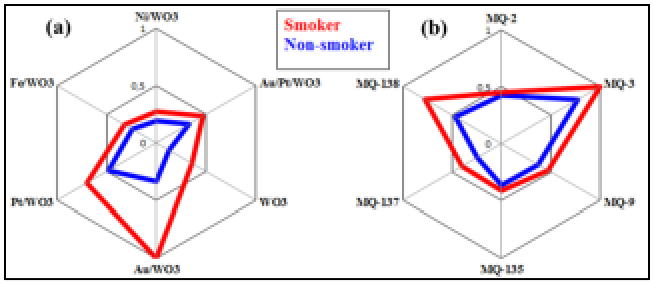

Figure 2. Radar plots of breath VOCs for smoker and non-smoker subjects with data gathered from: (a) six interdigitated sensors based on WO_3, (b) six MQ sensors based on SnO_2.

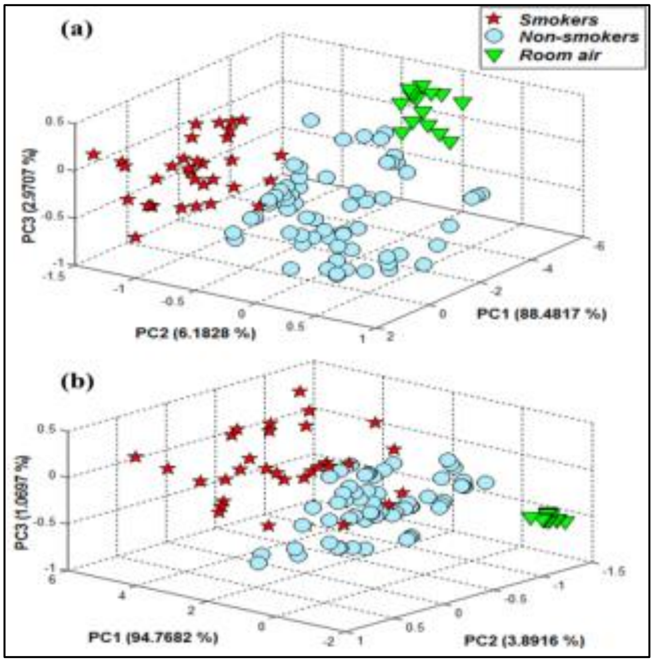

Figure 3. Three-dimensional PCA plot performed on breath samples of 11 smokers against 21 non-smokers and room air with data gathered from: (a) six interdigitated sensors based on WO_3; (b) six MQ sensors based on SnO_2.

and 99.73 % which were explained by the first three principal components for WO_3 and SnO_2 sensors, respectively. That means that SnO_2 sensors are strongly correlated than WO_3 sensors. However, WO_3 sensor array gives further accuracy than SnO_2 sensors in the discrimination among the three clusters related to smokers, non-smokers and room air samples. It should be noticed that breath signatures regardless their smoking habits did not overlap with the cluster of the room air samples, indicating that breath VOCs were not affected by the ambient species. Otherwise, the same databases were treated also by SVMs method. Confusion matrix of SVMs reached a success rate of 99.09 % for WO_3 nanowires sensors and 94.59 % for MQ sensor array in the recognition of smokers from those of non-smoking volunteers. The first success rate was significantly better than the other resulted by Cheng [5], who found 2 misclassified breath-prints from 39 samples. Thus may be due to the effect of exogenous substances in room air.

4. CONCLUSION

This study compare the ability of the WO3 nanowires sensors and commercial MQ-series sensors based on SnO_2 to discriminate the breath VOCs patterns of smoker and non-smoker volunteers. Firstly, AACVD method has been used in a single step process to synthesize pure WO_3 and WO_3 functionalized by gold, platinum, gold/platinum, nickel or iron nanoparticles. Thus, morphology of metal nanoparticles was successfully confirmed by ESEM analysis. Hence, WO_3 as well as SnO_2 based-sensors show different responses between smokers and non-smokers breath. This suggests that the VOCs patterns in exhaled breath differ regarding smoking habits. PCA provides more precision for WO_3 sensor array in distinguishing the three clusters corresponding to exhaled breath of smoker's, non-smokers and room air samples. Besides, SVMs achieved success rates of 99.09 % and 94.59 % for WO_3 and SnO_2 sensor array, respectively. Therefore, the encouraging results of the proposed sensor arrays may be widely extended for other clinical analysis including the early diagnosis of lung diseases.

5. ACKNOWLEDGMENTS

We like to thank Moulay Ismaïl University for financial support of the project "Research support". This work has been funded in part by TROPSENSE under H2020-MSCA-RISE-2014 project, grant agreement number: 645758. R.I. acknowledges a 'Ramón y Cajal' fellowship awarded by the Spanish Ministry for Science and Competiveness (MINECO).

6. REFERENCES

[1] B. Buszewski, A. Ulanowska, T. Ligor, N. Denderz and A. Amann, "Analysis of exhaled breath from smokers, passive smokers and non-smokers by solid-phase microextraction gas chromatography/mass spectrometry," Biomedical Chromatography, vol. 23, pp. 551-556, 2009.

[2] I. Kushch, K. Schwarz, L. Schwentner, B. Baumann, A. Dzien, A. Schmid, et al., "Compounds enhanced in a mass spectrometric profile of smokers' exhaled breath versus non-smokers as determined in a pilot study using PTR-MS," Journal of Breath Research, vol. 2(2), pp. 026002, 2008.

[3] A. Jordan, A. Hansel, R. Holzinger, and W. Lindinger, "Acetonitrile and benzene in the breath of smokers and non-smokers investigated by proton transfer reaction mass spectrometry (PTR-MS)," International Journal of Mass Spectrometry and Ion Processes, vol. 148, pp. L1-L3, 1995.

[4] M.K. Nakhleh, H. Amal, R. Jeries, Y.Y. Broza, M. Aboud, A. Gharra, et al., "Diagnosis and Classification of 17 Diseases from 1404 Subjects via Pattern Analysis of Exhaled Molecules," ACS nano, pp. A-N, 2016.

[5] Z. J. Cheng, G. Warwick, D.H. Yates, and P.S. Thomas, "An electronic nose in the discrimination of breath from smokers and non-smokers: a model for toxin exposure," Journal of breath research, vol. 3, 036003, 2009.

[6] A. Thamri, H. Baccar, F.E. Annanouch, E. Llobet, and A. Abdelghani, "Methanol, Ethanol and Acetone Sensing Using AACVD-grown Tungsten Oxide Nanoneedles," Journal of Nanomedicine & Nanotechnology, vol. 7, pp. 1-6, 2016.

[7] T. Saidi, K. Tahri, N. El Bari, R. Ionescu, and Bouchikhi, B , "Detection of seasonal allergic rhinitis from exhaled breath VOCs using an electronic nose based on an array of chemical sensors," IEEE Sensors, pp. 1566-1569, 2015.

[8] F. E. Annanouch, Z. Haddi, M. Ling, F. Di Maggio, S. Vallejos, T. Vilic, T., et al., "Aerosol-assisted CVD-grown PdO nanoparticle-decorated tungsten oxide nanoneedles extremely sensitive and selective to hydrogen," ACS applied materials & interfaces, vol. 8, pp. 10413-10421, 2016.